UNIVERSITY COLLEGE LONDON

Faculty of Mathematics and Physical Sciences

Department of Physics & Astronomy

NOVEL RF QUASI-OPTICAL COMPONENTS FOR THZ ASTRONOMY

Thesis submitted for the Degree of Doctor of Philosophy of the University of London

by

Paul Moseley

Supervisors:
Giorgio Savini
Elena Saenz

Examiners:
Professor Brian Ellison
Professor Xiaodong Chen

June 19, 2015

To my family

I, Paul Moseley, confirm that the work presented in this thesis is my own. Where information has been derived from other sources, I confirm that this has been indicated in the thesis.

Abstract

There have been many successful THz instruments used in ground and space based telescopes that operate over a range of frequencies from 10s of GHz up to 10s of THz. For some instruments, their operation depends on precise filtering of the received radiation, which can be achieved by using metal mesh filters. These filters can also be referred to as frequency selective surface, which are part of a broad category of metamaterials. By controlling the geometry of these surfaces and combining multiple layers, it is possible to steer the radiation or control the polarisation.

This thesis expands on using existing knowledge and fabrication techniques of metal mesh structures to build new quasi-optical devices, which could be a lightweight replacement for existing components, such as lenses, or new devices with properties that are not possible using traditional materials. Initially an analysis of suitable modelling methods to predict the behaviour of the individual gird structures is performed. It is then shown that multiple girds can be combined to create an artificial dielectric. By using the developed modelling tools a parameter space is found which sets a practical limit on devices that can be built. This theory is also applied to rectangular grids, which have the same properties, but are polarisation dependent.

With this framework in place, a series of devices are designed and characterised. This includes a broadband gradient index flat lens, which was characterised using a VNA from 90 to 220GHz. This design was modified to produce a lens that is capable of separating out two orthogonal linear polarisations and focusing them separated on the same focal plane. Finally an analysis of different of artificial waveplates is performed, to determine which metamaterial structures are best suited for replacing traditional sapphire waveplates.

Acknowledgements

I would like to thank my supervisor Dr. Giorgio Savini for supporting me along this PhD.I am grateful for the knowledge that he has given me which has made this PhD possible. I would also like to thank my second supervisor Elena Saenz for her support as well. I am grateful fro the opportunity to go work at ESTC for 6 months and have access to the facilities there, which was possible due to the ESA NPI scheme. I would also like to thank Cardiff University, especially Peter Ade for agreeing to fabricate the prototypes as well as letting me use the facilities at Cardiff.

I would also like to thank all my family and friends who have supported me along the way. I have been honoured to meet some great new people, who I am sure I will stay in touch with for many years to come.

"Without deviation from the norm, progress is not possible."

- Frank Zappa

Contents

This page was intentionally left blank

List of Figures

This page was intentionally left blank

List of Tables

This page was intentionally left blank

Chapter 1

Introduction

1.1 Observing the sky at THz Frequencies

THz astronomy has now become an umbrella term for a large range of different observations which cover frequencies as low as hundreds of GHz, where the wavelength is measured in millimetres up to tens of THz, which is in the micron wavelength range. There is a range of different phenomenon that occur across this frequency range which are of great interest to the galactic and extragalactic astronomy community. There is still much to explore, which can only be achieved by technological advancements in the instrumentation that detects it. This thesis describes the development of new quasi-optical components implemented using novel materials, that can eventually go towards advancing the next generation of instruments.

In the history of astronomy, the mm-wave to the far infrared spectrum is some of the least explored due to the technological advancements required to detect it. Since the photon energy in this spectrum is too small to be detected using traditional semiconductor technology used for the optical regime. This means that bolometric systems with require cryogenic cooling, or heterodyne systems must be used. It contains a wealth of information, from detecting the earliest light in the universe to searching for complex molecules in the local universe. This is best illustrated by figure 1.1, which shows the electromagnetic energy content of the Universe at various frequencies. At the longest wavelengths the sky is dominated by the cosmic microwave background, which was produced by the primordial

Universe at recombination. Next to that is the cosmic infrared background which is caused by galaxies in the young Universe. Finally there is the cosmic optical background which is dominated by evolved stars/galaxies and active galactic nuclei (AGN)[1]. THz astronomy explores in the first two regions.

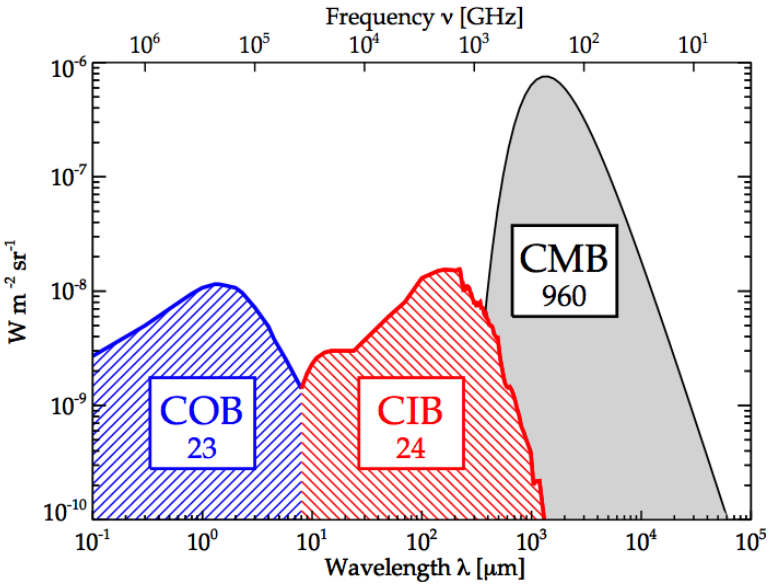

Figure 1.1: Illustration of the spectral energy distributions for the most important backgrounds in the Universe. [1]

There have been an array of both ground and space telescopes that operate over this frequency range. These include, but are not limited to, the Atacama Large Millimetre Array(ALMA) which is a ground based interferometer consisting of 66 ground based telescopes which operate at various bands from in the frequency range of 30 to 950 GHz. It is a fully configurable interferometer, which gives it very high sensitivity and has a spatial resolution down to 10 milliarcseconds. Its is based on a heterodyne receiver, which has the advantage of high spectral resolution. However, to observer at higher frequencies observations must be made above the atmosphere using space telescopes.

Two recent space missions (the Planck probe and the Herschel Space Observatory) have also been launched in the past decade. The goal of Plank over its 3 years of operation was to measure the cosmic microwave background, which shows the state of the Universe when it was only 380,000 years old. By measuring the sky at multiple frequencies from 30 to 857 GHz, it was able to produce the most accurate map of the Cosmic Microwave Backgroun (CMB) yet. The telescope consisted of two different instruments. The Low

Frequency Instrument (LFI) which covered 30-70 GHz and used high-electron-mobility transistors as the detectors. The High Frequency Instrument (HFI) covered 100-857 GHz and used bolometric detectors. Both sets of instruments required liquid cryogenic cooling, which set the finite lifetime of the mission.

The Herschel space observatory operated at a higher frequency range from 440GHZ to 4.4 THz. It consisted of three instruments PACS (Photodetecting Array Camera and Spectrometer), SPIRE (Spectral and Photometric Imaging Receiver) and HIFI (Heterodyne Instrument for the Far Infrared). Each instrument overlapped in bands but had different strengths. SPIRE was a bolometric instrument, which had the greatest sensitivity. HIFI, was based on a heterodyne system, which had the advantage having a high spectral resolution, many orders of magnitude greater then SPIRE.

Due to its spectral and spatial imaging capabilities it carried out a wide range of measurements including the detection of the first nobel gas molecule in space [2]. It was also possible to produce detailed images of the neighbouring galaxy Andromeda 1.2.

Figure 1.2: An infrared image of the Andromeda galaxy taken with the Herschel Space Observatory

1.2 Polarisation in Space

Some of the devices discussed in this thesis deal with the detection and manipulation of polarisation. Described below are two phenomena which give rise to polarisation in space.

1.2.1 Magnetic Fields and Dust

In the local universe it is possible to map the presence of interstellar magnetic fields in space by measuring the polarised light from dusty regions of space. The mechanism for this is given in figure 1.3. Magnetic fields cause ionised dust grains to become aligned along it or to spin with a preferential axis. Due to this, distant visible star light can

become polarised when passing through the aligned grains, and at the same time, due to their alignment, they emit with a preferential orientation resulting in a linearly polarised thermal radiation. By measuring the polarisation component, the magnetic fields in the region can be deducted, thus establishing if the magnetic fields play a role or not in the star formation. [3]

It is also important to measure the polarisation of the interstellar medium since it constitutes a strong foreground for the polarisation measurements of the cosmic microwave background, so it has to be subtracted out.

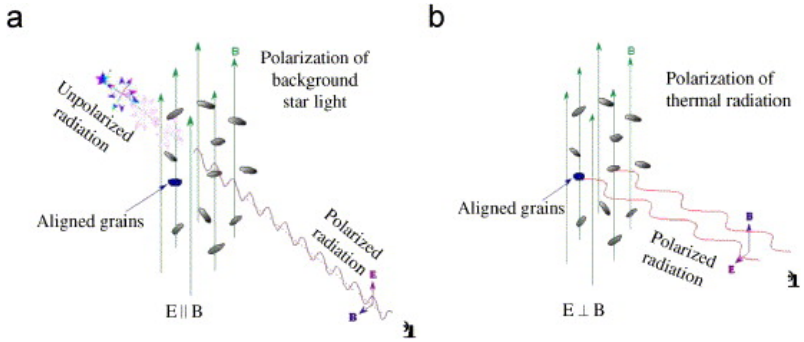

Figure 1.3: a) Polarisation of starlight passing through aligned dust grains. b) Polarisation emitted by an aligned cloud of dust grains [3]

1.2.2 Polarisation of the Cosmic Microwave Background

The intensity of the CMB has been mapped in detail already, but there is also a polarisation component to the signal, which if measured can reveal additional information about the origins of the universe. Polarisation occurs due to scattering of photons off electrons which occurred at the so-called last scattering surface, which is the point in time when the universe had cooled sufficiently for it to become sufficiently neutral to allow the photons to escape. The orientation of the polarisation can be caused by three main effects. The first is caused by the movement of photons from hot to cold regions. Secondly they can be effected by the vorticity in the plasma. Finally a passing gravitational wave will cause a stretching of space at that point.

This final mechanism gives the weakest contribution to the polarised signal, which means it is the hardest to resolve (See 6.1). However, if it can be detected it would be proof for gravitational waves. There have been attempts to measure this signal so far[4], but there has yet to be any definite proof. Therefore, there is still much interest in building

a telescope which is sensitive enough to measure it. Such a telescope would have to have very low noise performance and must have all systematic errors well understood. One such optical component which can aid in accounting for these errors in polarisation is a half wave plate (HWP), which is discussed in chapter 6.

1.3 Applications outside of space

The applications for the technology discussed in this thesis is not only limited to space based applications. There is an increasing interest in earth observation, including measuring the water content in the atmosphere, which has spectral features in the mm-wave region. The next generation MetOps2 satellite has dedicated instrument for measuring the water content in the air and it covers the frequency range 24-229 GHz.

There are also applications in passive imaging which offer a non invasive way to observe the internal structure or spectrum of an object. For example in manufacturing THz imaging can be used to find defects inside an object, while THz spectroscopy can be used to check for any chemical components that might be present in a sample. The same techniques can also be applied to looking a biological samples, such as looking to see if there is a THz signature of cancerous cells[5]. It is possible to have passive imaging of people, which would have useful security applications, such as a replacement to airport scanners.

1.4 THz Detection

The observations stated above have only recently become possible in the last century due to technological developments in detectors, cryogenics and optics. Two of the main types of detector technologies used in space based applications are Bolometers and Heterodyne revivers.

The first bolometer was developed by Samuel Pierpoint Langley in 1878, but it wasn't until the 1950's when they were cryogenically cooled. The latest bolometric detectors require cryogenic cooling down to hundreds of mili-Kelvin, so that the sensitivity of the detector can be maximised.

The modern heterodyne receiver was invented by Edwin Armstrong in 1918. The operation of a heterodyne receiver is different to that of a bolometer. In stead of measuring change in temperature due to the absorbed power, it directly captures in the incident way

and uses a multiplier to down sample the signal. This is achieved by using a mixer which is fed from a local oscillating source of a know frequency. By taking the difference a lower frequency is output, which can be readout using normal electronics. This has the advantage of requiring less cryogenic cooling and it can inherently resolve the spectrum of the signal, which is not directly possible when using a bolometer.

1.4.1 THz Optical Elements

The optical components used in a telescope are independent of the detector technology used. Typical optical elements that are required include lenses, mirrors, filters, beam splitters, polarisers and couplers. Due to the fact that the optical properties of materials change with frequency, different materials that would normally by opaque at visible wavelengths can now be used. Existing mm-wave lenses are made much in the same way as traditional lenses, except they are formed out of polyethylene, which has at THz frequencies the same refractive index as glass at mm-wavelengths.

In cryogenically cooled detectors, placing filters in the optical path allow for frequencies of interest can be selected while other radiation that would warm up excessively the detector system are rejected. To achieve the precise filtering requirements, metal mesh filters are commonly used. [6]. These consist of sub-wavelength periodic metallic structures, which can be tuned to filter the required frequencies. It is this technology that will from the basis of the new devices described here.

1.4.2 Future Science Aims and Their Design Requirements

The demand for next generation space missions are starting to push the limits of traditional materials. Firstly the demand for larger focal plane arrays means the size required of some components exceeds the current manufacturing capabilities. Along with this increase in size comes an increase in weight, so there is demand to produce lighter components while maintaining the same performance. Finally, this metal mesh technology allows a freedom of manipulation of light that is just not possible with traditional optics. This could also allow for the optical path of an instrument to be substantially reduced if it were possible to replace a series of components with one element.

1.5 Thesis Overview

The work in this thesis focuses on the development and production of novel quasi-optical components for THz astronomy using metal mesh structures. The development process can be broken down into modelling the behaviour of the underlying metal mesh structures, designing ideal optical elements and how it can be realised using the metal mesh structures. Then finally the measurement and characterisation of the fabricated device. The work is organised in the 6 chapters below.

Chapter 2 - Frequency Selective Surfaces Theory

In chapter 2 the basics of metamaterial theory is described. The individual building blocks that are used through all the devices described within are introduced. A modelling framework is developed which describes the process of representing these structures using transmission line theory. Finally a comparison between modelling methods and measured data is undertaken to find the best suited method.

Chapter 3 - Equivalent Refractive Index Theory and Applications

The structures introduced in the previous chapters are combined to create an artificial dielectric. Using the modelling tools that have been developed a parameter space is performed to find the range of values that can be obtained using this technique. An alternative approach of modelling these structures is also introduced, which predicts the band structure to determine its dispersion properties.

Chapter 4 - GRIN Lens

This chapter uses the artificial dielectrics to build a gradient index flat lens. The ideal design of the lens is detailed along with the process of realising it with the metamaterial structures. A test bed is then constructed so that suitable measurements can be made on the lens both on and off axis using a network analyser.

Chapter 5 - Polarisation Splitting Lens

A second prototype based on the previous GRIN lens design is detailed. However, this lens is able to separate and focus two orthogonal linear polarisations onto the same focal plane. A prototype of this device is then built and the initial results are presented.

Chapter 6 - Metamaterial Half Waveplates

An overview into the technological developments of half waveplates (HWP) for astronomy purposes, especially for future CMB missions is presented. The feasibility of using metamaterial HWP to replace existing sapphire waveplates is investigated. Existing prototypes are characterised, as well as a discussion of other potential metamaterial designs.

Chapter 7 - Conclusion

Finally, a summery of the conclusions of the work undertaken in this thesis is presented, as well as a suggestion of future devices and techniques which can be pursued in the future.

This page was intentionally left blank

Chapter 2

Mesh Grid Theory

2.1 What is a Metamaterial?

In the simplest case a metamaterial is an artificial material, which consists of a periodic metallic structure, in which the periodicity is much smaller then the incident wavelength, this is typically on the order of $\lambda/10$. The design of the periodic structure controls the overall properties of this bulk material. Which, as with a standard material can be described by an effective permittivity and permeability.

The unit cell can be either 2 dimensional (2d) or 3 dimensional (3d) [7][8][9]. In the case of a 2d unit cell, a 3d metamaterial can be built by stacking these 2d sheets on top of each other with a given spacing. These parameters which define such a build can be chosen to have a range of different material characteristics, such as a positive or negative refractive index. These 2d planar structures are often referred to as frequency selective surfaces, due to the fact that a single surface will also act as a filter. These 2d structures in a multilayer configuration will be the focus of this work, in both the theoretical aspect, given that no single modelling technique has yet delivered a sufficiently reliable performance prediction when multi-elements are considered; and practical focusing on the measurement of the performance of such devices. The building of theese concepts described here will also be described briefly due to the established technological heritage in the build of stacked metal-meshes embedded in polypropylene.

Depending on the selection of unit cell and operational frequency of a frequency se-

lective surface, the material properties can be classified in one of the four regions given in figure 2.1. The bottom left section represents a material that has a negative refractive index. Recent research [10] [11] has focused on searching for suitable structures which operate in this region. An example of such a structure is the split ring resonator, figure 2.2a, this has a narrow operating band where the negative refractive index is achieved[12], this in turn is limiting in its applications for space observations, which require a larger bandwidth.

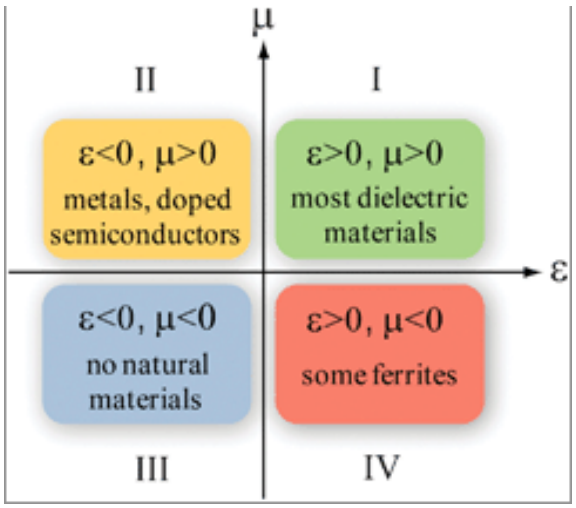

Figure 2.1: Classification of materials based on values of permittivity ϵ and permeability μ.

The positive quadrant represents material parameters which can be achieved with a simple geometry including thin strips and wide patch geometries. All bulk dielectrics also fall into this category. The patch and strip geometries have the advantage of having a broadband operation and are less lossy, figure 2.2 b/c. It is for these reasons that this work will look at using these structures to build devices.

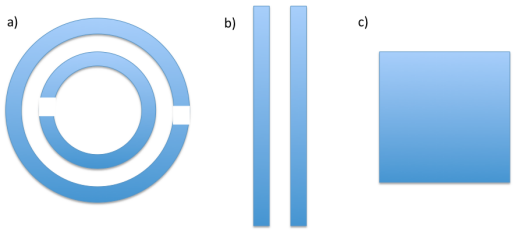

Figure 2.2: Different geometry configurations for 2d metamaterials: a) Splitring Resonators b) Infinite 1d strips c) Square Patch

2.1.1 EM Modelling

Before building a metamaterial, a prediction of its response over a given frequency band, which can be expressed as the transmission, refection or phase must be made. These quantities can then be used to extract the effective material parameters. This prediction is made by modelling how an incident electromagnetic field interacts with the structure of the metamaterial and is then reradiated.

There are many different techniques in which these structures can be modelled which have different levels of complexity. Using maxwells equations to directly solve a problem becomes difficult as the complexity of the structure increases. Therefore, different levels of approximation must be made, which leads to a compromise in computational speed or accuracy. Broadly, most approaches can be divide into two categories, either analytical modelling or numerical modelling. It is generally assumed that numerical modelling produces a more accurate solution, since for a finite element or finite difference time domain approach, the object to be modelled must be suitably discretized using a mesh, in order for Maxwells equations to be solved at each point. Using an analytic approach, a number of assumptions such as the periodicity of structure and thickness of the metal are made. This allows different techniques can be used to solve a given structure. Using this technique gives a much quicker simulation time, but puts constraints on the kind of structures that can be simulated. It will be shown later, in some circumstances, the analytical approach is as accurate as the corresponding numerical technique, while being considerably quicker, which is crucial when a larger number of parameters have to be varied to optimise a given device.

In practice a combination of techniques are required to design a metamaterial based device. In this thesis, the main modelling tool developed is an analytical equivalent circuit model to represent the 2d planar metamaterials. It can then be modelled as a multilayered material by using transmission line theory. This can then be validated using HFSS [13], which is an industry standard finite element modelling tool. The following sections detail how the transmission line formalism is derived.

Computational comparison of HFSS and transmission line model

Simulating structures in HFSS will always take more computational time then using the equivalent analytical model described in this chapter. However, it is an important tool

to use as it is able to validate and check individual results from the analytical model. In the cases where it is possible to run a simulation on HFSS, the initial design would be found using the analytical model. Then this final proposed design would be simulated using HFSS to verify. This final check can be useful as saves possible expenses and time in fabricating and testing a device. While HFSS could theoretically model any device if it had access to unlimited memory and time, in practise it is not practical to model some devices.

A simple free standing grid could be simulated in under an hour using HFSS at low frequencies. However, as the frequency increases the computational time increases, since the number of mesh cells or unknowns increases. This is not the case in the analytical model which can solve a structure in the order of seconds, the computational time does not change with frequency. When cascading grids, the computational time scales linearly for the analytical model and any change between the periodicity of grids does not matter. HFSS will also scale linearly, but only if the cascaded grids have the same periodicity. This is because HFSS must have a single common periodic boundary defined across the whole structure. Therefore, if two grids of different periods are cascaded, then a common multiple for the period must be found. This can end up having to simulate a structure which is tens of times larger then the individual gird size. This means that there are a greater number of unknowns to solve for, thus longer computational time. In the case of a device consisting of 20 girds with different periods, HFSS might take a week to find a solution, where are the analytical model would solve it under a minute.

2.2 Equivalent Circuit Modelling Approach

2.2.1 Transmission lines

The basics of transmission line theory were proposed by Oliver Heaviside in the 1880's. The theory was required to explain why, when electrical signals were sent down cables, which were much longer then the wavelength of the signal propagating along them, there would be a loss of transmitted power. This is due to the fact that a signal can not be transmitted instantaneously so the voltage and current vary along a distance and time. By understanding this, a transmission line could be designed with a given impedance which describes the maximum amount of power that can be transmitted and would minimise the amount of power that is reflected from the load.

When a signal is propagated down a transmission line, consideration of the connecting load is just as important as the line itself. This is due to the fact that at the interface between the transmission line and load, reflections will occur, which is related to the maximum power that can be transmitted. By tuning the properties of the line and load so they match, zero refections will occur. Electronic co-axial cables have a standardised transmission properties which are defined as the impedance of cable, so that connected loads can be designed to have a similar impedance to maximise power transmission. This formalism is much simpler to work with, since only the impedance of a line or device needs to be known and not how the voltage and currents are behaving inside.

A transmission line can be modelled as a lumped element circuit of length dz. For a losses line this is just a L-C circuit. This element has a characteristic impedance $z_0 = \sqrt{(L/C)}$. From this it is possible to calculate how much power will be transmitted through a system and how much is reflected. A more detailed explanation is given in Appendix B.

This electrical representation of impedance as a ratio of voltage and currents propagating along a wire can be also expressed as the ratio of electric and magnetic fields propagating in a bound medium. This representation can be formulated from Maxwells equations. It is assumed the substrate used in the devices is lossless.

2.2.2 Representing dielectrics as transmission lines

A dielectric slab can also be described as a type of transmission line. Therefore, the same theory that is used to describe normal transmission lines such as coaxial cable can be applied. This theory can be used to describe how a wave propagates inside a dielectric and how the wave is transmitted or reflected at an interface based on the material parameters.

This theory can be derived from Maxwells Equations. Assuming a uniform plane wave in a lossless medium propagating along a fixed direction, z. It is possible to define the electric,$\mathbf{E}$ and magnetic,$\mathbf{B}$ fields as transverse fields.

$$\mathbf{E}(z,t) = \hat{\mathbf{x}}E_x(z,t) + \hat{\mathbf{y}}E_y(z,t) \qquad \mathbf{H}(z,t) = \hat{\mathbf{x}}H_x(z,t) + \hat{\mathbf{y}}H_y(z,t) \tag{2.1}$$

These fields must satisfy Faradays and Amperes Laws which can be written as:

$$\frac{\partial \mathbf{E}}{\partial z} = -\frac{1/c}{\eta}\frac{\partial}{\partial t}(\eta \mathbf{H} \times \hat{\mathbf{z}}) \qquad \frac{\partial}{\partial z}\eta \mathbf{H} \times \hat{\mathbf{z}} = \frac{1}{c}\frac{\partial \mathbf{E}}{\partial t} \tag{2.2}$$

Where $\eta = \sqrt{\mu/\epsilon}$ is the defined as the characteristic impedance and c is the speed of light. t is time, ω, is the angular velocity. This can be simplified further by assuming harmonic time dependence, since it is assumed the system is in a steady state.

$$\mathbf{E}(z)e^{j\omega t}, \mathbf{H}(z)e^{j\omega t}, \tag{2.3}$$

This also means that that the time derivatives in equation 2.2 can be replaced by $j\omega$ so that it becomes

$$\frac{\partial \mathbf{E}_{\pm}}{\partial z} = \mp jk\mathbf{E}_{\pm} \tag{2.4}$$

The final solutions to this equation can be explained as a superposition of both forward and backwards components.

$$\mathbf{E}(z) = \mathbf{E}_{0+}e^{-jkz} + \mathbf{E}_{0-}e^{jkz} \tag{2.5}$$

$$\mathbf{H}(z) = \frac{1}{\eta}\hat{\mathbf{z}} \times \mathbf{E}_{0+}e^{-jkz} + \mathbf{E}_{0-}e^{jkz} \tag{2.6}$$

Where $\mathbf{E}_0$ is an arbitrary constant vector such that $\hat{\mathbf{z}} \bullet \mathbf{E}_{0\pm} = 0$

It is also possible to express the fields in terms of its forward and backwards components.

$$E_+(z) = \mathbf{E}_{0+}e^{-jkz} = \frac{1}{2}[E(z) + \eta H(z)] \tag{2.7}$$

$$E_-(z) = \mathbf{E}_{0-}e^{jkz} = \frac{1}{2}[E(z) - \eta H(z)] \tag{2.8}$$

Equations 2.5 and 2.7 can now be expressed in a more convent matrix format.

$$\begin{bmatrix} E \\ H \end{bmatrix} = \begin{bmatrix} 1 & 1 \\ \eta^{-}1 & -\eta^{-}1 \end{bmatrix} \begin{bmatrix} E_{+} \\ E_{-} \end{bmatrix}, \begin{bmatrix} E_{+} \\ E_{-} \end{bmatrix} = \frac{1}{2} \begin{bmatrix} 1 & \eta \\ 1 & -\eta \end{bmatrix} \begin{bmatrix} E \\ H \end{bmatrix} \tag{2.9}$$

Which will act as the building blocks for modelling more complex structures. Two important quantities can be defined, the wave impedance and the reflection coefficient.

$$Z(z) = \frac{E(z)}{H(z)}, \Gamma(z) = \frac{E_{-}(z)}{E_{+}(z)} \tag{2.10}$$

By substituting in equations 2.5 and 2.7, the wave impedance,$Z(z)$ and reflection$\Gamma(z)$ coefficient can be related to each other by

$$Z(z) = \eta \frac{1 + \Gamma(z)}{1 - \Gamma(z)}, \Gamma(z) = \frac{Z(z) - \eta}{Z(z) + \eta} \tag{2.11}$$

Now that the impedance and reflection coefficients have been defined, the fields must now be propagated through a continuous medium. The reason for defining the fields and boundary impedances in different ways is that the quantities $E_{+}(z), E_{-}(z), \Gamma(z)$ have simple propagation properties, whereas $E(z), H(z), Z(z)$ match simply across interfaces. To derive the propagation matrix consider the field quantities at two given points z_1, z_2 such that the distance between them is given by $l = z_2 - z_1$.

Using equation 2.7 the forward and backwards traveling fields at these two positions can be expressed as:

$$E_{2+} = \mathbf{E}_{0+} e^{-jkz_2}, E_{1+} = \mathbf{E}_{0+} e^{-jkz_1} = \mathbf{E}_{0+} e^{-jk(z_2 - l)} = e^{jkl} E_{2+} \tag{2.12}$$

$$E_{2-} = \mathbf{E}_{0-} e^{jkz_2}, E_{1-} = \mathbf{E}_{0-} e^{jkz_1} = \mathbf{E}_{0-} e^{jk(z_2 - l)} = e^{-jkl} E_{2-} \tag{2.13}$$

These can be expressed in the matrix form

$$\begin{bmatrix} E_{1+} \\ E_{1-} \end{bmatrix} = \begin{bmatrix} e^{jkl} & 0 \\ 0 & e^{-jkl} \end{bmatrix} \begin{bmatrix} E_{2+} \\ E_{2-} \end{bmatrix} \tag{2.14}$$

This is the propagation matrix which describes the behaviour for both forward and backwards propagating waves. From this the reflection coefficient can also be propagated in the same way.

$$\Gamma_1 = \frac{E_{1-}}{E_{1+}} = \frac{E_{2-}e^{-jkl}}{E_{2+}e^{jkl}} = \Gamma_2 e^{-2jkl} \tag{2.15}$$

Using the matrix relations given in equations 2.9 ,2.14 it is possible to derive a propagation matrix for the total electric and magnetic fields.

$$\begin{bmatrix} E_1 \\ H_1 \end{bmatrix} = \begin{bmatrix} coskl & j\eta sinkl \\ j\eta^{-1}sinkl & coskl \end{bmatrix} \begin{bmatrix} E_2 \\ H_2 \end{bmatrix} \tag{2.16}$$

This can also be used to propagate the impedance

$$Z_1 = \eta \frac{Z_2 coskl + j\eta sinkl}{\eta coskl + jZ_2 sinkl} \tag{2.17}$$

The above equations describe how the fields propagated along a continuous medium. However, it must now be considered what happens at the interface between two different mediums, thus two different characteristic impedances η, η'.

Since the impending fields are tangential to the interface, the boundary conditions from the solution of Maxwells equations, show that the total electric and magnetic fields must be continuous across the interface.

$$E = E^{'} \tag{2.18}$$

$$H = H^{'} \tag{2.19}$$

However, substituting for the forward and backward electric fields, the relation is given as

$$E_+ + E_- = E_+^{'} + E_-^{'} \tag{2.20}$$

$$\frac{1}{\eta} E_+ + E_- = \frac{1}{\eta'} \frac{1}{E_+^{'} + E_-^{'}} \tag{2.21}$$

The portion of the forwards and backwards wave which propagate across the interface are related by Fresnels coefficients which are represented by ρ, reflection and τ, transmission. This can be visualised by figure 2.3. Note that depending on the direction of propagation there is a difference in coefficients.

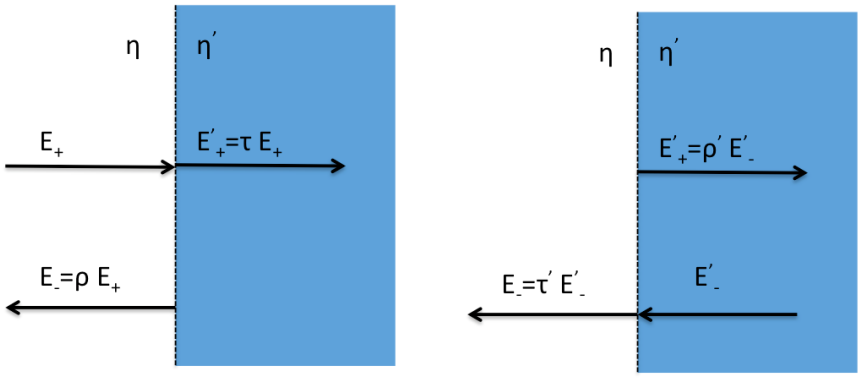

Figure 2.3: On the left shows how fractions of positive traveling wave can be described by ρ, τ and on the right show how a negative travelling wave can be described by ρ', τ'

These relations can be expressed in similar form as the propagation matrix, which relates how the field propagates at the boundary.

$$\begin{bmatrix} E_+ \\ E_- \end{bmatrix} = \frac{1}{\tau} \begin{bmatrix} 1 & \tau \\ \tau & 1 \end{bmatrix} \begin{bmatrix} E_+^{\backslash} \\ E_-^{\backslash} \end{bmatrix} \tag{2.22}$$

The coefficients can be directly related to the characteristic impedance, which since $\eta = \eta_0/n$ can also relate to the refractive index of each material.

$$\rho = \frac{n - n'}{n + n'} \qquad \tau = \frac{2n}{n + n'} \tag{2.23}$$

$$\rho' = \frac{n' - n}{n' + n} \qquad \tau' = \frac{2n'}{n' + n} \tag{2.24}$$

$$\begin{bmatrix} E_+ \\ E_- \end{bmatrix} = \frac{1}{2n_1} \begin{bmatrix} (n_1 + n_2) & (n_1 - n_2) \\ (n_1 - n_2) & (n_1 + n_2) \end{bmatrix} \begin{bmatrix} E'_+ \\ E'_- \end{bmatrix} \tag{2.25}$$

With matrixes 2.14 and 2.25 it is now possible to model any series or combination of dielectrics. One particular application is the modelling of anti-reflection coatings. The overall transmission and reflection properties of the slab can be extracted from the ratio of forward and backward propagating waves.

$$\Gamma = \frac{E_{1-}}{E_{1+}} \tag{2.26}$$

$$\tau = \frac{E'_2}{E_{1+}} \tag{2.27}$$

To demonstrate this theory so far a simple anti-reflection coating (ARC) on a glass slab can be modelled. The required refractive index of the coating is given by $n_{ARC} = \sqrt{n_{slab}}$. Given that glass has an index of $n = 1.5$, the coating must be $n = 1.22$. The thickness is defined by $\lambda/n4$, where λ is the wavelength for which refections will be minimised and n is the index of the coating. Figure 4.21 shows how the coating works. The incident wave strikes the first surface and is partially reflected and transmitted. The transmitted wave strikes the backside of the coating and again is partially transmitted and reflected. However, the coating has been set so that the second reflected wave has undergone a π phase shift which will destructively interfere with the first reflected wave.

There are many more multiple refections that occurs then those shown in 4.21 which are taken into account in the transmission line formalism. Figure 2.5 shows the comparison of the transmission through a coated and uncoated slab modelled using this transmission line approach. The coating thickness was set to $625um$ which give the peak transmission at 4 wave numbers, cm^{-1}. It shows the transmission has increased around that wavelength

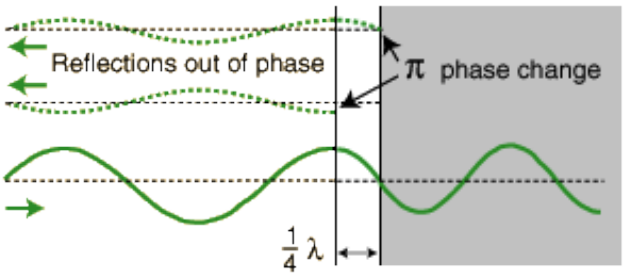

Figure 2.4: Illustration of reflections that occur in an antireflection coating. The coating causes a π phase shift between the two reflections, causing the reflection to cancel out. (Figure taken from [14])

with the addition of only one coating. This use of the transmission line method that additional layers can be added by cascading more matrixes.

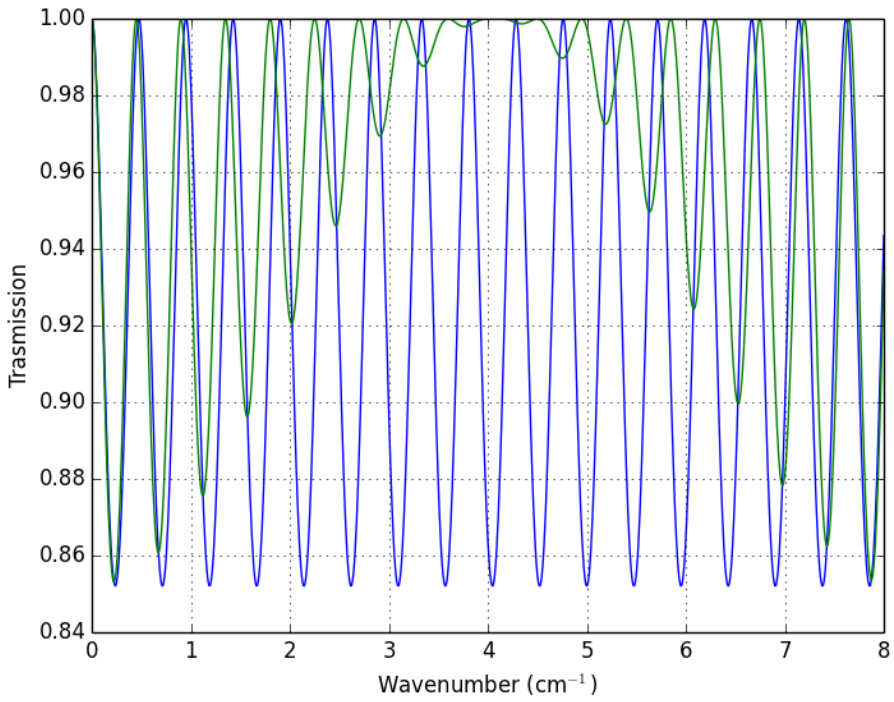

Figure 2.5: When a ARC coating is applied to a slab of quart, it can greatly approve the transmisson at a given wavelength which depends on the thickness of the coating.

2.2.3 Including waveguide discontinuities

After defining how a wave can propagate through any number of dielectric layers, the next step is to consider a metamaterial structure placed at the interface between two dielectric

layers. It will be shown that the behaviour of these metal mesh structures have a response which models that of typical LCR circuits. Since the exact contribution of inductive, capacitive and resistive component depends on the structure used, it is better to represent the grid as a lumped impedance (figure 2.6).

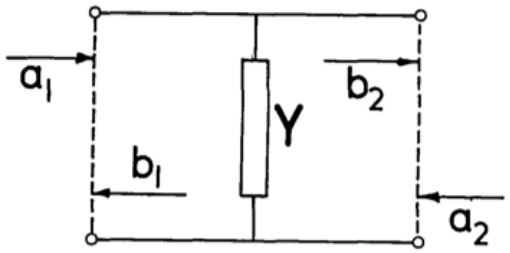

Figure 2.6: Shunted transmission line, with corresponding incident/reflected wave amplitudes. a_1,a_2 define the input amplitude into the element.b_1,b_2 define the output amplitude.

This can be represented as a new scattering matrix, equation 2.28. Note that when there is no grid present the admittance is zero and it reduces to the previous scattering matrix given by equation 2.25. Also this method only models a single linear polarisation, which means that the orientation of the structure must be defined in the admittance approximation. The admittance is defined as the inverse of the impedance $1/Z$. It is used to simplify the ability to cascade multiple elements, which will be required later.

$$r(Y) = \frac{1}{2n_1} \begin{vmatrix} -Y + (n_1 + n_2) & -Y + (n_1 - n_2) \\ Y + (n_1 - n_2) & Y + (n_1 + n_2) \end{vmatrix} \tag{2.28}$$

With the introduction of this shunted impedance matrix, it is now possible to represent a series of cascaded dielectric and metamaterial structures. This is based on the assumption that a suitable representation for the admittance Y can be found the accurately models the response of the grid structure. A series of different approximations are detailed below.

2.3 Equivalent circuit representation

The formulation of the equivalent admittance for a given structure must be found by solving the problem of how the incident field generates currents in the metallic structure, and then how these currents re-radiate a scattered field. Once a solution is found, it can then be used in the shunted impedance matrix. There are two types of geometry this problem will be solved for "patch", 2d, and "strip",1d, structures. The reason for this, is that they have some very useful properties as well as being simple to represent as an equivalent circuit.

Before describing these geometries further, there are some assumptions and relationships that must be taken into account. It is assumed that the metallic structures are infinitesimally thin, hence they are represented as a two dimensional shape, this means that the electrons only move in the plane perpendicular to the incident field.

There is also a useful relationship between complimentary grids called Babinet's principle [15]. This states that the transmission through one mesh screen plus the transmission through the negative of the same mesh rotated through 90 degrees must equal one. This means that while they are physically different mesh structures, only one structure needs to be solved for, since the complimentary structure has the inverse transmission response, assuming that the structure is symmetric.

The simplest structure to understand the response of is a capacitive and inductive gird as shown in figure 2.7, which is also a clear example of Babinet's principle. This structure consists of periodic infinitely long strips, which have a regular periodicity and strip width. These grids act as a capacitive (low pass) or inductive (high pass) filter depending on their orientation with respect to the incident field. A qualitative physical explanation of why the grids exhibit this behaviour by considering the general movement of the electrons at different frequencies[16]. When the field is aligned perpendicular to the strips, figure 2.7b, the grid acts as a low pass filter. Considering a low frequency wave incident on the strip, the electrons quickly gather on the edge of the strip meaning they are stationary on the edge of the strip. This means that the low frequency radiation is not transferred to the electrons movement, so the radiation passes through. Only when the frequency becomes high enough, does the electron become able to move causing absorption. The opposite effect happens when the incident field is parallel with the the grid, figure 2.7a. At low frequencies the electrons are free to travel larges distances the wave perturbs it, causing

them to absorb all incident radiation. As the frequency of the wave increases, the electrons have less distance to oscillate, causing the amount of radiation they absorb to decrease. This therefore acts as a high pass filter, which has the same behaviour as an inductor in a circuit.

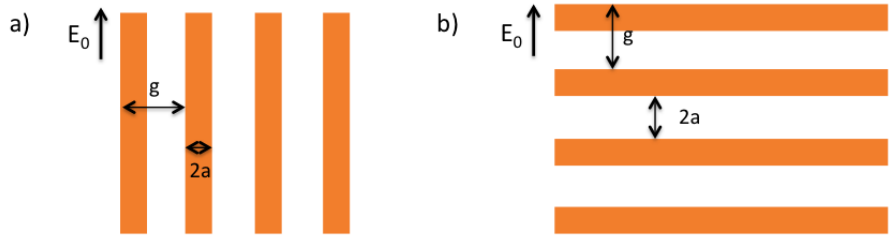

Figure 2.7: The infinite strip geometry can behave as an inductive (a) or a capacitive(b) filter depending on how it is aligned to the electric field.

This grating structure has the limitation that its response is dependent on the polarisation state of the incident wave. This can be overcome by using a square patch and net structure, figure 2.8, which is symmetric. The same qualitative analysis can be applied to these structures. The square patch structure, figure 2.8b, acts as a low pass or capacitive filter, since the the electrons are bound to the edges of the patch at low frequencies. Where as the square net structure, figure 2.8a, will act as a high pass or inductive filter due to the fact that the electrons are free to flow along both axis at lower frequencies.

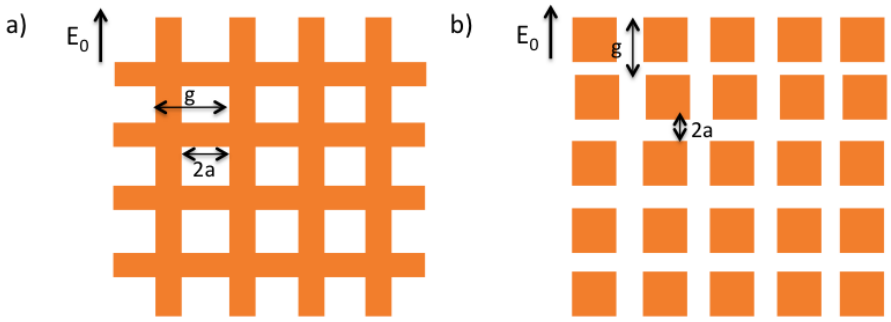

Figure 2.8: a) The net structure acts as a inductive filter. b) The square patches act as a capacitive filter.

The above definitions give an approximate reasoning on why these structures have their given behaviour. However, a more rigours mathematical frame work must be established, so that a solution can be found that explains how the admittance changes with the physical

geometry and frequency.

To formulate a solution, one must assume that the given mesh is infinitely periodic and is incident with a uniform plane wave. Under this assumption Floquet's theorem can be applied 2.30. On the case of a 1d periodic structure, it will have the general solution of the form

$$\mathbf{E}(x,y,z+nd) = e^{(-jnkd)}\mathbf{E}(x,y,x), \mathbf{H}(x,y,z+nd) = e^{(-jnkd)}\mathbf{H}(x,y,x) \tag{2.29}$$

where $n = 0, \pm 1, \pm 2, ...$, d is the periodicity of the strucutre, k is the wavenumber and q is a complex constant. That is the fields in an adjacent period change only by a constant complex multiplier. This can be used to give a generalised solution 2.30 which gives the field at an arbitrary position above a periodic surface. Each term in the series is a Floquet mode.

$$\mathbf{E}(x,y,z) = \sum_{n=-\infty}^{\infty} \mathbf{E}(x,y,z)e^{(-j(q+\frac{2\pi n}{d})z} \tag{2.30}$$

This condition is satisfied by the periodic patch structure 2.31, where d is the periodicity of the structure and I_n is the current flowing in the nth wire.

$$I_n = I_0 e^{-jnqd} \tag{2.31}$$

The actual formulation of the solution is more complex [16] since an accurate model of how the currents are distributed on a patch must be found. The advantages of such a solution is that the currents need to be only derived for one structure. Also, for most problems only the first or second Floquet modes are needed, hence an analytical approximation can be used.

The following sections give an overview of some of most common derivations for capacitive and inductive grids. The notation has been changed so that the geometry of girds that is given is consistent with that given in figures 2.7,2.8.

Marcuvitz

In 1951, N. Marcuvitz published a comprehensive method for solving various waveguide discontinuities using transmission line theory to represent them as an equivalent circuit[17]. One of the problems posed is that of the capacitive strips. These strips are described as an infinitely extended plane grating formed by metallic strips of zero thickness. This assumes that the E field of the incident wave is perpendicular to the strips. The geometry of this structure is defined by just two parameters, a - the gap between strips and g - the periodicity of them, represented by figure 2.7. This approximate solution solution is given in equation 2.32

$$\frac{B}{Y_0} \approx \frac{4g\ cos\theta}{\lambda}\left\{ln\frac{2g}{\pi a} + \frac{1}{2}(3 - 2cos^2\theta)\left(\frac{g}{\lambda}\right)^2\right\},\ \ \frac{a}{g} << 1 \tag{2.32}$$

The validity of this equivalent circuit model is $g/\lambda < 1$ which implies that the structure must have a sub-wavelength periodicity. This is related to the fact that this model can not propagate higher order diffraction modes.

Ulrich

The first paper to produce and model a metal mesh filter was by Ulrich [18]. In this paper he proposes the first equivalent circuit for the 2d mesh structures, shown in figure 2.8. The assumption that he makes are that the grids are taken to be infinitesimally thin, the metal is a perfect conductor and that the capacitive effect of the supporting dielectric is neglected. Equation 2.33 shows how the admittance is formulated. Ulrich takes the equation from Marcuvitz and claims that it is valid in case of a 2-D mesh, except that there is a resonant frequency ω_0. This value defines the frequency at which the grids are either fully transmissive or reflective, depending if it is a capacitive or inductive grid. This value is defined empirically in equation 2.33.

$$\Omega = \frac{\omega}{\omega_0} - \frac{\omega_0}{\omega}, \qquad \omega_0 = 1 - 0.27\left(\frac{a}{g}\right) \tag{2.33}$$

$$Z_0\left(\frac{a}{g}\right) = \frac{1}{2ln\left(\frac{1}{sin(\frac{a\pi}{g})}\right)} \tag{2.34}$$

$$Y(\omega) = \frac{1}{R + jZ_0\Omega} \quad \text{–Capacitive} \tag{2.35}$$

$$Y(\omega) = \frac{1}{R + \frac{jZ_0}{\Omega}} \quad \text{–Inductive} \tag{2.36}$$

Timusk

R. Timusk improved the model to include the presence of the dielectric that supports the capacitive mesh [19]. It is shown that the admittance is increased when surrounded by a dielectric. This correction is accounted for by including the factor $(n_1^2 + n_2^2)/2$. This corrected expression is given in equation 2.37

$$Y_0 = \frac{1}{Z_0} = 2(n_1^2 + n_2^2) ln\left(\frac{1}{sin(\frac{a\pi}{g})}\right) \tag{2.37}$$

LZ

A paper published by Lee and Zarrillo (LZ)[20], gave another formula to give the admittance of a metal mesh, shown in equation 2.38. The form of this equation is similar to that given by Ulrich, except it has been multiplied by an extra term. The chosen value for the resonant mesh frequency is also different. The comparisons they do with numerical solutions match better then Ulrich. However, they have not taken into the account the effect of the dielectric.

$$Y_{ind} = Y_{cap}^{-1} \approx -j\Omega \frac{\left\{\frac{g}{g-2a} + \frac{1}{2}(\frac{a}{\lambda})^2\right\}}{ln\left(\frac{1}{sin(\frac{a\pi}{g})}\right)} \tag{2.38}$$

Compton

Whitborn and Compton produced two papers[21] [15] which expanded on the previous work by Ulrich and Timusk. The paper was written to validate the claims that Timusk had made about the change in admittance due to the effect that the supporting dielectric has on the capacitive grid. The valid the claims of Timusk by using Babinet's principle by measuring the transmission through the two complimentary structures and found a difference equal to the amount Timusk proposed.

The second paper looks at the effect the dielectric has on the resonance frequency of the mesh. They modify Ulrich's equations to produce equations 2.39, 2.40. Note that $\omega = g/\lambda$ is the normalised frequency. In the same paper they also claim that the limits for the transmission line model is in the region where $(\lambda/ng) \geq 2$.

$$\frac{X_L}{Z_0} = -\left(\omega_0' \, ln \, cosec\left(\frac{\pi a}{g}\right)\right)\left(\frac{\omega}{\omega_0'} - \frac{\omega_0'}{\omega}\right)^{-1} \tag{2.39}$$

$$\frac{X_C}{Z_0} = \frac{2}{n_1^2 + n_2^2}\left(4\omega_0' \, ln \, cosec\left(\frac{\pi a}{g}\right)\right)^{-1}\left(\frac{\omega}{\omega_0'} - \frac{\omega_0'}{\omega}\right) \tag{2.40}$$

$$\omega_0' = \omega_0\sqrt{\frac{2}{n_1^2 + n_2^2}} \tag{2.41}$$

2.4 Model comparisons

To validate and compare the above admittance formulas a python code was developed. This was based on the transmission line matrix method detailed above. It developed to be fully modular, so that different admittance models could be used interchangeably. The code also allows for any combination of different dielectric layers, grids and spacings. The basic analytical calculus contained in the code,will also act as a foundation for modelling devices in later sections. A copy of this code can be found in Appendix A. A comparison of these models against a single capacitive grid is shown in figure 2.9. Which shows the Timusk matches the performance of the grid the best.

2.4.1 Substare loss

In all of these models, it is assumed that the absorption losses in the polypropylene substrate are negligible at the frequencies of interest. This is verified by Figure 2.10 which shows that the absorption losses are on the order of a few hundredths of a percent. Therefore is is assumed that the substrate is lossless.

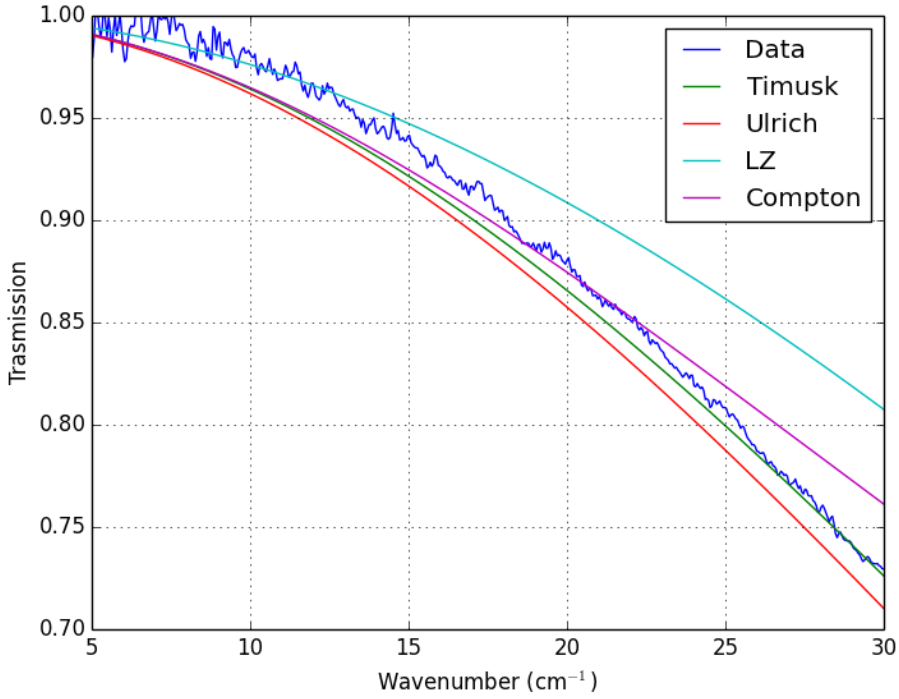

Figure 2.9: Comparison of different equivalent circuit models to measured gird data. Timusk was found to give the most accurate solution.

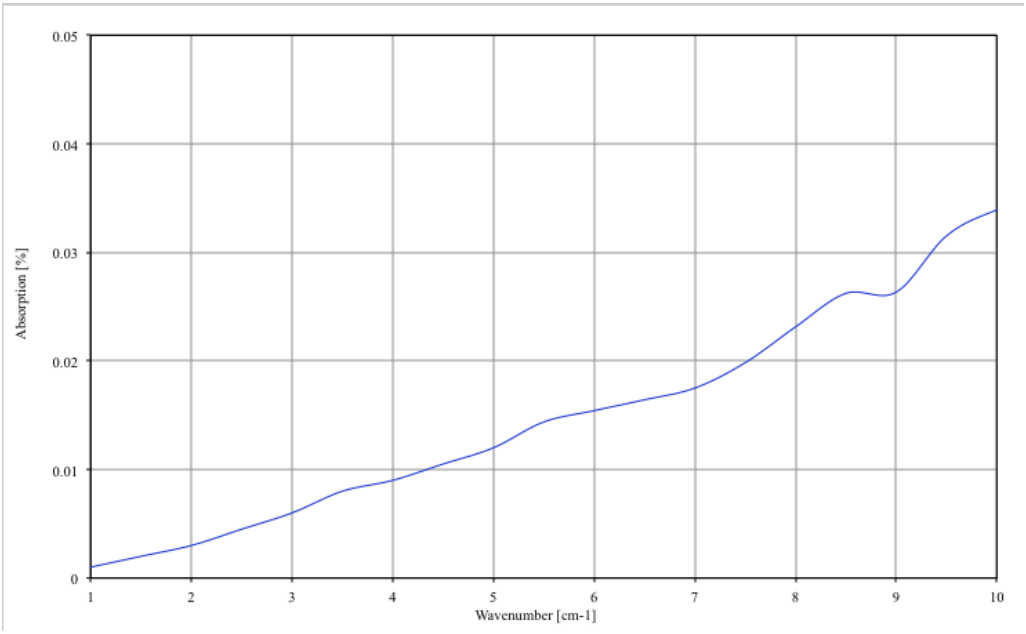

Figure 2.10: The absorption losses as a percent of absorbed power in polypropylene.

2.5 Non-Symmetric Grids

The above examples are all limited to the case of X-Y symmetry, or square capacititve girds. This can be an advantage for some devices, such as filters, since it does not affect the polarisation state of the propagating wave. However, by breaking the symmetry of these structures an anisotropic response can be formed. The extreme case of this has already been given in the case of strip gratings, but intermediate cases are also possible with interesting consequences.

Breaking the X-Y symmetry by considering rectangular patches allows for four variables to change the response of the grid(figure 2.11). The first consequence of the overall structure is that the unit cell periodicity can be different along each axis.

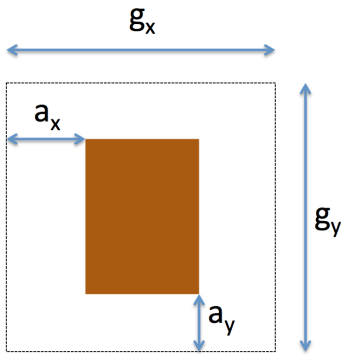

Figure 2.11: Unit cell of rectangular patch. There are now four possible variables to change its response.

The original scattering matrix has to be modified so that propagation can be calculated along both axes. This is based on a simplified case of the method outlined by Berreman [22] providing the scattering matrix in equation 2.42. In this case it is reduced 4x4 matrix consisting of the original 2x2 scattering matrix, one for each polarisation. This is because there is no polarisation leakage between the two axes of the rectangular grids proposed here.

$$S_{n_1 n_2} = \frac{1}{2n_1} \begin{pmatrix} -Y_{TE} + (n_1 + n_2) & -Y_{TE} + (n_1 - n_2) & 0 & 0 \\ Y_{TE} + (n_1 - n_2) & Y_{TE} + (n_1 + n_2) & 0 & 0 \\ 0 & 0 & -Y_{TM} + (n_1 + n_2) & -Y_{TM} + (n_1 - n_2) \\ 0 & 0 & Y_{TM} + (n_1 - n_2) & -Y_{TM} + (n_1 + n_2) \end{pmatrix} \tag{2.42}$$

Due to the broken symmetry in the grids, a new expression for the admittance of rectangular girds must be found. There has been much less focus on a generalised solution to this problem, but some specialised solutions exist in the case where the rectangle becomes a dipole.

Zarrilo

Zarrilo the only known paper which gives an approximation for a rectangular capacitive mesh [23]. His expression is given by equation 2.43. In this expression, the size of the outer unit cell is defined by the geometry a, b and the inner patch size is given by c, d. This paper uses the first mode approximation. This is defined for low frequency regions, which is defined for regions where $a < \lambda$, which is the case for the structures modelled here.

$$Y_L = (-j)2\left\{\sqrt{\frac{\lambda}{a}^2 - 1}\left[\frac{cos(\frac{\pi c}{a})}{1-(\frac{2c}{a})^2}\right]^2 - \frac{1}{\sqrt{\frac{\lambda}{b}^2 - 1}}\left[\frac{sin(\frac{\pi d}{b})}{(\frac{\pi d}{b})^2}\right]^2\right.$$
$$\left.+2\left(\frac{b}{a+b}\right)\left[\sqrt{\left(\frac{a^2+b^2}{a^2b^2}\right)\lambda^2 - 1} - \frac{1}{\sqrt{\left(\frac{a^2+b^2}{a^2b^2}\right)\lambda^2 - 1}}\frac{a}{b}\right]\left[\frac{sin(\frac{\pi d}{b})}{(\frac{\pi d}{b})^2}\right]^2\left[\frac{cos(\frac{\pi c}{a})}{1-(\frac{2c}{a})^2}\right]^2\right\} \tag{2.43}$$

Ikonen

This approximation applies in the extreme case when the rectangles are stretched such that they become dipoles [24] [25]. This method can be used in the case where a large capacitance is required for polarisation while having a much weaker polarisation for the other.

$$Z = -\left(\beta(0) - \alpha^{-1} + \frac{\eta}{2s}\right)d \tag{2.44}$$

$$\beta(0) = -\frac{\eta k}{2d}\left[\frac{1}{kd} - \frac{1}{2} + \frac{j}{\pi}\left(log\frac{kd}{4\pi} + \gamma\right) + \frac{j}{d}\sum_{n\neq 0}\left(\frac{1}{\sqrt{\left(\frac{2\pi n}{d}\right)^2 - k^2}} - \frac{d}{2\pi n}\right)\right] \tag{2.45}$$

2.5.1 Grid Verification

To test the validity of these methods, a series of test grids were fabricated. The Designs of the the grids are given by figure 2.12. The four girds shown here were designed to test the transition from a narrow rectangle to a near square like structure.

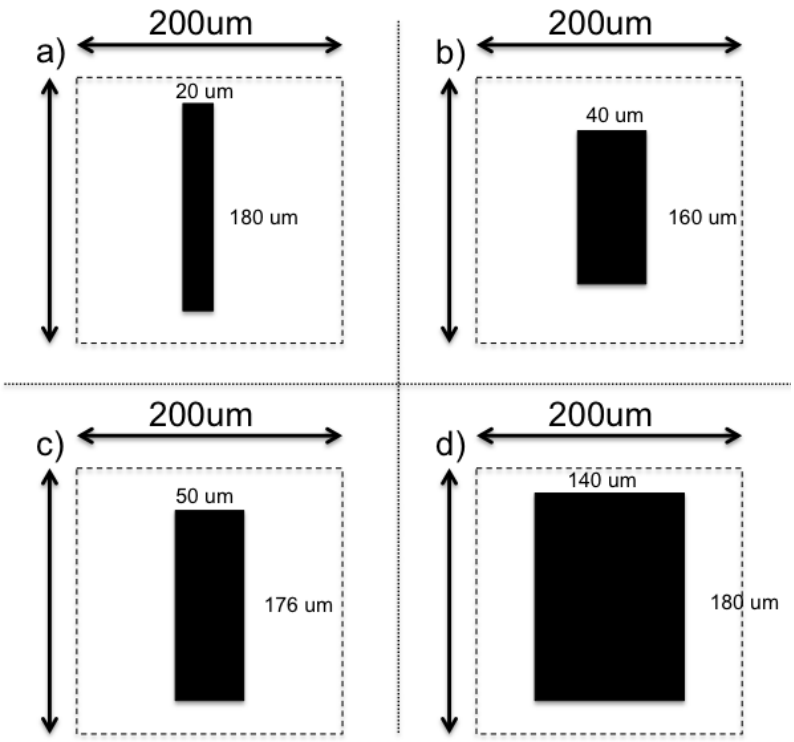

Figure 2.12: The geometry of 4 different rectangular patches to test.

The these grids were measured using a Fourier transform spectrometer (FTS) at Cardiff University. This allows for precise transmission data to be obtained over a larger frequency range with good spectral resolution. At the time a vector network analyser (VNA) was not available to use. The results given by figure 2.14, show that there is a different response depending on the polarisation incident on the structure. The transmission line models were compared to the results of the structure given by figure 2.12a, which shows that there is an agreement between the model and the data. It can be shown that at the grid resonance, where there is no transmission, there is good agreement between all models. Neither model has a good prediction after the resonance of the structure, this is accounted for by the fact there is only modelling the first mode. However, it shows that the model can give an approximation on how the rectangular grid will behave.

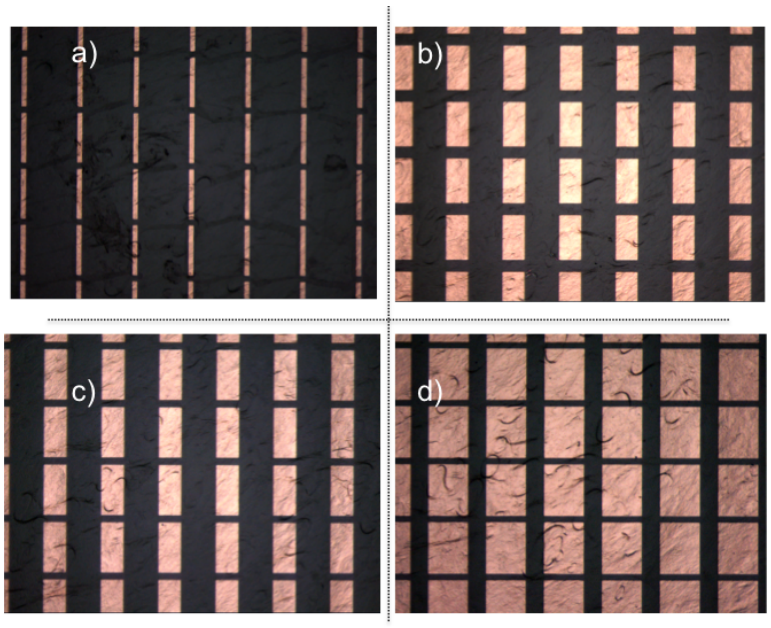

Figure 2.13: Image of fabricated rectangular patches.

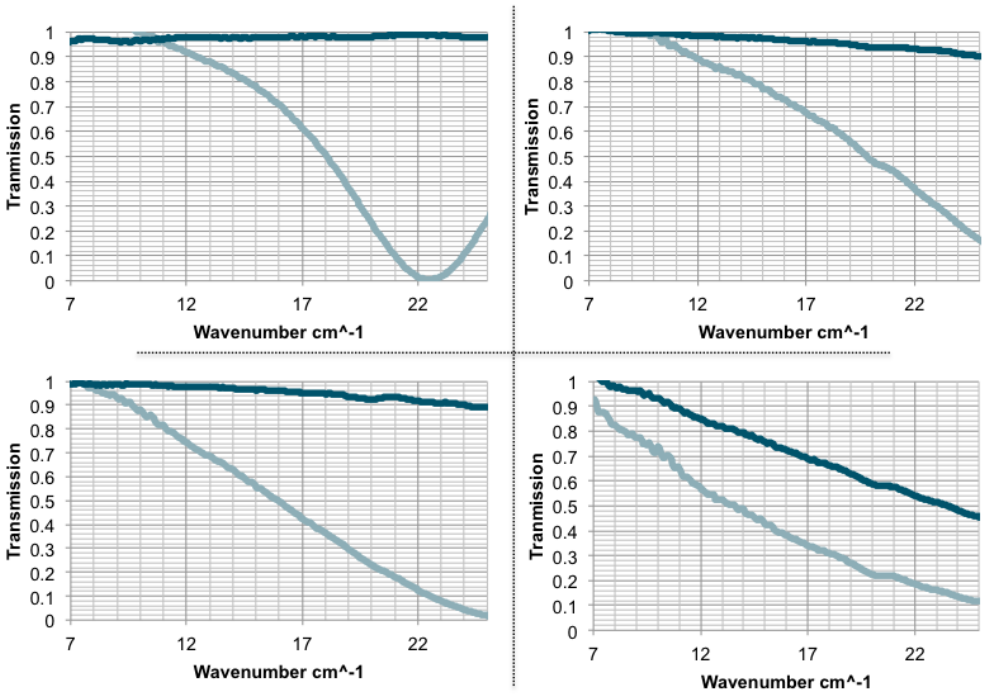

Figure 2.14: The measured transmission response for two orthogonal polarisations for each of the patches given in figure 2.12.

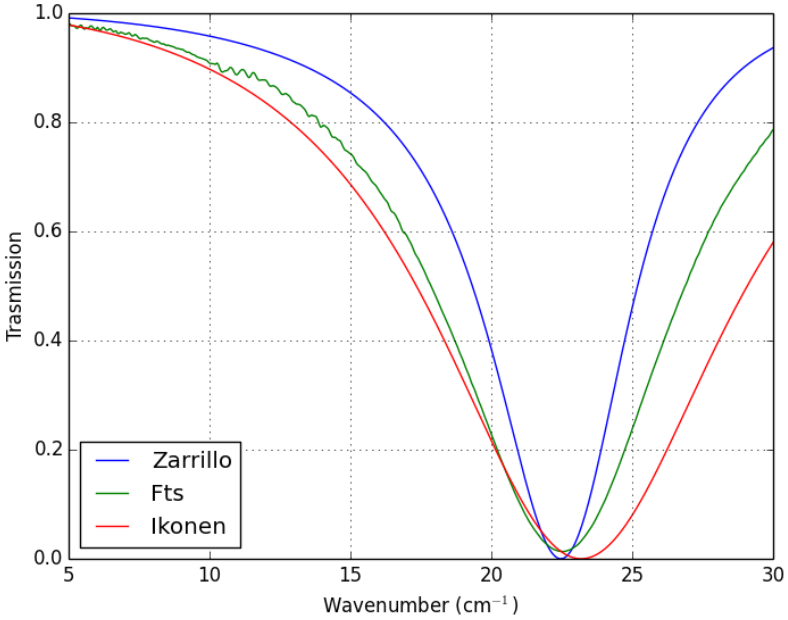

Figure 2.15: Comparison of the transmission line model and the measured data of the patch give in 2.12a.

2.6 Conclusions and Future Work

This chapter has shown how it is possible to create a transmission line model to represent multiple dielectric layers. The metal mesh grids have the ability to act as low or high pass filter depending on their geometry. It is possible to include them into the transmission line model by representing them as an equivalent circuit. This gives a simple way to predict the behaviour of the girds just by defining their geometry. A number of different equivalent circuit models were tested, but it was found that Timusk gave the best approximation. In all of these cases the absorption losses of the substrate were ignored. This was then verified by looking at the absorption in polypropylene.

It was also shown that it is possible to represent a anti symmetric girds such as a rectangular patch. Since the symmetry is now broken, the response of each patch depends on the orientation of the incident polarisation. The analytical models that describe this geometry were found not be as accurate as the equivalent models for the symmetric grids. However, it can still be used to get an approximation of the performance of the structure.

Further improvements can be made to this model by using a method of moments (MoM) approach to model the grid structure [26]. This allows for the higher order current modes that occur in the structures to be considered. It is also capable of calculating the

transmission of any arbitrary shaped patch. However, to implement this into the model is non-trivial and would take considerable time.

This page was intentionally left blank

Chapter 3

Equivalent Refractive Index Theory and Applications

3.1 Using a FSS to build an artificial dielectric

The previous chapter showed how the geometry of a single gird can be changed to adjust its filtering properties. Grids of different geometry's have also been combined to create devices which have specific passbands [6]. This chapter aims to show how it is possible to combine multiple grids so that it mimics a bulk dielectric with a given refractive index. The advantage of creating these artificial dielectrics is that the structure can be tuned to have a wide range of refractive index profiles, which are not found in natural materials. By understanding the range of possible values such a structure can take, it opens up a number of new optical devices that can now be constructed, since it is now possible to control the refractive index artificially.

The structure for creating an artificial dielectric is based on stacking a series of capacitive patch grids of the same geometry with a uniform spacing. This is illustrated in figure 3.1. The spacing between layers is filled by a dielectric, which for all examples and devices detailed throughout is polypropylene, which has a refractive index at mm- and sub-mm wavelengths of $n = 1.49$. The reasons for the dielectric gap filler can be found in the manufacturing techniques or, since it is possible to fuse the layers together without distorting the layer geometry or changing the layer inter-layer thickness. It has also been

shown to have very low absorption loss at sub-mm wavelengths. This construct allows for 3 different parameters which affect the refractive index, the patch size, a/g, the unit cell size, g and the spacing between layers d. It will be shown that the number of layers beyond the first few, thus the over all thickness of the slab, does not have a large impact on the effective index, just like a regular dielectric.

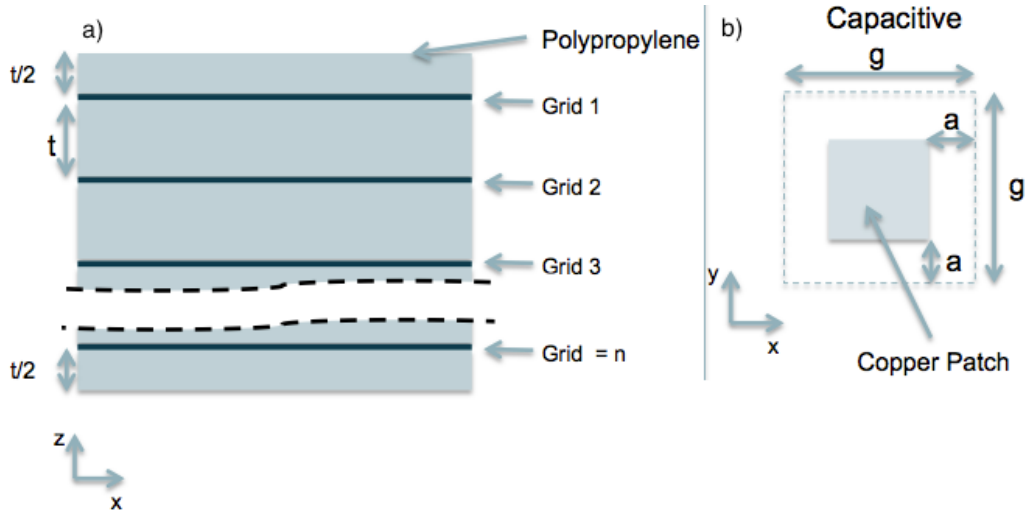

Figure 3.1: Grid configuration for making an artificial dielectric. a) Individual gird layers are stacked on top of each other, with a given spacing. b) The unit cell that is used in the girds.

A typical transmission response for an artificial dielectric is given in figure 3.2. This highlights the important considerations which must be made when designing a structure for a given application. It can be seen that there is a frequency cut off that occurs, where transmission decreases rapidly to zero. This is due to the capacitive patch grids used which are inherently a low pass filter, the point at which the cut off occurs depends on the chosen geometry. This inherent property combined with the Fabry-Perot effect that occurs leads to an equivalent dispersion effect in the structure, which causes the effective refractive index to increase as the cutoff approaches.This means that when designing these structures for a given application, the required operational bandwidth must be placed at wavenumbers well below where these effects occur.

3.1.1 Parameter extraction

The properties of the grids should be more strictly described in terms of the permittivity and permeability of the material. However due to the non-resonating nature of the geom-

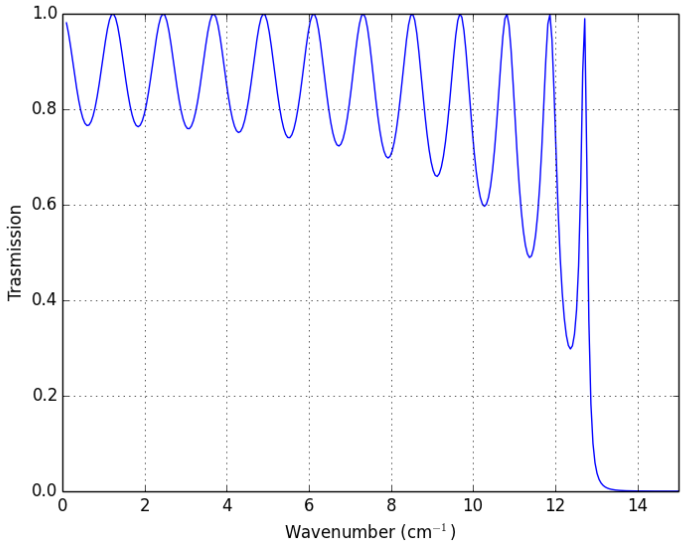

Figure 3.2: Typical transmission response for an artificial dielectric. There is a frequency cutoff that occurs due to filtering properties of the capactitve grids.

etry of the grid structure used, it can be assumed that $\mu = 1$ for all the structures used here [27]. Also, that the permittivity of the structures is $\epsilon > 1$, though the lower limit is set based on the spacing material used. This means that the effective index will always be greater than one. For consistency the artificial dielectric will be defined in terms of the effective refractive index, $n_{eff} = \sqrt{\epsilon_{eff}}$.

This means that the structure can be described in the same way as a bulk dielectric. Allowing for the same techniques to extract the refractive index can be applied. One approach is to use the Fabry-Perot (FP) intensity formula. This gives the transmission response of a parallel plate dielectric slab by taking into account the standing wave between the interfaces of the slabs. This is represented by equation 3.1, where n is the refractive index of the material, $\tilde{\sigma}$ is the wavenumber separation between transmission peaks and Δx is the thickness of the material . In an ideal case, this function could be fitted to the simulation and then the refractive index extracted. Due to the presence of the frequency cutoff that occurs as well as weak dispersion, it is not always practical to fit the FP curve. Instead a first order approximation can be made by measuring the transmission that occurs at the first minimum, from which the refractive index can be found from equation 3.2. This only describes the refractive index at a single frequency. However, it has been shown [27] that for frequencies far away from the cutoff, there is only a slight variation in the effective index.

$$T(\tilde{\sigma}) = t^2 = \frac{1}{1 + [2r/(1-r^2)]^2 sin^2(2\pi n\tilde{\sigma}\Delta x)} \tag{3.1}$$

$$T_{min} = (\frac{4n^2}{n^2+1})^2 \tag{3.2}$$

There are many other techniques in the literature to retrieve the material parameters of a meta material structure directly from the S- parameters [28] [29]. These can be applied to theoretical or practical results to see how the material parameters vary with frequency. However, in many cases they are limited by the fact that they assume that the wavelength in the medium is much larger then the slab thickness, which is not the case here. These techniques are required for more complex structures, such as split ring resonators, that have negative material parameters at wavelengths close to that of resonance[11]. Since the structure under study here does not have any resonant features, the material parameters can be retrieved using the classical FP formula. Another reason for which this is not a major concern is that for the initial structures in mind, it is assumed that the material is non dispersive, so only a first order approximation of the effective index is required. A more practical technique is discussed in section 3.4 that allows for more precise prediction of dispersion effects in an electrically large medium.

3.1.2 Verification of Transmission Line model.

It has been shown how a single stack of grids can behave as a material with a single refractive index. However, to build a device that requires multiple refractive index values such as a graded index profile, many different geometries are required. To do so the transmission line model developed in chapter 2 must be used. While there is good agreements with the TL model for a single grid geometry, the effects of the spacing between grids must be explored and validated independently via finite element analysis (HFSS).

To do this, multiple structures each with different spacings are modelled both in the TL model and HFSS. The chosen structure has a geometry with $g = 200um$ and $a/g = 0.05$ and will consist of 20 grids. Figure 3.3 shows the comparison between models with a $100um$ spacing. It shows a strong agreement between the two methods and shows that the

TLM accurately predicting the cutoff. By reducing the separation down to 60um, Figure 3.4 shows that there is a slight deviation between results, but still yielding a reasonable approximation. However, by halving the separation to 30um, larger discrepancies can be found between models, figure 3.5. The reason for the disagreement is due to the capacitive coupling effects that occur between the two layers [30]. This a fundamental limit in the equivalent circuit representation, since the approximation does not take into account any of the currents that occur on neighbouring patches. However, at close separations the physical structure is still behaving as an artificial dielectric since in the HFSS data Fabry-Perot fringes are still visible.

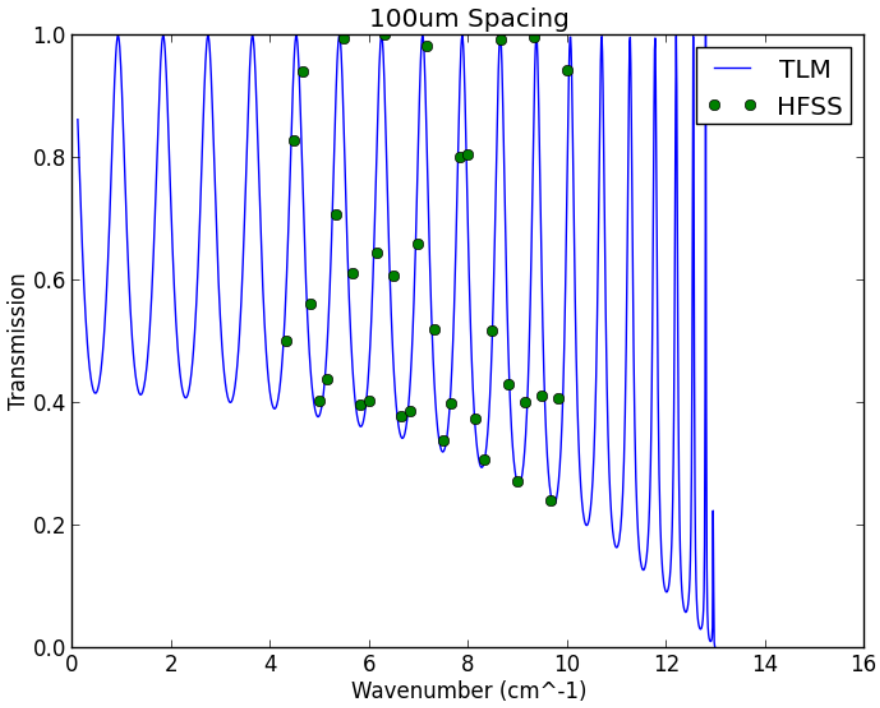

Figure 3.3: Model comparison between Transmission Line and HFSS at 100um spacing. This shows that there is good agreement between the two different simulations.

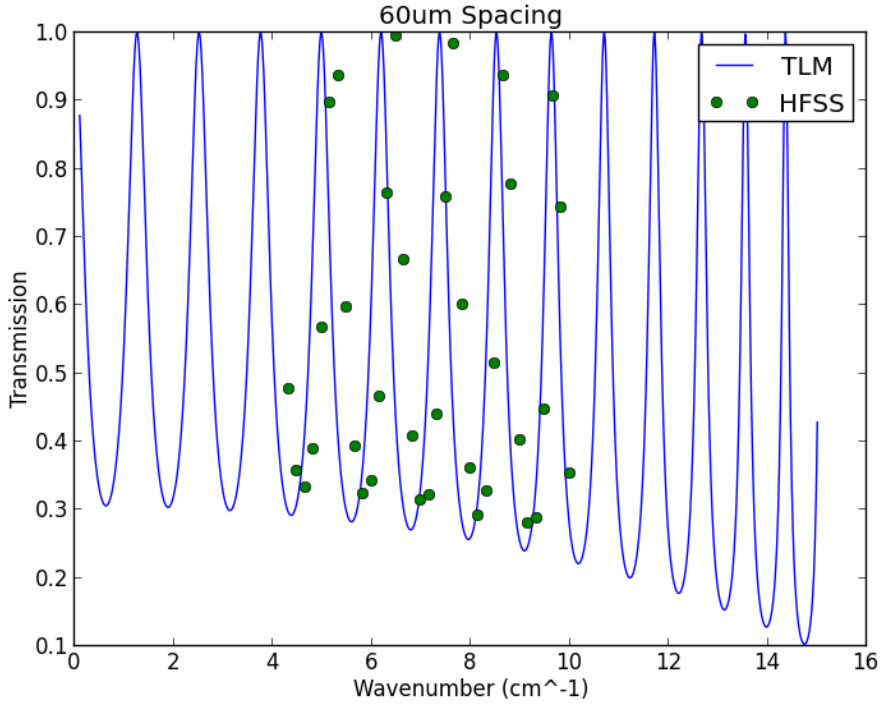

Figure 3.4: Model comparison between Transmission Line and HFSS at 60um spacing. There is now some discrepancy occurring between the two models.

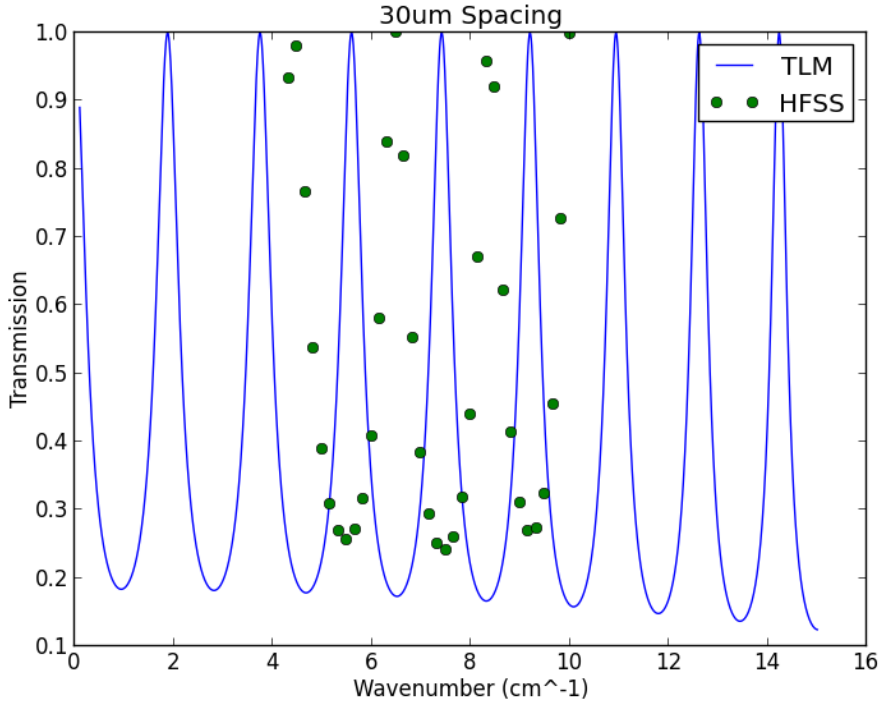

Figure 3.5: Model comparison between Transmission Line and HFSS at 30um spacing. This shows that there is poor agreement between the two different simulations

3.2 Exploring obtainable effective refractive indices

Using the TL model, it is now possible to explore the range of possible effective refractive index values that can be obtained using this structure. There are four possible parameters that can be varied to see their effect on the effective index. Firstly the number of layers is investigated. By increasing the number of layers while fixing the geometry, figure 3.6 is produced. This shows that the transmission value of the first minimum is the same for all, thus the effective index remains the same. The only thing that is observed to change is the number of fringes. This is the exact same behaviour that occurs when the thickness of a bulk dielectric is changed. It should also be noted that the cut off frequency remains consistent for more than 3 grids.

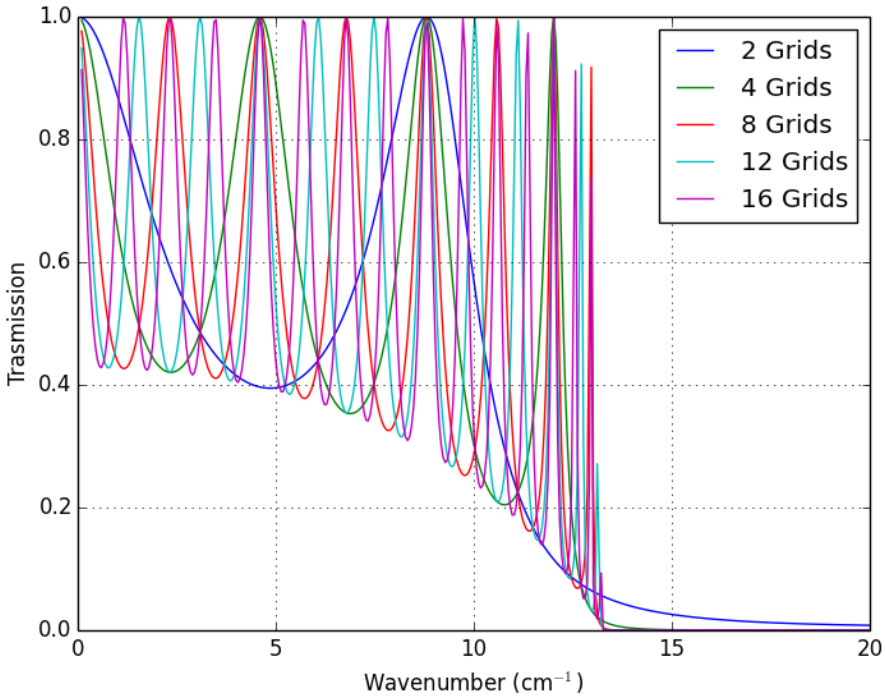

Figure 3.6: Transmission profile for increasing number of grids with the same geometry. The overall transmission response stays the same, but the number of fringes increases.

Now that it has been shown that the number of layers does not affect the effective index, the next step is to look at the effect of the spacing between layers. Figure 3.7 shows the effect that changing the spacing between layers has on effective index. It shows that as the layers are brought closer together, the effective index increases. However, it also shows that as the spacing between layers decreases the cutoff occurs is shifted to a lower

frequency.

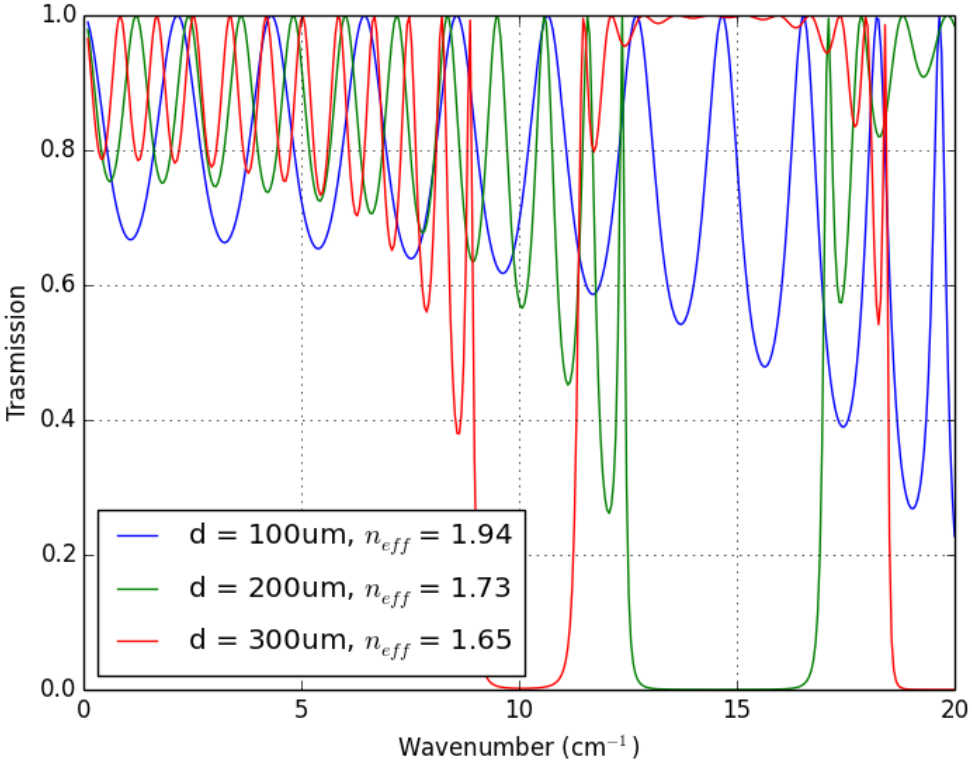

Figure 3.7: The effect of the transmission profile, when inter layer spacing is changed. The effective index decreases with distance.

This leaves the two final parameters to vary, the unit cell size, g and the patch size a/g. Figures 3.8 -3.10 show a parameter sweep of these two parameters, at different separations. From all of these results it can be seen that the most sensitive parameter to vary is the patch size, a/g. The structure will always have $n_{eff} = n_{substrate} = 1.5$ when $a/g = 0.5$ since this corresponds to a patch size of zero. Therefore, the unit cell size g sets the maximum obtainable index value and the rate at which the effective index decreases down to the minimum value. Also as expected, increasing the spacing of the grids, lowers the maximum obtainable effective index.

Determining the maximum obtainable index depends entirely on the application required. From the results above, the highest theoretical index is achieved when the spacing is as small as possible, the cell size is as large as possible and patch size as big as possible (a/g approaching zero). However, in most practical applications this can not be realised. Firstly, the basic principle of any metamaterial is that the periodicity of the structure

must be far smaller then the wavelength, to avoid diffraction effects. This means that the frequency cutoff occurs at lower frequencies as the unit cell size increases. For applications where a graded refractive index needs to be created in a two dimensional space, placing of the elements is much simpler when the periodicity of the cell remains constant. There may also be a limit on the smoothness of variation in index from one cell to another. For a larger unit cell size and smaller a/g values, where the rate of changed of index is the greatest, some precise values may not be obtainable due to the etching resolution limitations in the manufacturing process. Finally, there is a practical limit to the minimum spacing that can be used. For real bulk dielectrics there will be a required thickness. Therefore, thicker devices with closer spacings require more layers, which makes the deice more costly and complex to fabricate.

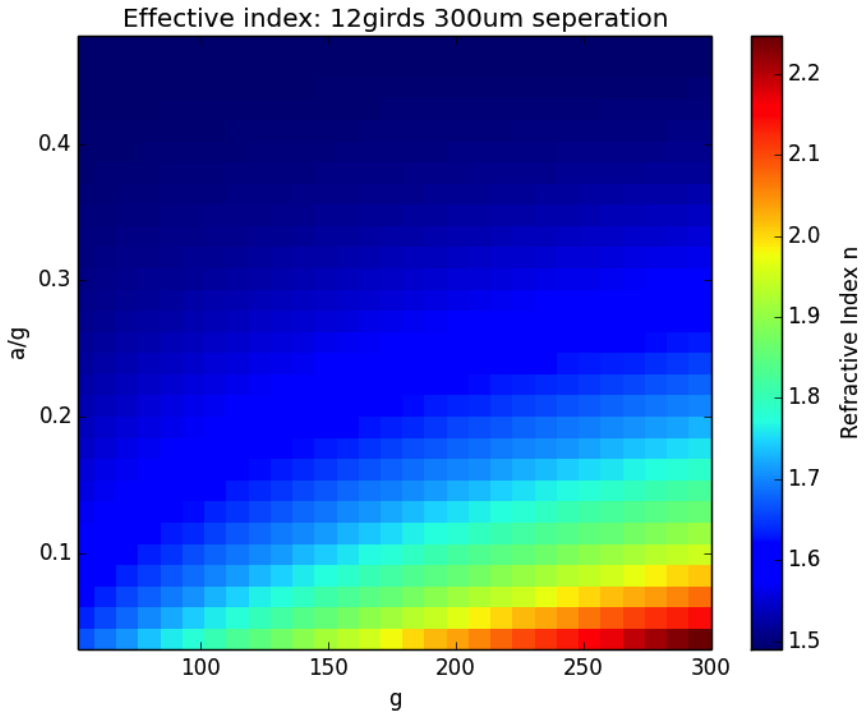

Figure 3.8: Effective index value as a function of unit cell size and patch size, with a separation of 300um.

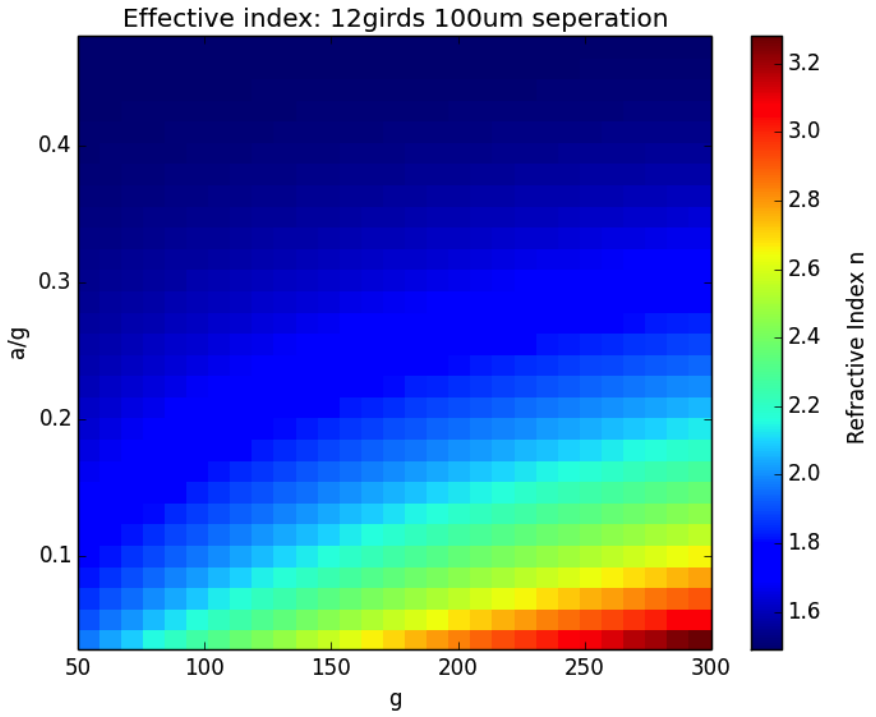

Figure 3.9: Effective index value as a function of unit cell size and patch size, with a separation of 100um.

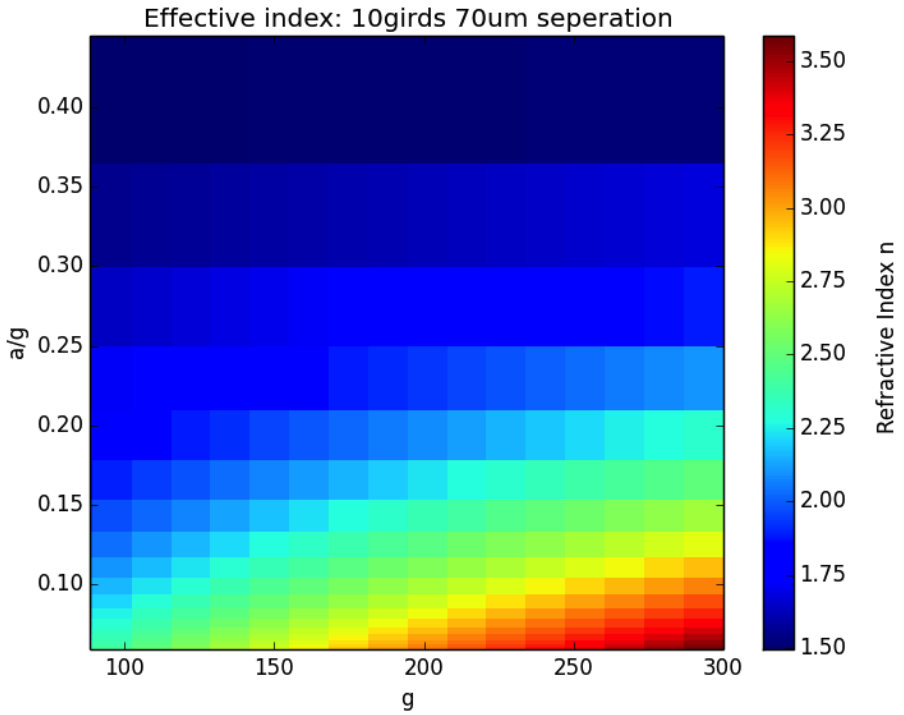

Figure 3.10: Effective index value as a function of unit cell size and patch size, with a separation of 70um. As the spacing moves closer together, the effective index increases.

3.3 Misalignment of grids

In the modelling above, it is assumed that geometry configurations are perfectly aligned. In practise, due to uncertainties in the manufacturing process this is not possible, there will be some mis-alignment between the different layers. To measure the effect this has on the overall effective index, a series of simulations in HFSS were performed. Two different cases are considered, firstly a randomly organised stack is shown in figure 3.11 and then a periodically mis-aligned stack, in such a way that each patch is shifted by half a unit cell, figure 3.12.

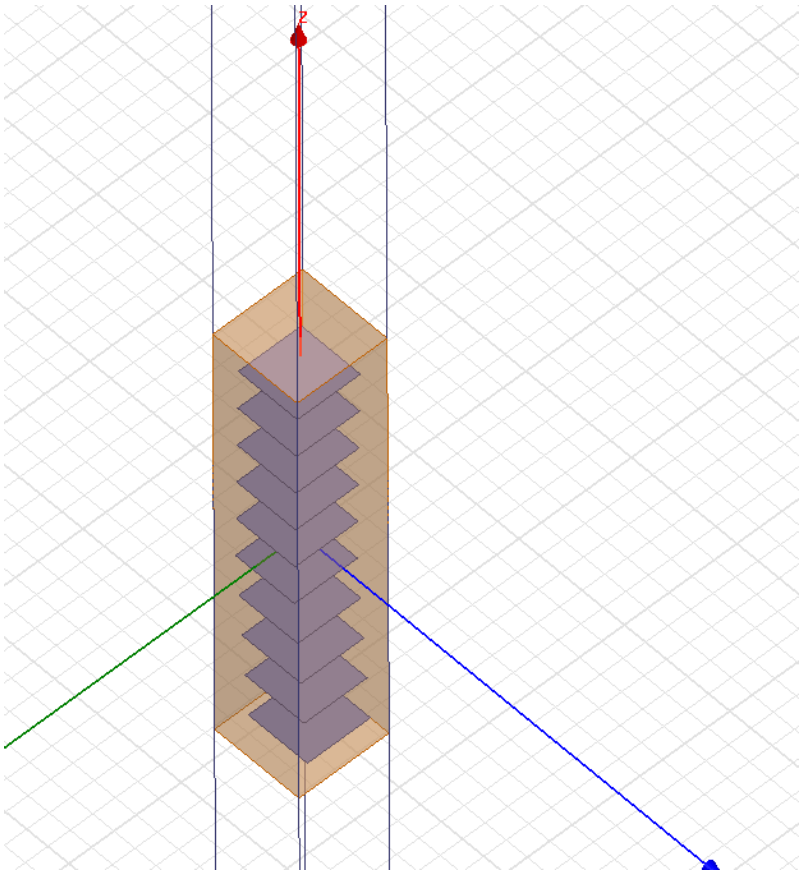

Figure 3.11: Randomly aligned stack of grids as simulated in HFSS to test if it had an effect of the effective index value.

The transmission results for each of these structures is shown in figure 3.13. The solid blue curve represents transmission through a perfectly aligned structure. The randomly aligned structure is over plotted and has the exact same transmission response. This shows that the exact placement of the grids is not critical to its operation. In the case of the offset grids given in figure 3.12, the results show that when the polarisation is aligned

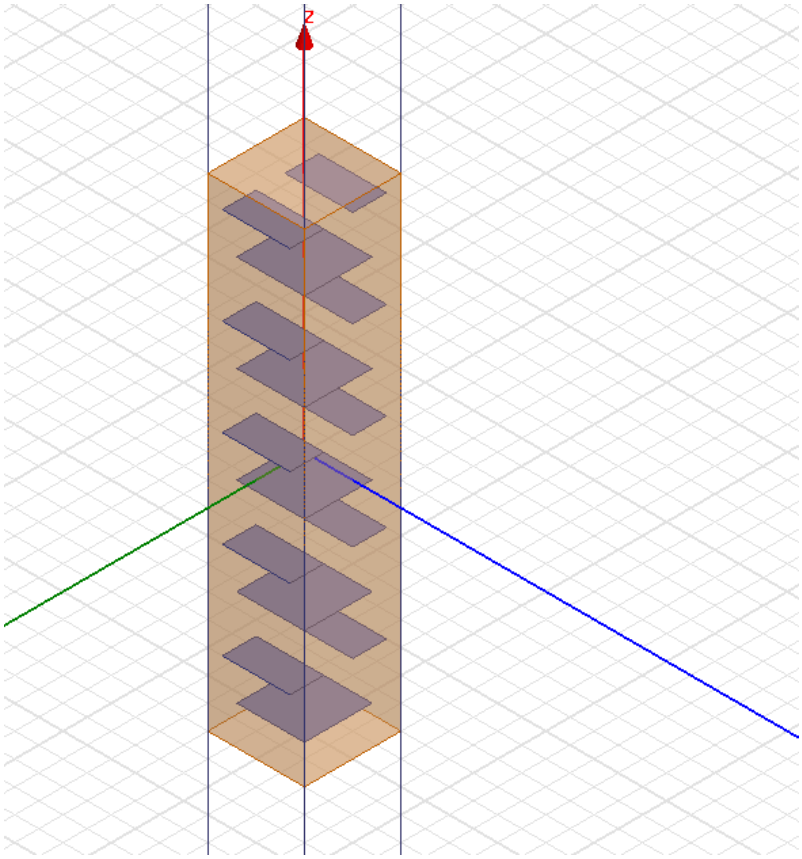

Figure 3.12: Periodically offset grids.

in the direction of the periodic offset there is a slight shift in the transmission profile, while there is no change for the other polarisation. This shift in the transmission response corresponds to a difference in refractive index of $\Delta n = 0.2$.

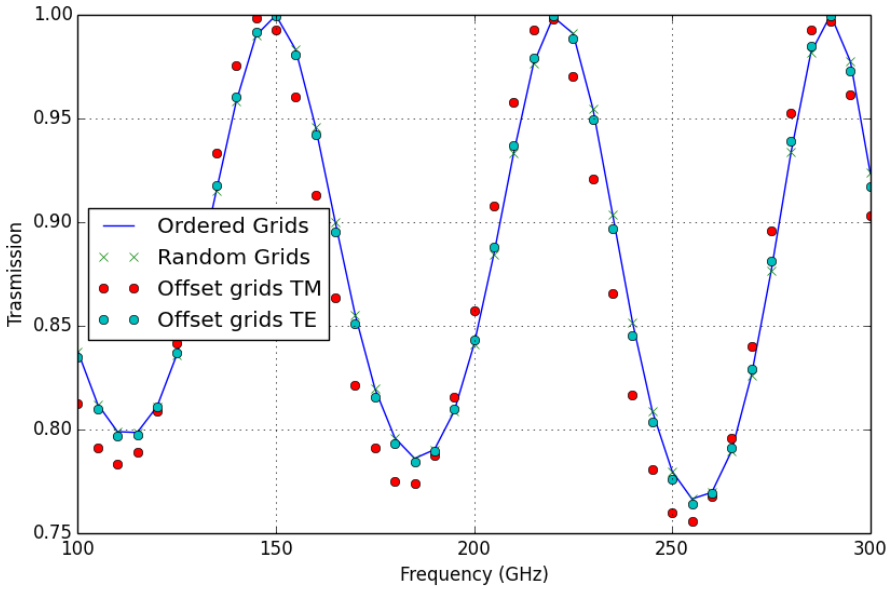

Figure 3.13: Comparison in transmission profile of differently stacked grids that shows that there is no change in the random girds, but a slight change in the periodically misaligned grids.

3.4 Describing the band structure of an artificial dielectric

The transmission line model for these regular periodic structures has been shown to be as accurate and much faster then HFSS to calculate the effective index. However, for some applications the exact behaviour of the frequency cut-off and dispersion of the structure are required. While this can be found using the methods previously described, there is another way to obtain this information.

Since it has been shown that the number of layers does not affect the value of the effective index, but only the number of transmission peaks, it is possible to let the number of layers increase to infinity. This ideal infinite periodic structure can now be described using Bloch waves[31],. By using the same approach used for 1D photonic crystals, the band structure can be determined, from which the allowed transmission regions and its dispersion behaviour can be found.

Following the method outlined by Kaipa [31], the dispersion equation for the Bloch waves is given by equation 3.3, where k_B is the the Bloch wavenumber, $\phi = \beta_d h$ is the electrical thickness of the slabs, D is the gap between patches and b is the normalised admittance for the capacitive grid given by equations 3.4a-3.4c. The Bloch wavenumber is

real for allowed transmission regions and imaginary for forbidden regions. It is real when the frequency region is such that $|cos\phi - b/2 sin\phi| < 1$.

$$cos(k_b h) = cos\phi - \frac{b}{2} sin\phi \tag{3.3}$$

$$b = \frac{\omega C_g^{TE}}{Y_d^{TE}} \tag{3.4a}$$

$$C_g^{TE} = \frac{2D\epsilon_{eff}}{\pi c \eta_0} ln\left[csc\left(\frac{\pi g}{2D}\right)\right] \tag{3.4b}$$

$$Y_d^{TE} = \frac{\sqrt{\epsilon_r - sin^2\theta}}{\eta_0} \tag{3.4c}$$

From these relations, the Bloch wavenumber can be plotted to show the band structure. Figure 3.14 shows the band structure for a grid geometry of $g = 200um$ and $a/g = 0.2$. This shows two transmission bands, $0 - 21$ wave numbers and 33-46 wave numbers. This result can be compared to the same structure modelled using the transmission line method. This is shown in figure 3.15 for a stack of 20 grids. It can be seen that the two pass bands match up in the same place.

The effective refractive index can be directly extracted from the Bloch wavenumber by equation 3.5. When applied to the structure above, figure 3.16 is produced, with the corresponding transmission profile over-plotted. This shows that there is a slight increase in effective index with frequency as expected, but, the most drastic change occurs near the frequency cutoff.

$$n_{eff} = \frac{k_b}{h 2\pi \lambda} \tag{3.5}$$

3.4.1 A graded index flat prism

The advantage of using the band structure to model a artificial dielectric is that it is possible to design a device that uses the dispersion that occurs in the structure. Below is an outline of one of the most common devices that use this, a prism.

A traditional optical prism exploits the dispersion of the glass medium and has its

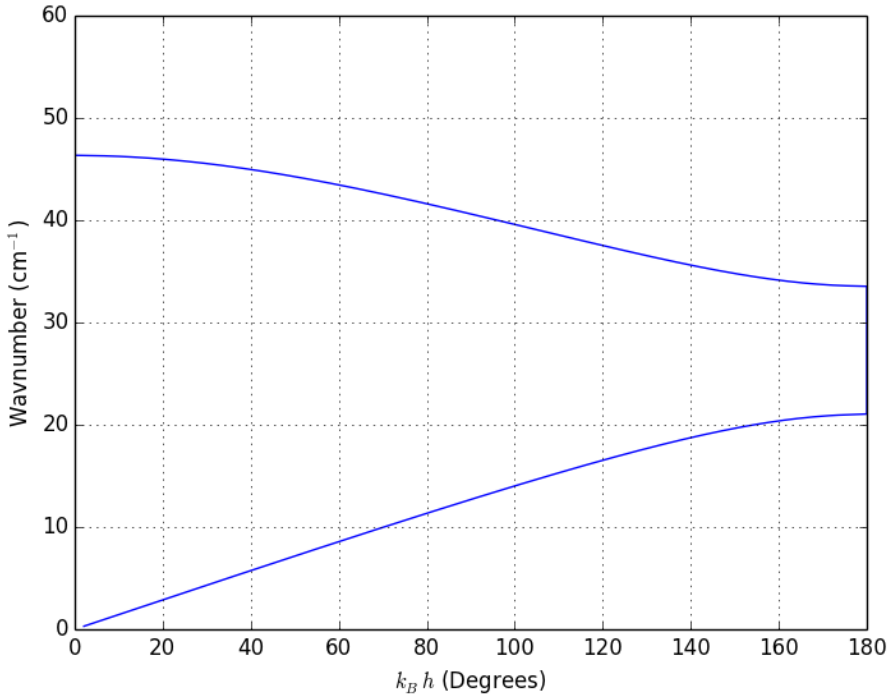

Figure 3.14: Band digram showing allowed transmission regions. It shows that no transmission will occur between 20 and 32 wave numbers.

faces cut such that each wavelength refracts with a different angle, causing a spectrum to be produced. In the examples above, it is shown that as the wavelength approaches the cut off frequency, there is a rapid change in effective refractive index, which is the same that occurs in a prism. However, it is only possible to create a planar structures using these grids, therefore another means to refract the light must be found.

The solution to this is to create a device that has a linear graded index. It has been shown [32] that there is a relationship between the overall index gradient of a slab and angle at which a plane wave will be refracted when passing through it (equation 3.6).

$$dn(x) \approx dx sin\theta / t \tag{3.6}$$

Therefore, if it is possible to design a structure where $dn(x)$ is a function of frequency then θ would also become a function of frequency, which would mimic a prism. To see if such a gradient structure is possible, a parameter space which explores the relation between patch size, frequency and effective index is required. The spacing and unit cell

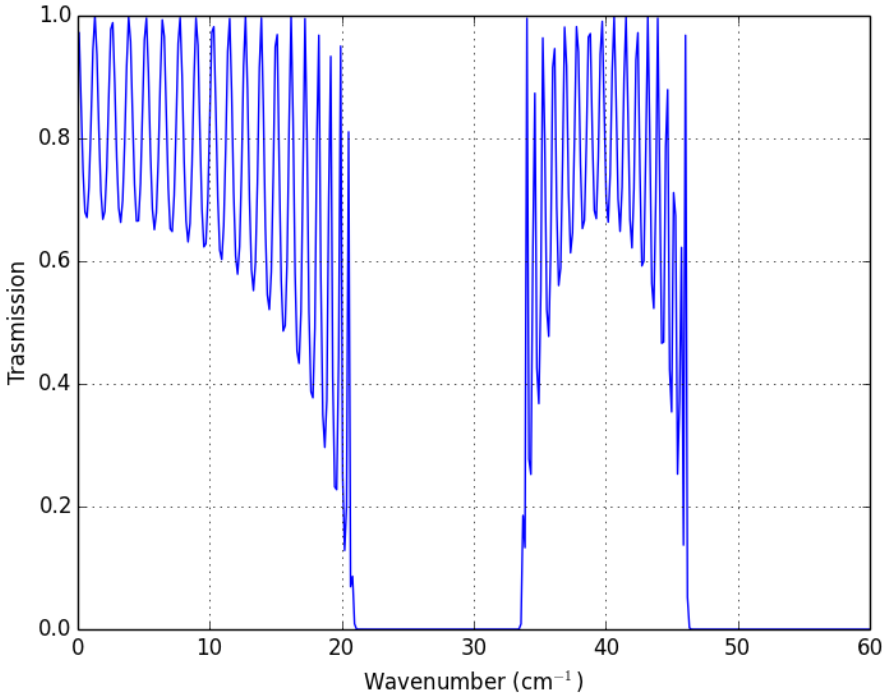

Figure 3.15: Corresponding transmission profile calculated with transmission line model.

size remain constant throughout the whole structure. From this parameter space (figure 3.17) it shows that the rate at which the effective index changes is different for each patch size. This means that for a given array of increasing patch sizes, the overall index gradient will change with frequency.

Assuming just a linear change in patch size, figure 3.18 is produced by using the parameter space to calculate the expected angle of refraction assuming unit thickness. This shows that the dispersion effects of the grid could vary enough to give a suitable range of diffraction angles.

The exact behaviour and design of such a device still need to be investigated, but this shows that how the dispersion effects of the grids could be exploited to precisely steer light based on its frequency in way that is not possible using existing diffraction gratings.

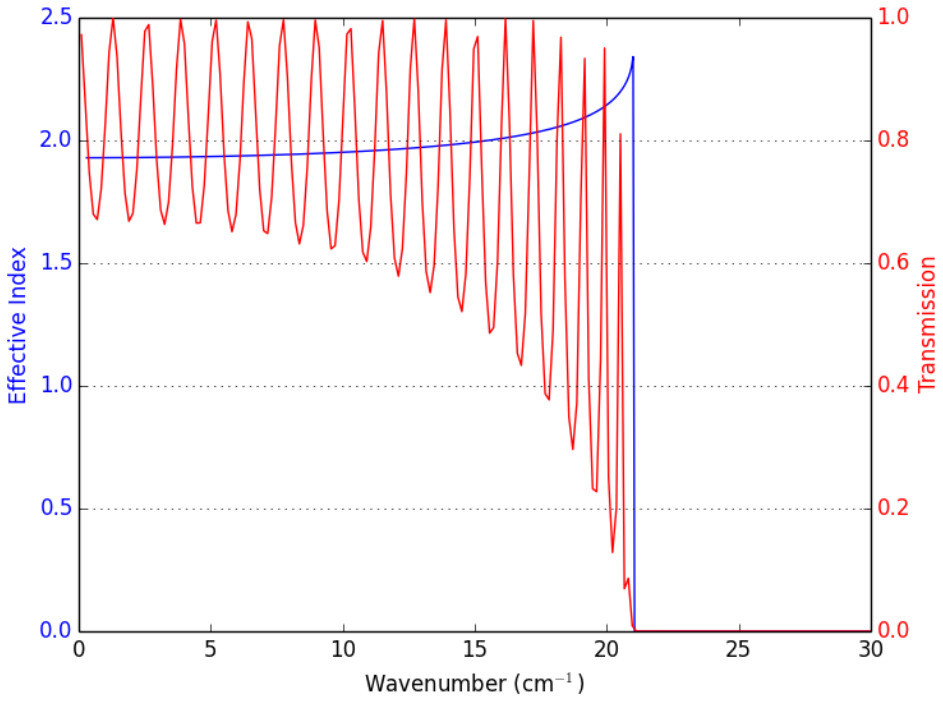

Figure 3.16: The full dispersion relation for a given stack compared to the transmission profile.

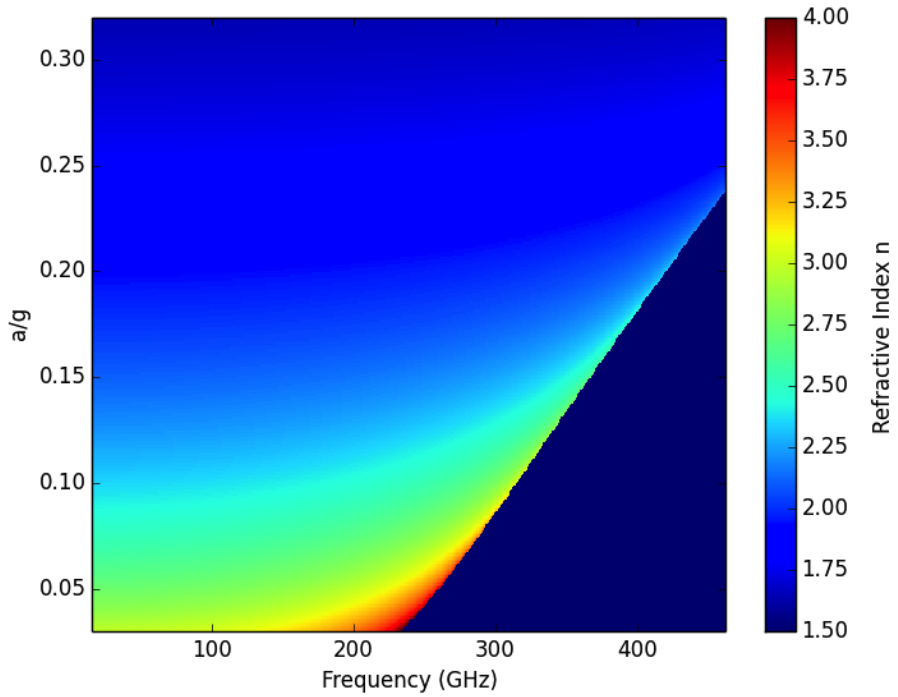

Figure 3.17: The rate at which the effective index increases as is approaches the cutoff frequency is different depending on patch size.

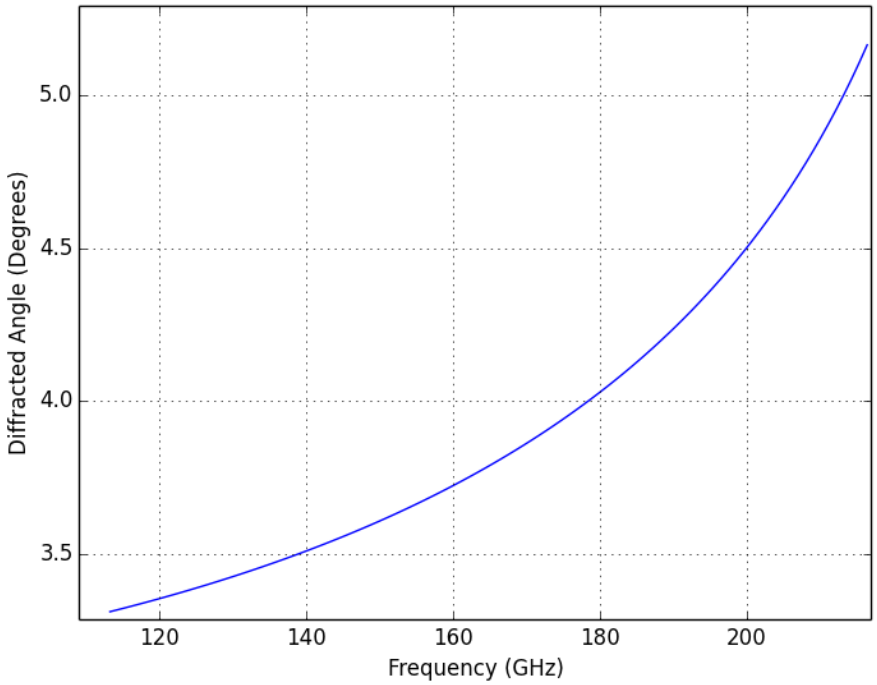

Figure 3.18: The deflection caused by an array of linearly increasing patches, based on the approximation of equation 3.6

3.5 Artificial Birefringence

After demonstrating that an artificial dielectric can be built using a stack of square patch girds, it can now be extended to create an artificial birefringent material. A birefringent material is such that it has two perpendicular optical axis, each with their own refractive index. This means that the structure is now sensitive to the orientation of the incident polarisation.

This symmetry breaking can be achieved by using a rectangular patch structure which was detailed in Chapter 2. From the tests of the single grid structures, it was shown that there there there two distinct transmission responses when the polarisation is aligned with the axis of the unit cell. Therefore by combining the rectangular girds into a stack, there would be two distinct Fabry-Perot transmission profiles, thus two effective refractive indexes, one for each polarisation.

To verify that a stack of rectangular patches is sensitive to different polarisation as predicted, the structure given by figure 3.19, was modelled in HFSS. Figure 3.20 shows this result of two linearly polarised plane waves incident along each of the main axes of the unit cell. It can be seen that there are two different Fabry-Perot resonances, thus two different effective indices. It was also found that there was no cross-polarisation generated by the structure.

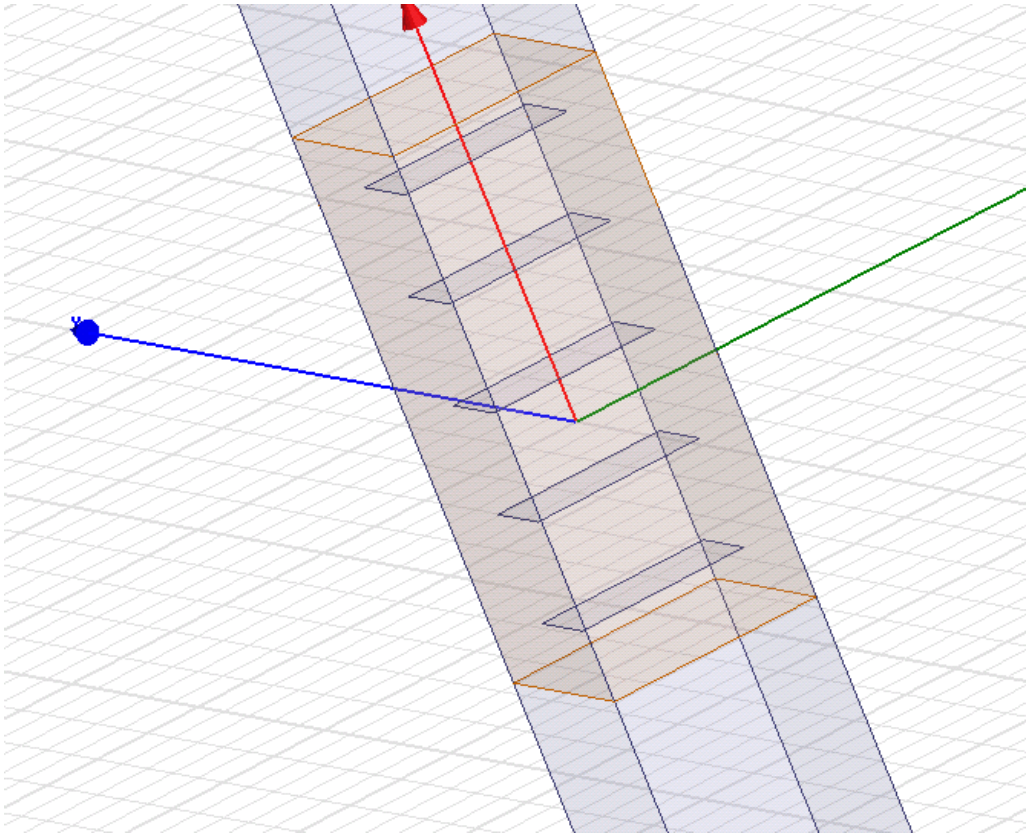

Figure 3.19: HFFS structure. Copper patches embedded in polypropylene.

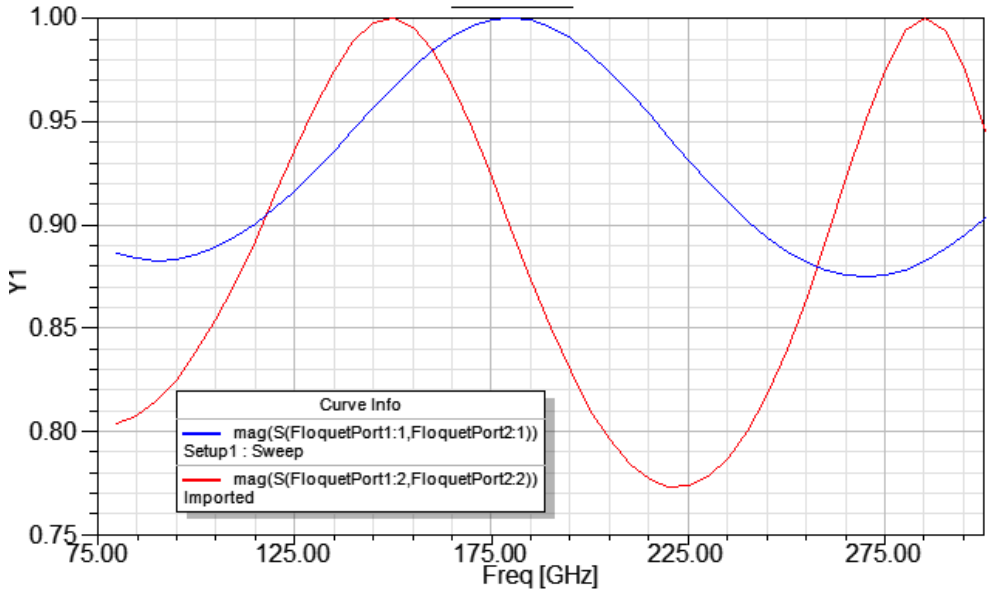

Figure 3.20: Modelled transmission for each polarisation through the structure.

3.6 Conclusion

It has been shown that it is possible to create an artificial dielectric by stacking a series of capacitive girds with a regular separation. The parameter space performed, showed that it

is possible to get a range of different effective refractive indexes. However, it is important to keep into account other factors when trying obtain the highest possible value, such as frequency cut-off and the physical number of layers required to build it. It was also shown that this could be extended to create an artificial birefringent material by using a rectangular patch instead of a square, thus breaking the symmetry.

Finally, a different method was presented for modelling the girds by considering an infinite stack of mesh structures and solving for the Bloch wave number. From this the precise refractive index could be extracted for each frequency as well as where the frequency cut-off occurs. An outline of a possible flat prism design was presented, which shows how the dispersion effects of the grids could be exploited. To realise this device, further work is needed in understanding the exact behaviour of the linear gradient slab.

Chapter 4

GRIN Lens

4.1 Graded index lens design

With the ability to now create artificial dielectrics it is now possible to apply them to design a practical device. It was chosen it would be a gradient index flat lens. Such a lens would be able to replace existing polypropylene lenses, with something that is much less bulky and weighs only a few hundred grams. This first prototype would also act as a test to see if it was possible to vary the material parameters so that a graded index can be formed.

This first gradient index lens based on a metal mesh artificial dielectric or lenster (LENS filtER) has recently been produced [33]. The initial measurements were first made using a Fourier transform spectrometer (FTS), to test the overall spectral response of the lens. Beam y-cuts were also performed both at a single frequency (90GHz - below the design frequency) and with a broadband source. The limitation of this method is that the beam shape could not be measured at individual frequencies, so the exact chromatic nature of the lens could not be found. It was also not possible with the equipment available to make any direct phase measurements of the lens, to help identify the focus of the lens. These limitations have now been overcome with further measurements using a quasi-optical bench available at the European Space Agency (ESA-ESTEC).

4.1.1 Lens Recipe

The design of the lens is based on existing recipes for graded index lenses. This ideal design is represented as a smoothly varying refractive index profile, which is then realised by using a metamaterial, with the aim of matching the required index profile as closely as possible.

The chosen lens design is based on a Wood lens[34]. This lens has a radially varying refractive index profile as a second order function of the radius (parabolic), while maintaining a constant index in the z direction. This profile is determined by equation 4.1. The chosen design has a radius of 70mm and a focal length of 250mm. This design is similar to that of a typical polypropylene lens that is currently used in the testing of far infrared astronomy. The thickness of the lens is then set by the central index value, n_0 and the minimum index value at the edge of the lens. Which in this case is set by the substrate of the mesh grids, polypropylene.

$$n = n_0 - \frac{r^2}{2df} \tag{4.1}$$

To achieve this refractive index control, an equivalent index material, as described in Chapter 3, is used. Preliminary HFSS simulations show that closely stacked meshes show little variation in frequency as well as no polarisation discrimination, when the square geometry is employed. There are four parameters that are used to control the desired refractive index. The size of the copper patch, the unit cell size it occupies, the number of metal mesh layers and the separation between them. These four parameters allow a lot of freedom in tuning the desired refractive index. The maximum central index was chosen to be $n = 2.7$, this then sets the required thickness to be 2mm. This requirement constrains the number of layers and separation of grids that must be used. This leaves the cell size and patch size left to be determined. Since the required index profile is radial, the cell size is fixed and the patch size is varied to control the index. It assumed that by varying the patch geometry slowly, each element can still be treated as an infinite periodic structure, so that the existing modelling techniques can be used. The assumption has been applied before to design meta surfaces [35] [36], where the EM field propagates along the surface, instead of through it, as in this case. The final physical design consists of 20 identical mesh grids with a 100 micron spacing.

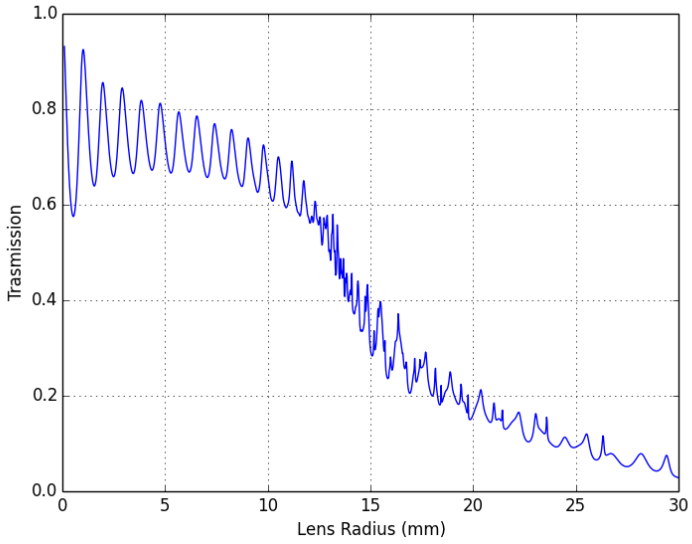

Figure 4.1: Predicted spectral transmission of the designed lens based on the transmission line model and integrated based on the spatial distribution of the grids.

4.1.2 Predicted performance

Using the TL model it is possible to model the overall transmission through this proposed lens design as a function of frequency. This is done by finding the transmission for each discrete value of n radially outwards from the centre of the lens. These results can then be combined to give a normalised transmission across the whole lens, figure 4.1. This is based on the assumption that a plane wave will strike the lens so it is illuminated uniformly. This predicts that the lens will be broadband, operating frequency up to 300GHz before a loss of performance. The loss of power in these transmission regions is due to the impedance mismatch with free space. The lens overall transmission tapers off as the frequency increases due to the fact that the relevant cut-off frequency characteristic of the capacitive geometry decreases towards the centre of the lens as the copper patch slowly fills the periodic mesh becoming opaque.

4.2 Further measurements

4.2.1 Quasi-Optical bench

The quasi-optical bench available at ESA is designed to characterise the material properties of samples by measuring the transmitted and reflective power through it. This is a free-

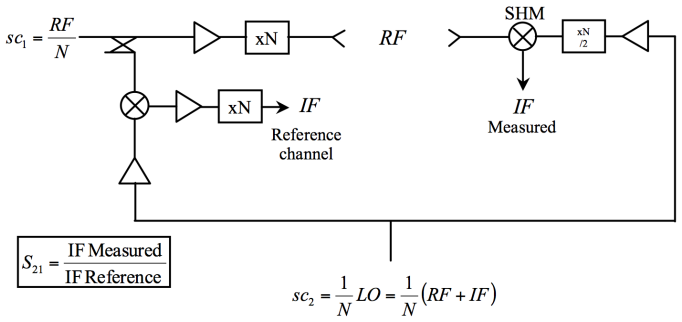

Figure 4.2: Schematic representation of the frequency extension units. Both reciver and transmitter are fed by a common local oscillator (LO) signal

space measurement system that uses corrugated horns connected to a network analyser to both launch and receive the electro magnetic radiation. The use of corrugated horns, means that they have a high gain, which in turns means that the beam is well contained. The beam is focused using aluminium of axis parabola mirrors, which have a set focus.

The frequency range of operation of the optical bench is 50 - 500 GHz divided in 6 frequency bands: 50-75 GHz, 75-110 GHz, 110-170 GHz, 170-260 GHz, 220-325 GHz, and 325-500 GHz. These are the frequency bands that are dictated by the Solid State Frequency Extension Units , which are based on multipliers and mixers. A schematic representation of the units is shown in Figure 4.2. The receiving channel has a sub harmonic mixer (SHM) which is used to de-multiply the incident signal with a local oscillator (LO) This outputs a intermediate frequency (IF) which can be measured by the VNA.

The 50-75 GHz and 75-110 GHz modules are commercial HP extenders. The 110-170 GHz and 170-260 GHz are internally developed based on VDI components [37]. The resolution in frequency achieved in these measurements is about 100 MHz. The physical positioning and curvature of the ellipsoidal mirrors is such that at the sample holder position the field can be approximated as a plane wave. A picture of the quasi-optical bench in transmission configuration is shown in Figures 4.3 ,4.4

4.2.2 Measurement setup

To measure the lens, this setup has to be changed, since the distribution of the field produced must be observed directly. This is achieved by removing the secondary mirror and placing the receiver module on a movable x-y stage, as shown in Figures4.5, 4.6. In this configuration, the field behind the lens can be scanned with a minimum resolution of 1mm. However, since these adjustments must be made manually, this sets a practical limit

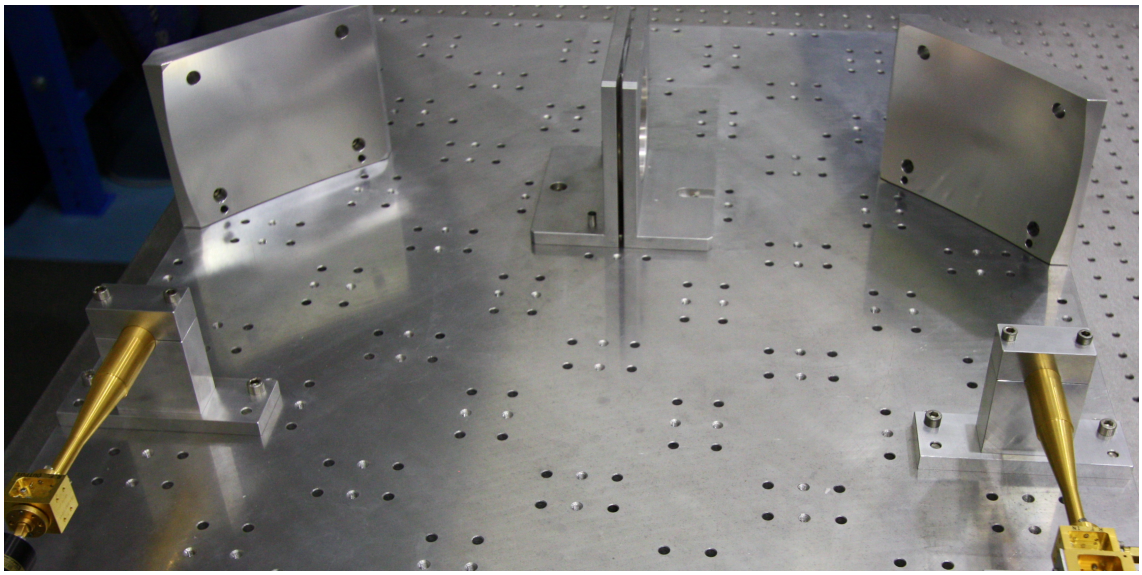

Figure 4.3: Quasi-optical test bench in transmission configuration: corrugated horns, elliptical mirrors and sample holder.

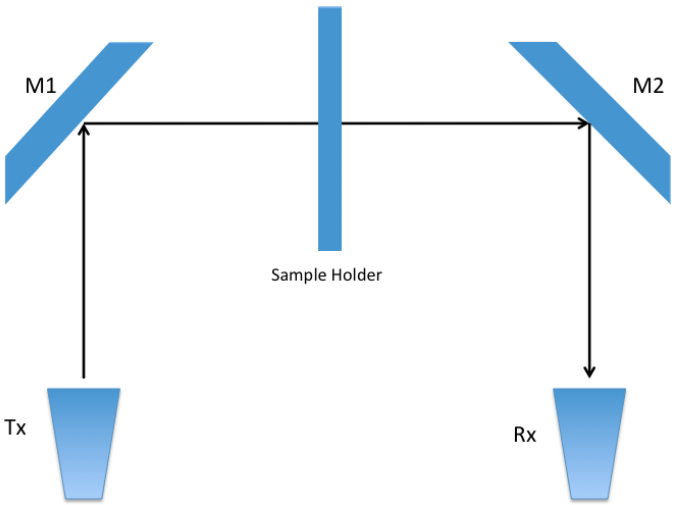

Figure 4.4: Schematic of Quasi-optical test bench in transmission configuration:.

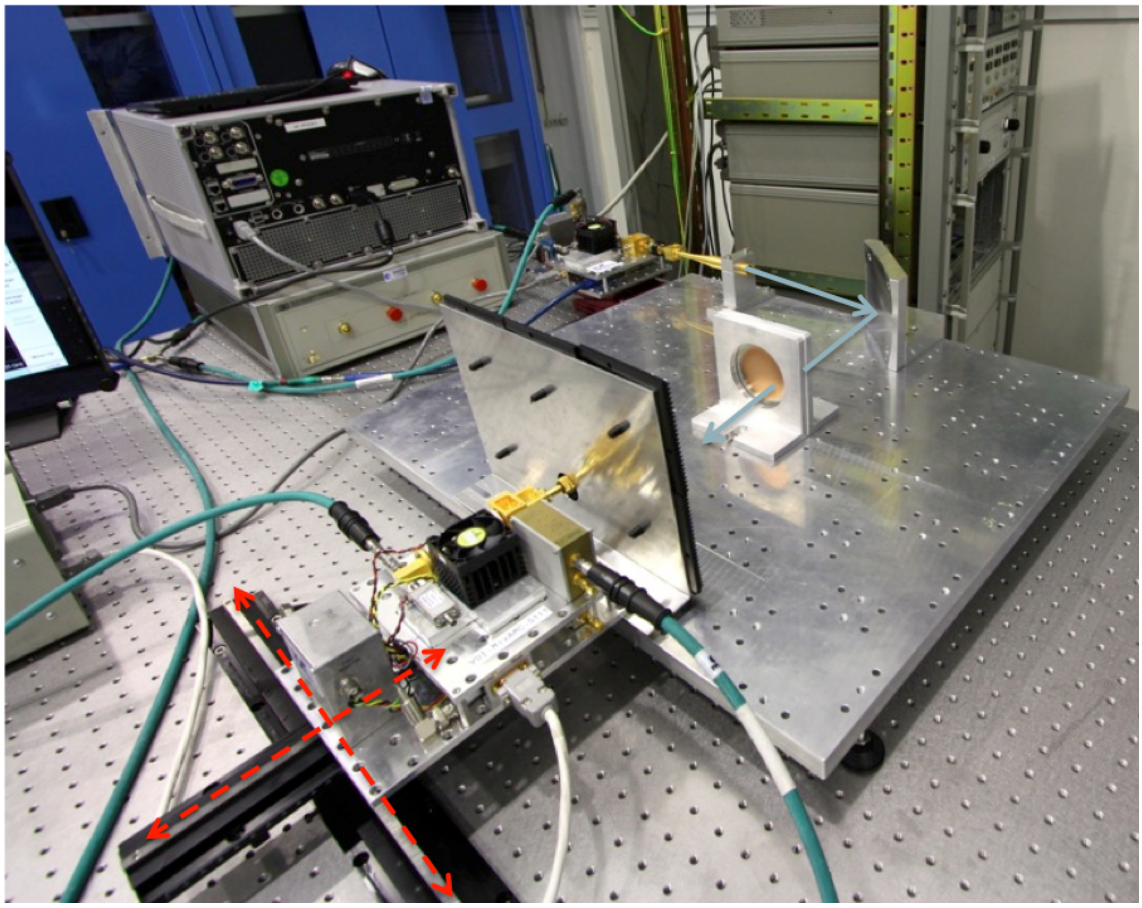

Figure 4.5: Modified quasi-optical bench to measure field distribution. Receiver is mounted on movable x-y stage

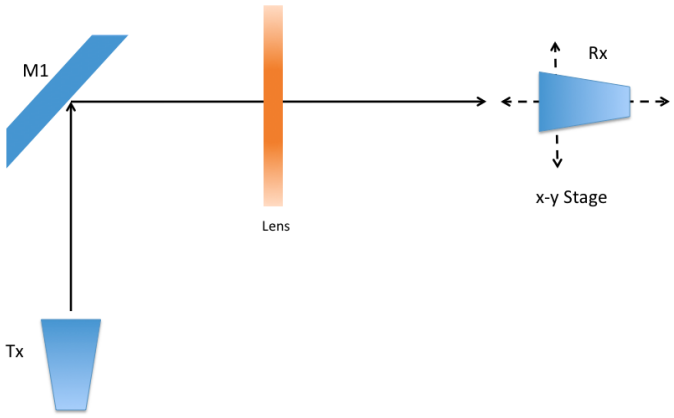

Figure 4.6: Schematic of modified Quasi-optical test bench

on the number of measurements that can be made. So it was decided to have a higher resolution in the plane parallel to the lens in order to have a clearer understanding of the beam shape could be formed.

Since the lens is radially symmetric, only a 2d cut of the 3d field needs to be scanned as long as the horn is well aligned through the centre of the lens. Due to using a x-y scanner that works in the horizontal plane, it is important to make sure the height of the receiver horn is inline with the centre of the lens. This was achieved by mounting the x-y stage on an adjustable stage in the third axis(z). The other important step to consider when aligning the setup, is to make sure that the horn is scanned perpendicular to the face of the lens. Since one of the main requirements of these measurements is to obtain the phase, any misalignment would introduce a slope into the phase results. To accurately align the receiver, the lens was removed and the phase was measured at two different points across the sample holder. If perfectly perpendicular the phase would be the same at both points. If not the alignment can be adjusted and the measurements repeated.

The lens was initially designed to operate at 150GHz. However, the underlying physics of the equivalent index metal-mesh technology is not a strong function of frequency so it is expected that this lens would be effective at other frequencies below the natural cut-off the the capacitive grids. How much its behaviour would differ from the frequency of design is on the other hand not well known and measurements would both confirm and guide further modelling of this aspect. Based on the above, the three frequency bands 75-110 GHz, 110-170 GHz and 170-260 GHz bands were used.

4.2.3 Measurement Errors

When setting up to take a measurement, it is important to consider and possible errors and systematics that could effect the data. The biggest source of error comes from the the ability to correct setup up the position of all the components, which will also effect the repeatability of the measurements, since every time the experiment is re-assembled, the precise positioning of components can change. In practice this is not an issue since all the components were place on a optical bench and the translational stages had a fixed reference that they could be aligned to. However, to be completely sure, once a given measurement setup had been configured, it was left unmoved until all frequency bands had been covered. The only distance that had to be measured was the distance of the phase centre of the horn to the lens. This could be accurately measured to the nearest millimetre.

The electronics used were very stable. The VNA could measure values down to .01 db. Which is far greater accuracy then required, since the purpose of these tests was to

confirm the general behaviour of the lens. If this device had been designed for a specific application, much greeter care could be taken in obtaining a more accurate result. The data taken here is to look at the shape of the data, rather then specific values a full calibration of VNA was not needed.

4.3 Results

Using the setup described above, the field behind the lens was scanned from left to right in 1mm steps, then repeated again after increasing the distance from the lens. Due to limitations in the range of the movable stage, the closest distance to the lens that could be measured was 50mm, with the main interest in the lens performance being the area around the focal length.

The distribution of the field is measured at different increasing frequencies is shown in Figures 4.7 - 4.11. These 2d contour plots show the focusing power of the lens, which is situated to the left of the plots. It can be seen that there is a slight shift with the focal length as the frequency increases. This is due to the change in the effective refractive index with frequency of the artificial dielectric structure. The other notable change is that the focal length appears to be around 23cm shorter than the designed focal length of the lens.

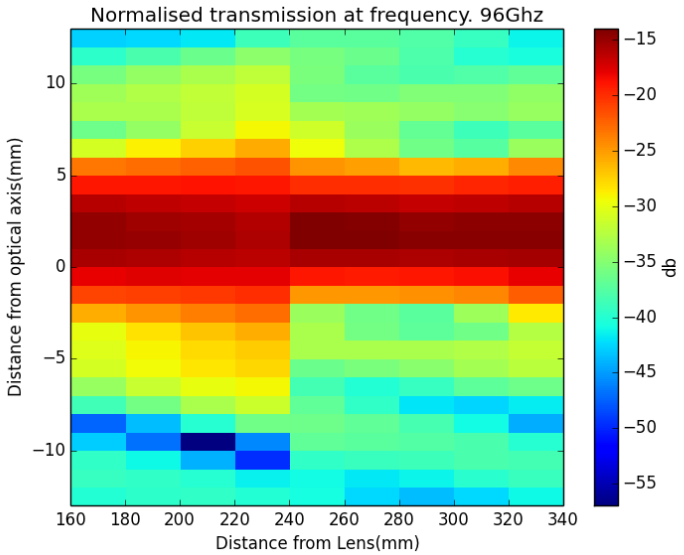

Figure 4.7: 2D plot of the transmitted field at 96 GHz. The lens was situated to the left of the plot.

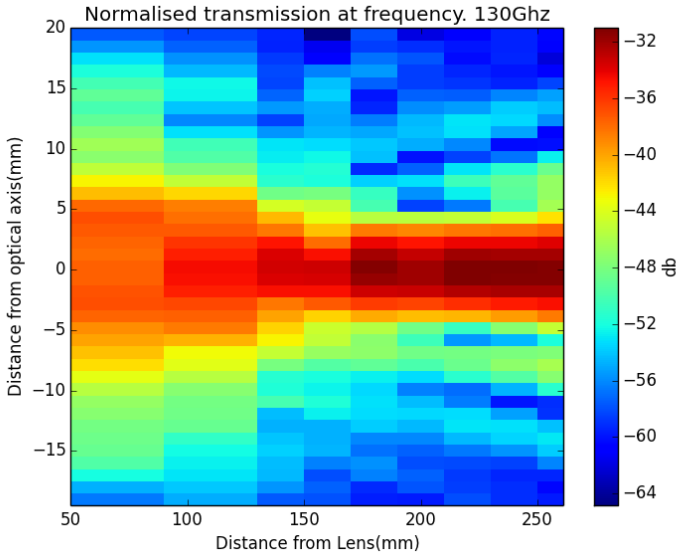

Figure 4.8: 2D plot of the transmitted field at 130 GHz. The lens was situated to the left of the plot. The focus can be seen to be at 230mm.

This is due to a slight change in effective refractive index from ideal design. Since it has been shown in chapter 3 that the mis-alignment of the grids does not change the effective index, it must be due to the dispersion that occurs in the grids. This would cause a increase in refractive index at the centre of the lens, since the dispersion effect is greater for larger patch sizes. An increase in refractive index corresponds to a decrease in focal length.

Figure 4.12 shows the cross sections of the lens transmission at 150GHz, it shows how the beam waist narrows around the focus of the lens. The displayed beam pattern is slightly broader then it actually should be. This due to to the fact that the beam is convolved with the aperture of the receiver horn. When characterising future devices which are designed for a specific application, this must be taken into account. However, since this was to demonstrate that the prototype would work, it does not need to be considered. Figure 4.13 shows how the variation in phase changes with position at 150GHz around the optical axis of the lens. These phase results show that the focus appears to be at 230mm where the phase is the flattest, which matches the previous result.

After characterising the performance of the lens with normal incidence, it is now possible to explore the performance off axis. This is of interest since there are two possible factors that could affect the lens. The first is the consideration of optical effects that occur with an ideal Wood lens, such as aberrations [38]. There are also certain effects that oc-

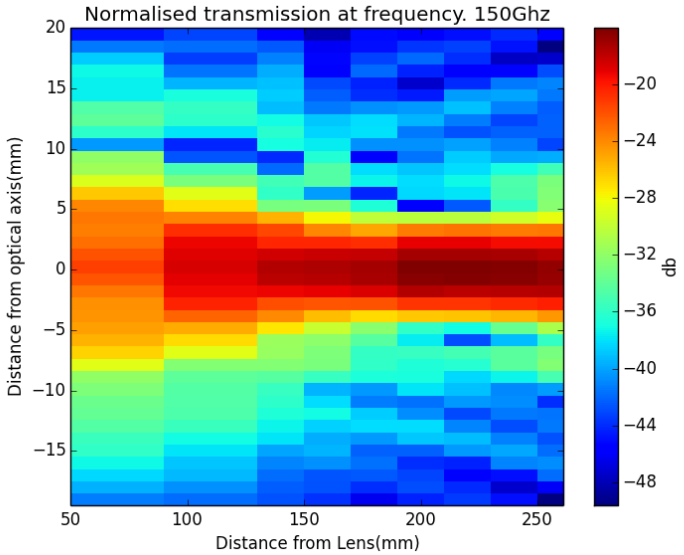

Figure 4.9: 2D plot of the transmitted field at 150 GHz. The lens was situated to the left of the plot.

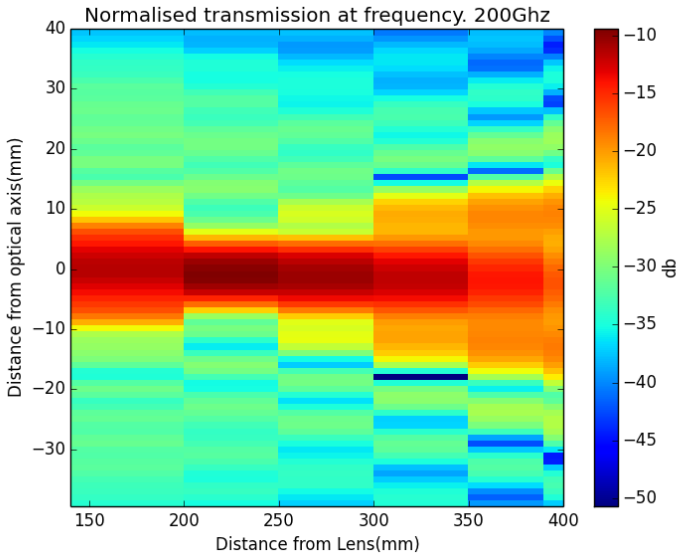

Figure 4.10: 2D plot of the transmitted field at 200 GHz. The lens was situated to the left of the plot.

cur with metal mesh grids when there is non-incident propagation. These include Woods anomalies which are spurious transmission peaks that occur off-axis and the introduction of polarisation effects [39].

The latter effects can be taken into account by using the band structure model described in Chapter 3, to model how the refractive index changes, based on physical dimen-

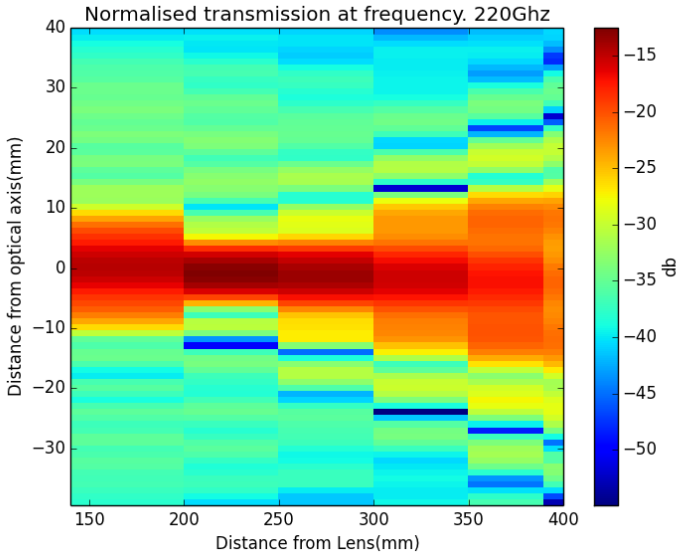

Figure 4.11: 2D plot of the transmitted field at 200 GHz. The lens was situated to the left of the plot.

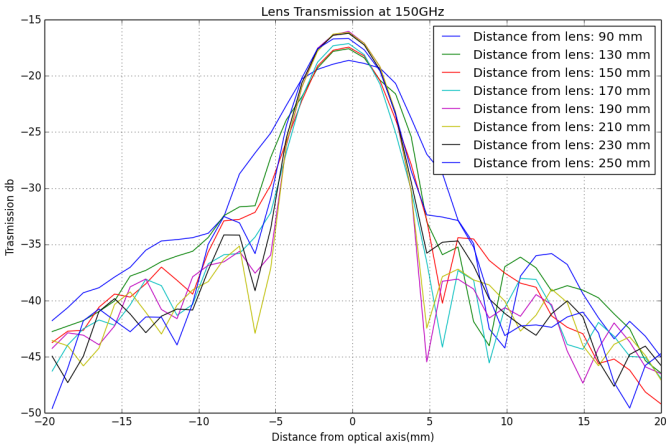

Figure 4.12: Cross sectional cut of beam pattern at 150GHz. It shows have the beam waist narrows around the focus of the lens.

sions of the patch sizes that were used. The results of this comparison are shown in figures 4.14 and 4.15. The dark blue curve shows the ideal index distribution obtained from Woods formula 5.1, based on central index of $n = 2.65$. The green curve is based on the the analytic expression of $n(a/g)$ used to design the lens [33], which closely approximates the ideal case. The red curve is obtained when the actual a/g distribution used, is placed into the band structure model. This n takes into account the frequency dispersion of the effective index caused by the girds. It shows that there is a slight increase in refractive

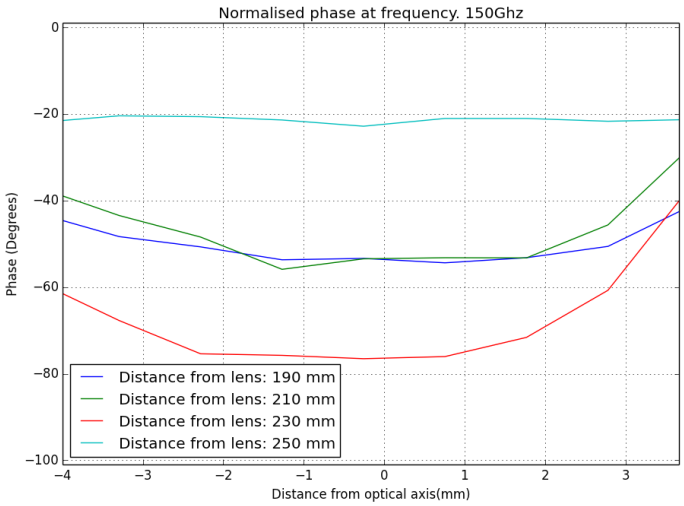

Figure 4.13: Change in phase front with distance from lens at 150GHz. At the focus of 230mm the phase becomes the flatest.

index, but this is inside of the original tolerances of the lens design. The most important curve is the light blue curve. This shows how the index distribution now changes at a non-normal incidence, which is that there is only a slight change. This is the ideal case, since it shows that lens should still perform off axis. For further clarification, figure 4.16 shows the full spectral response of the centre point of the lens. It shows when off axis, there is a small uniform shift downwards in the refractive index. These results show that it is expected that the off axis behaviour of the lens can be mostly predicted by ideal GRIN theory [40].

The same measurements are repeated but with the lens rotated about its axis to 12 degrees, to simulate non-normal incidence. Since the focused beam will also be at an angle, the x-y stage, thus the receiver, is tilted by the same amount so it is still perpendicular to the lens. This is represented in figure 4.17 The results from this measurement are shown in figure 4.18. Assuming that the underlying mesh structure behaves as in figure 4.14, this off axis behaviour has been modelled using the commercial ray tracing software Zemax, as shown in figure 4.18.

The final measurement performed on the lens, is a beam pattern measurement. This is achieved by fixing the receiver at the focal length of the lens then changing the angle of incidence of the plane wave on the lens. The measurement is made by attaching the lens and receiver to a rigid bar and allowing it to pivot about the centre of the lens. To make

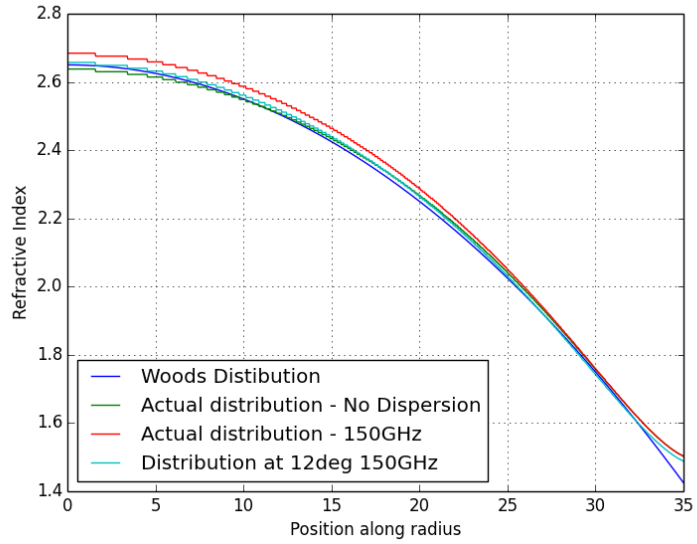

Figure 4.14: A comparison of the ideal design refractive index profile against dispersion model.

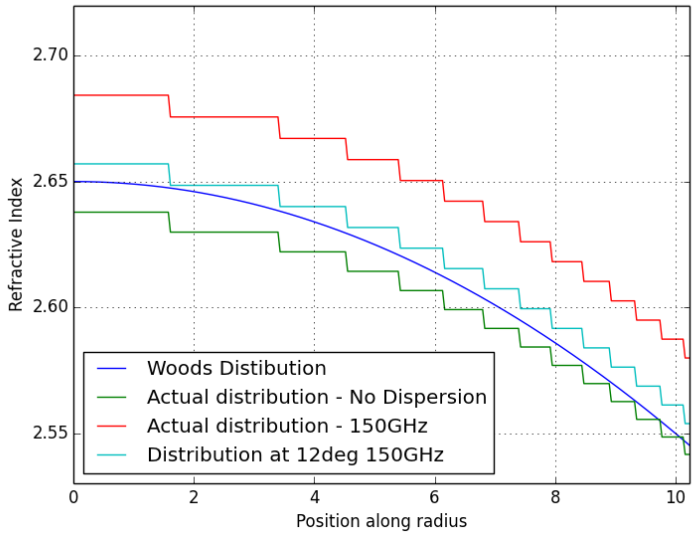

Figure 4.15: Variations in refractive index in the central region of the lens.

measurements of the angle, a mirror cube was placed on top of the lens and a laser was reflected off it onto a flat surface. Using simple trigonometry, it was possible to measure the defected distance of the laser from the origin to recover the angle. This setup is shown in Figure 4.19.

The results of this measurement are shown in Figure 4.20. The results are normalised

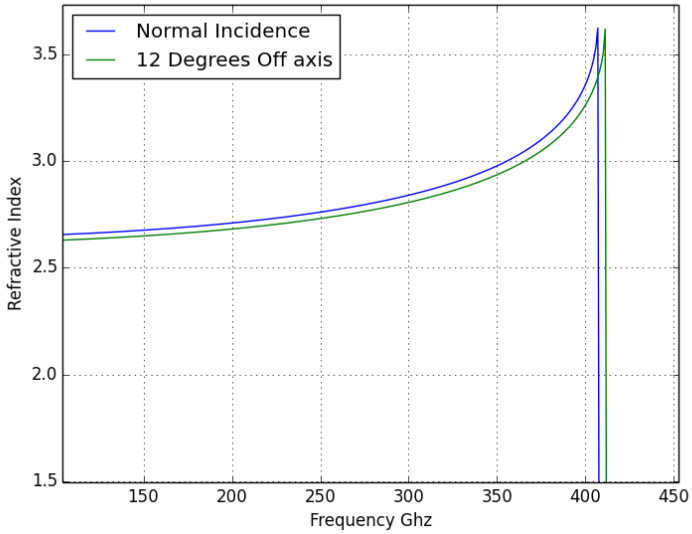

Figure 4.16: Change in central refractive index at centre point of lens with angle.

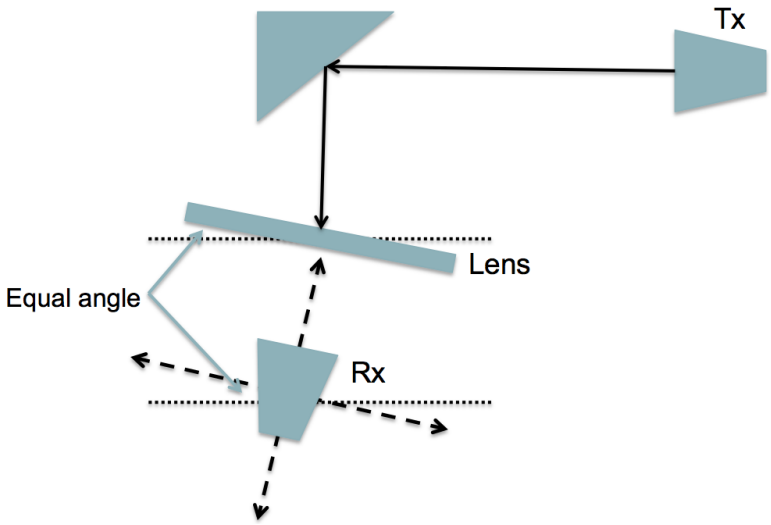

Figure 4.17: Diagram of quasi optical bench modified for off axis measurement.

to show how the beam pattern changes with frequency. This shows that the first side lobe occurs at -13db.

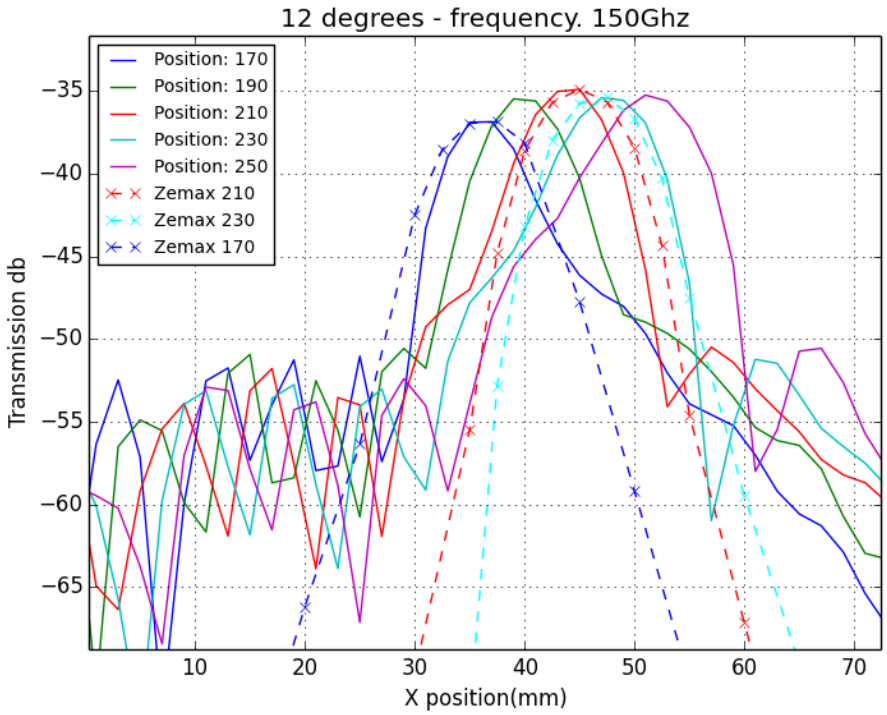

Figure 4.18: Transmission of non-normal incidence through the lens at 12 degrees, overplot of Zemax simulation of the same setup.

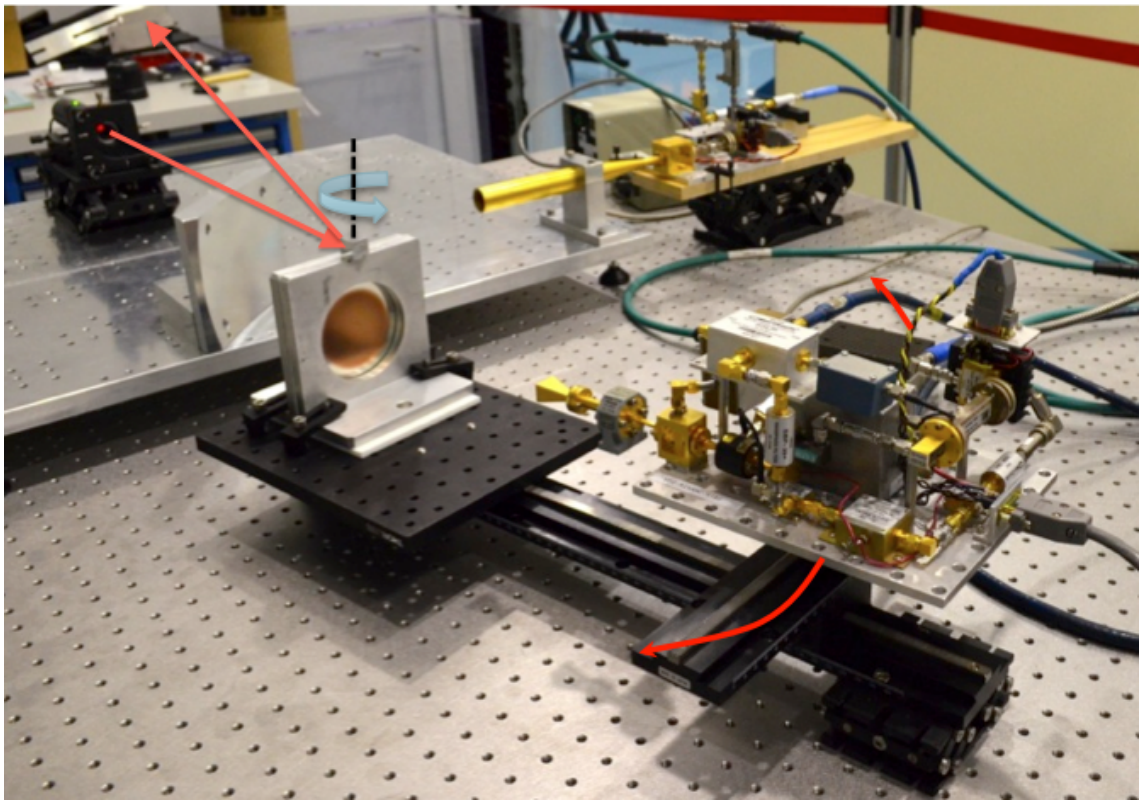

Figure 4.19: Modified quasi-optical bench to measure beam pattern. Receiver and lens are in a fixed position relative to each other.

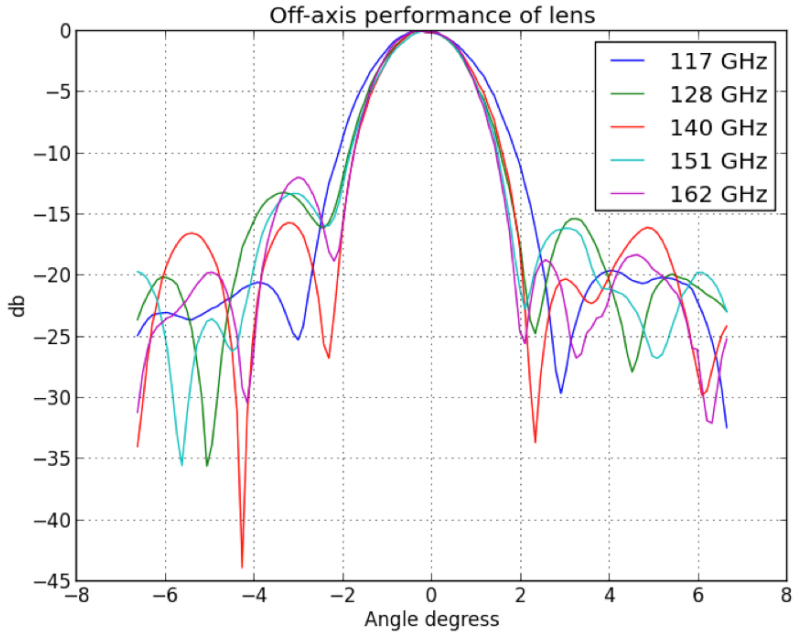

Figure 4.20: Measured beam pattern of lens, measured in db.

4.4 Further Developments

4.4.1 Anti-reflection coating

One of the biggest restraints on this current lens design is the reflection losses due to the impedance miss-match of the lens. Which is greater then the absorption losses in the lens. The way to avoid this, is to use an anti-reflection coating (ARC) layer designed with the same gradient index material as the grin lens. In a standard, non-grin lens, the simplest ARC is designed by placing a matching layer on both sides of the lens, with an index of $\sqrt{n_1 n_2}$ where n_1, n_2 are the refractive indexes either side of the coating . The thickness of the layer is is given by $\lambda/n4$ where λ is the optimum wavelength where maximum transmission will occur and n is the index of the coating.

To modify this for a grin lens, the matching layer must also have a graded index, that matches with the lens underneath. A proposed solution is to use three grids with a 100 micron spacing between to give a total thickness of 300 microns. This places the optimal operating frequency at 240GHz. When added to the the overall transmission simulation of the lens, there is a vast improvement in transmission, as shown by the green curve in figure 4.21, which also shows the comparison to the un-coated lens.

The limitation in this method is that the improved transmission performance is only over a narrow band. In normal optical systems, this is compensated by using additional matching layers of different index and thickness. However, it was found that having one metal mesh layer and another layer of normal dielectric, there could still be an improvement to the bandwidth. When simulated, this improved the transmission as shown by the blue curve in Figure 4.21.

4.4.2 Quater pitch lens

An evolution of the Wood lens design is to create a graded index lens which has the focus at the rear surface from the incident one. An illustration of this is given in figure 4.22. The application for such a device would be to replace existing hemispherical lenses used in detector arrays such as Polarbear [41]. Currently, hemispherical lenses are used to couple radiation to each detector in an array, and are typically made out of silicon in order to match the impedance of the detector substrate (also silicon). [42].

Array sizes are continuously increasing meaning that the number of lenslet couplers is also increasing. Given that each individual lens has be machined and polished as well as

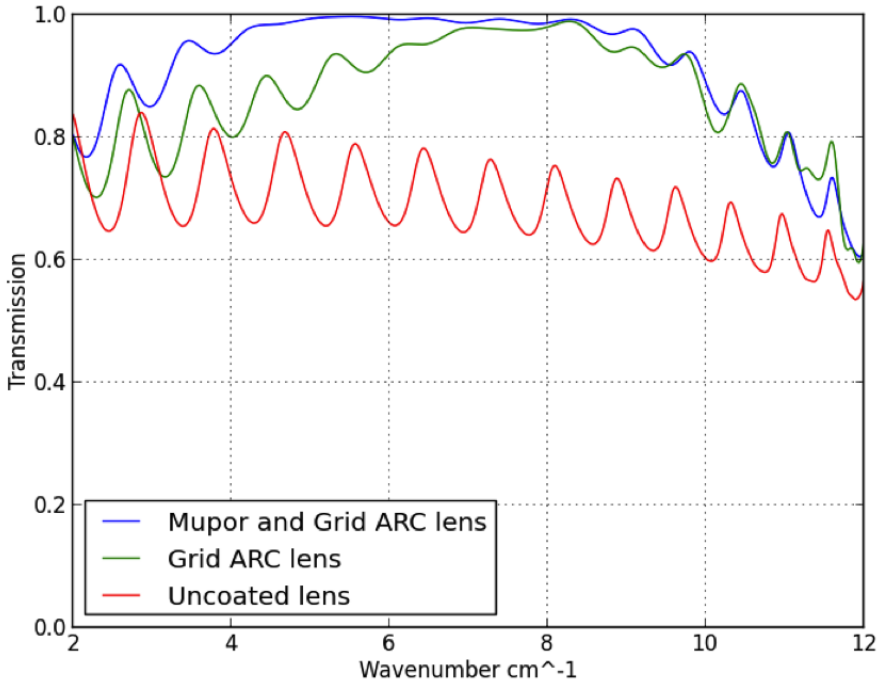

Figure 4.21: Comparison of how transmission changes by adding an ARC. The red line is the uncoated lens. The green shows just a simple ARC layer and the blue shows how the extra layers increase the overall bandwidth.

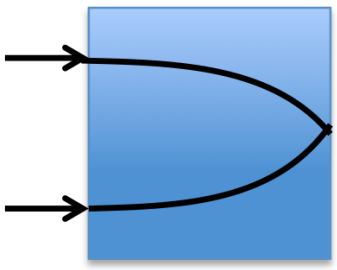

Figure 4.22: Quater pitch lens.

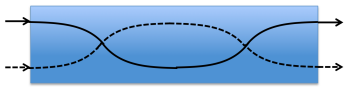

Figure 4.23: Full pitch rod. Typically used in fiber optics.

AR coated, the cost in time and money to build up larger arrays becomes impractical. The increase in array size leads to a greater possibility of variation between different lenslets that could produce systematic errors between detectors. The proposed quarter pitch lens could avoid these issues, since one large metamaterial slab could be fabricated which would contain multiple lenslets due to the ease of placing copies of the gradient pattern on the same photolithographic master. This would allow for more precise placement of the lens onto the detector as well as allowing for greater uniform behaviour between each lenslet.

The design of a quarter pitch lens is not new, they are currently used in conjunction with optical fibres and are usually described as "SELFOC lens" as in self focusing lens. Just like the Wood lens, the quarter pitch lens had a radial varying refractive index and is given by equation 4.2 where r is the lens radius and g_0 is the gradient constant that relates the radius of the lens to the pitch of the lens. A lens of pitch 1 is shown in figure 4.23, it is a rod of a given length, such that a ray incident at r_0 completes one complete oscillation in the lens before leaving at the same point on the opposite face. The rays in this gradient can be described by equation 4.3, so a lens of pitch 1 means $g_0 z = 2\pi$. Therefore for a quarter pitch lens is described $g_0 z = \pi/2$, so that all rays leave the lens at the same point. This relationship means that the thickness of the lens can be chosen freely to determine g_0. Once that is determined, the radius of the lens can be found from equation 4.2, for a chosen n_{max} and n_{min}

$$n^2 = n_0^2(1 - g_0^2 r^2) \tag{4.2}$$

$$r(z) = r_0 cos(g_0 z) \tag{4.3}$$

The size of the existing hemispherical lenses are $10mm$ in diameter, so a quarter pitch lens should aim to match it. To achieve this diameter, a thickness of 10mm is required, with a central index of $n = 2.3$, which gives a radius of 4.85mm. However, there are some

limitations in realising this design in practice.

Firstly, how smoothly the index can be varied, since there is now a much smaller radius to cover for almost the same index range as the previous GRIN lens. In this proposed design, $g = 200um$, which allows for 20 cells across the lens. The biggest limitation is the number of layers that are required to build up a device with this thickness. The largest spacing value that was capable of obtaining the central index value and maintaing the cell size, is 200um. This gives the required number of layers to be 50 which is not currently practical using existing manufacturing techniques.

The largest number of layers hot pressed is currently 20, which was the case of the 2mm thick GRIN lens. There is also a issue with thermal heating, since polypropylene has a higher heat capacity than silicon, and could cause a build up of heat which could cause additional thermal loading on the detectors that are cooled to sub-Kelivn temperatures.

A possible solution to this is to relax the focusing criteria of the lens such that it focuses a few millimetres away from the actual lens surface. This would allow for the a reduction in the thickness, so a reduction of layers. Further work is needed to study if this provides a more practical solution as well as investigating if there is any change in the coupling efficiency between lens and detector.

4.5 Conclusion

It has been shown that a gradient index flat lens can be built using an artificial dielectric[43][44][45][46]. By building a suitable test setup, including a network analyser, additional measurements were taken to further understand the performance of the lens. The lens was shown to match the ideal lens design closely, with only some chromatic behaviour due to the dispersive nature of the structure. New measurements of the off-axes behaviour of the lens were made. These results matched simulations of an ideal flat lens, which was able to show that even off axis, the mesh structure behaves as an artificial dielectric.

Since the lens was not impedance matched to free space, there were losses in the performance due to reflections. It was shown that by adding a graded index anti-refelction coating, the performance could be improved. Finally it was shown how the index profile of lens could be modified so that a quarter pitch lens could be made. While it was theoretically possible to make the required index profile, the large number of layers meant that it is currently not practical to build such a device.

Chapter 5

Polarisation Splitting Lens

5.1 Proposed design

Given the successful demonstration of a GRIN lens built using metal mesh grids, an investigation can be made to look into possible new optical device concepts. Choosing the next novel device to build is based on a balance between theoretically interesting optical designs and producing a device which has real practical applications.

Due to the potential complexity of manufacturing these designs, the choice of prototype to be realised must be a careful one. This is because the facilities used to fabricate these devices operate continuously at high capacity producing optical elements for other cutting edge research experiments, as well as commercial activities. This means that devices such as the quater-pitch described in chapter 4 would take a much longer time to be built as it will have to fit in with the clean room schedule of the Astronomy Instrumentation Group in Cardiff where these devices were ultimately built.

Given these criteria, it was decided to pursue a novel lens design that is capable of independently controlling two linear polarisation components such that they are spatially separated out and focused on the same focal plane. This is a device that can not be currently realised using traditional crystal optics.

The advantage of such a device is that if a single cell of the equivalent material presents different impedance values for opposite polarizations, it must be possible to create a material which is locally birefringent with distributions which are locally smooth independent

functions. Currently, to separate the polarisation of the input beam, beam splitters or polarisers must be used, which open additional ports in a system while augmenting the overall volume of the detecting system. This novel device could at the very least allow a more stringent definition of the instrument input while allowing a compact detecting unit.

The most similar existing optical device which represents the proposed design is a Wollaston Prism. This is a simple optical device consisting of two prisms made out of a birefringent crystal. They are then combined together such that the the crystal structure, thus birefringence, is rotated 90 degrees to each other as shown in figure 5.1. This device takes any unpolarised or partly polarised light source and deflects the two linear polarisations such that they are diverging from each other. However, this device is not capable of focusing the separated beams, to do this additional optics are required.

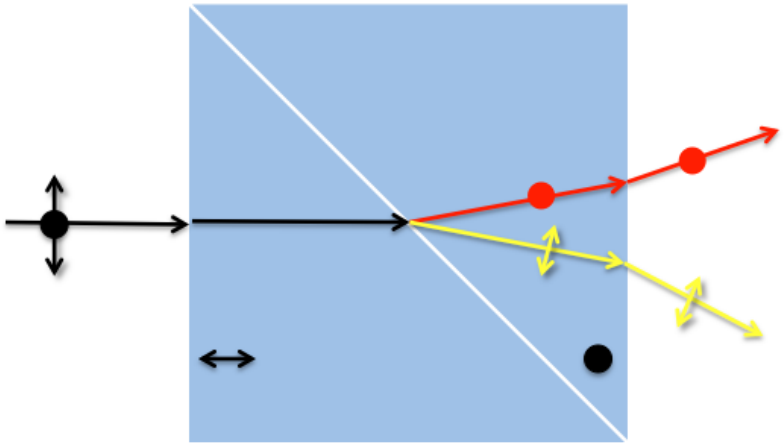

Figure 5.1: Ray path through Wollaston prism. Two birefringent prisms are orientated such the crystal axis are perpendicular.

This proposed device is based on the idea that it is possible to have local control of the birefringence of the material, so that each polarised wave takes an independent path through the lens. From this principle, the physical lens can be designed by containing two virtual lenses overlaid on top of each other, with a separation between the two lenses. Since each virtual lens is only sensitive to one polarisation, the corresponding separation relates to a separation in foci on the focal plane.

5.1.1 Ideal Lens Recipe

To constrain the number of unknowns in the design of this new device, the same recipe from the previous GRIN lens will be used for each of the virtual lens designs. In theory

almost any isotropic radially varying lens recipe could be used for the two virtual lenses. However, by using the existing design for the single lens built, a direct comparison can be made to see how the lens performance changes, since ideally the performance should be the same for each polarisation.

Therefore, the index profile used for each virtual lens is given by equation 5.1, which is the same Woods formulation used previously. With the same focal length of 250mm, a thickness of 2mm and radius of 35mm to match the existing lens.

$$n = n_0 - \frac{r^2}{2df} \tag{5.1}$$

The overall index distribution of the lens can be made by creating a common reference frame. For each point in this reference frame a vector n can be defined, which can take two values, n_{co} and n_{corss} corresponding to the refractive index each polarisation is senstive at that point.

Since each lens has a radially varying index, there are lines of constant index which form circles around the centre of the lens as shown in figure 5.2a. When the two lenses are overlapped with a chosen horizontal offset of their relative centres, shown in figure 5.2b, the circle of constant index for one lens now intersects the constant index circles of the other lens. The difference in anisotropy of the material at each point on the physical lens is determined by the chosen separation of the two virtual lenses.

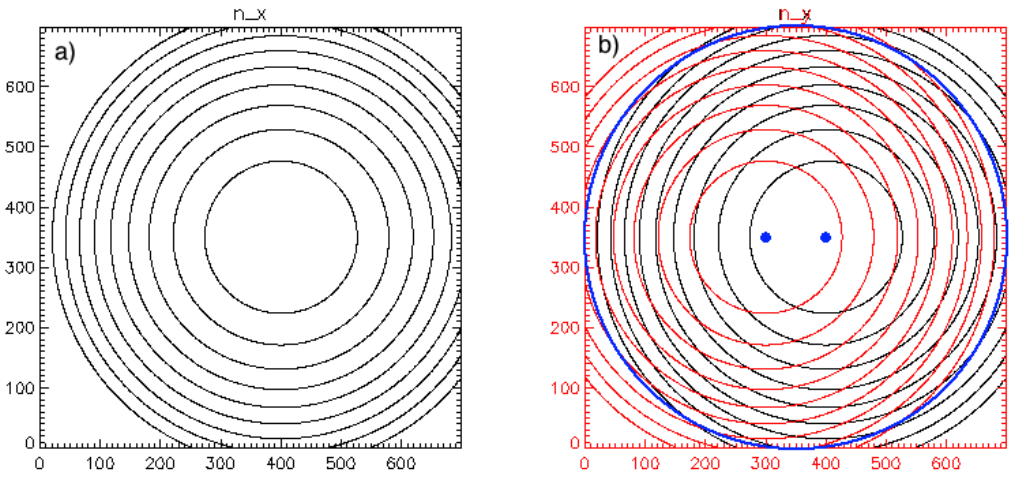

Figure 5.2: a) Radial distribution of index for one lens. b) Combined index distribution for both lenses. Physical device boundary high lighted in blue.

5.1.2 Material Design

To realise this design in practice, the artificial birefringence described in chapter 3 must be used. This allows for control of the two linear polarisation states. A parameter space of possible values must first be performed to find the range of available refractive index profiles as well as the maximum birefringence obtainable.

It is not needed to explore all 5 possible parameters, since most of them are constrained by the physical requirements imposed on the lens. Since this is the same physical design as the previous lens, the same material parameters can be used setting the requirement for 20 layers with a separation between them to be $100um$. This also yields the required 2mm thickness. The unit cell size is chosen to be 200um square, which allows for the lens to maintain the same index resolution as previous used and maintains a regular periodicity across the whole lens. With these parameters constrained, only the size of the rectangular patch can be varied to control the effective refractive index across the entire lens. These parameters are defined as the ratios a/g_x and a/g_y.

A preliminary parameter space map can be produced using the transmission line model. While it has been shown in Chapter 3 that there is a disagreement for some geometries, the speed of the simulations means that it can be used to give an approximate parameter space to test if the lens design is possible. The results from this produce Figure 5.3. This surface shows the values of n_y that can be achieved for a given a/g_x and a/g_y. The corresponding plot for n_x is the same but has its axis swapped. The surface in figure 5.3 shows that for a given refractive index, there are different combinations of a/g_x and a/g_y that exist. In the reference frame of the other polarisation, the surface is flipped, this means that the same a/g_x and a/g_y values correspond to a range of indexes. This anti-symmetric design means that such a lens design is possible providing that the Δn between the two indices defined by the pairs (a/g_x,a/g_y) identified when cutting the surface with a plane of constant value on its symmetric surface.

With confidence that the range of possible simultaneous index values can be achieved, the parameter space values can be obtained from HFSS. The results from this for each polarisation are shown in figures 5.4 and 5.5, the orginal data points have been interpolated, since a high resolution simulation is not feasible due to time constraints. While the TL does not match outside the regions when the rectangles approach a dipole, the same anti-symmetric profile is present which proves the assumption was correct.

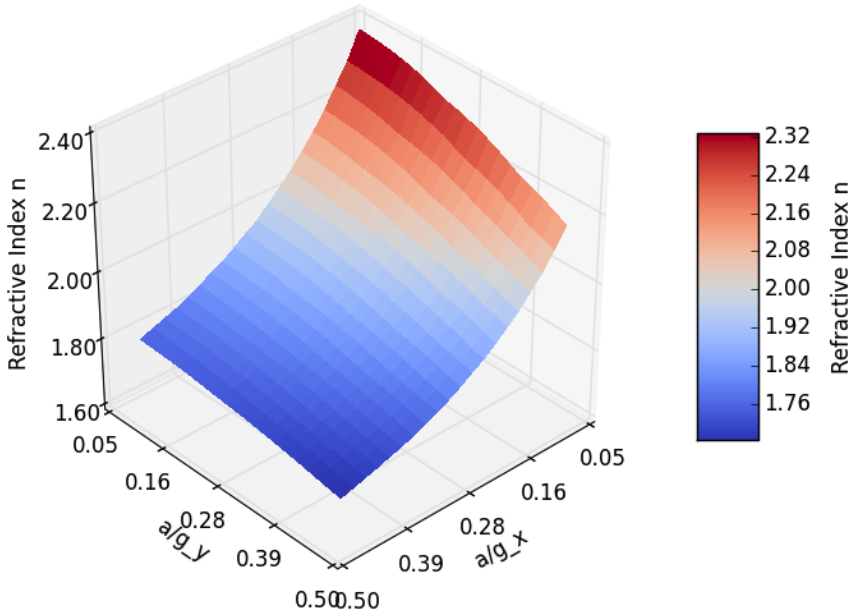

Figure 5.3: Refractive index parameter space for a/g_x vs a/g_y as seen by a co polarised wave

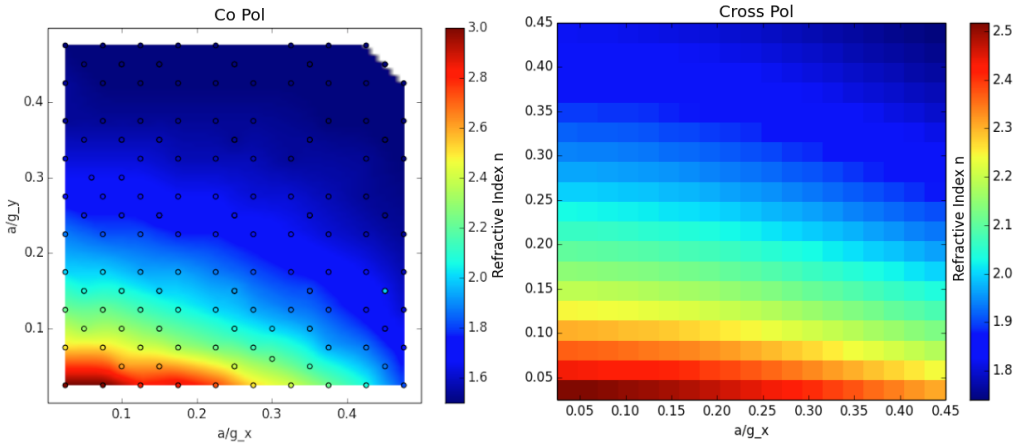

Figure 5.4: Effective refractive index parameter space, for a co-polarised wave. HFSS simulated mesh patterns are interpolated in the contour plot on the left, TL model is on the right for comparison.

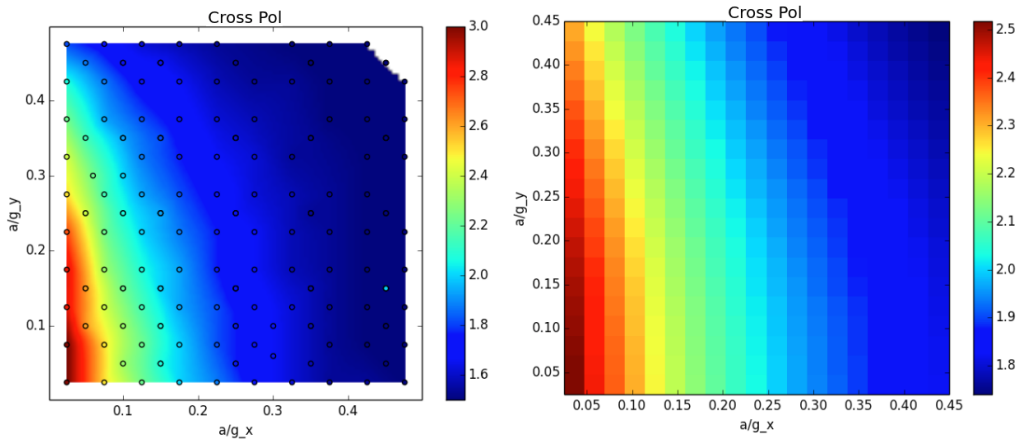

Figure 5.5: Effective refractive index parameter space, for a cross-polarised wave. HFSS simulated mesh patterns are interpolated in the contour plot on the left, TL model is on the right for comparison.

With a suitable parameter space now found, it is possible to match up the physical geometries to the ideal lens design. Since the physical ideal lens design consists of a vector of n_{co} and n_{cross}, an iterative process must occur to find all the suitable values for the lens map. This is complicated by the fact that a given value of n_{co} or n_{cross} depends on both a/g_x and a/g_y. The selection process is best illustrated by figure 5.6. A value of n_{co} or n_{cross} is first selected, the order does not matter since the physical parameters are reciprocal. The value will have a contour line in the parameter space which corresponds to an array of patch geometries, which will produce that given refractive index. Taking this array of values, they can be plotted on top of the parameter space of the other polarised index value as shown in figure 5.6. This line now intersects a range of refractive index values which are able to be selected. It is from this list that the second point in the index vector can be chosen. This then fixes the geometry of the patch. The secondary selection only contains a limited choice of available index values, figure 5.7, it is the maximum difference in index values which sets the maximum local birefringence that is obtainable at that point and thus the maximum separation between the two virtual lenses.

The results of this procedure when applied to the lens design produce the corresponding patch geometry's shown in figure 5.8. This comparison shows that it is technically possible to produce this lens. However, there is a limitation in this design. Any area where the effective index of one GRIN lens falls below that of the substrate will not allow for any GRIN behaviour of the other lens, thus breaking the overall cylindrical symmetry of the device. This design is then fabricated using the same method for the previous lens. Only

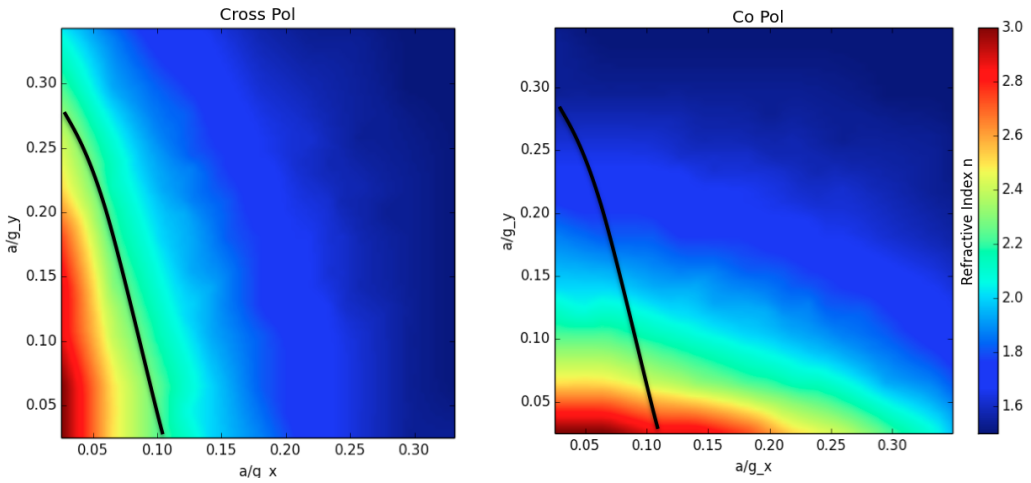

Figure 5.6: Illustration of how one an array of patch sizes can selected so that they follow a line of constant index for one polarisation, while those geometries relate to a selection of values for the other polarisation.

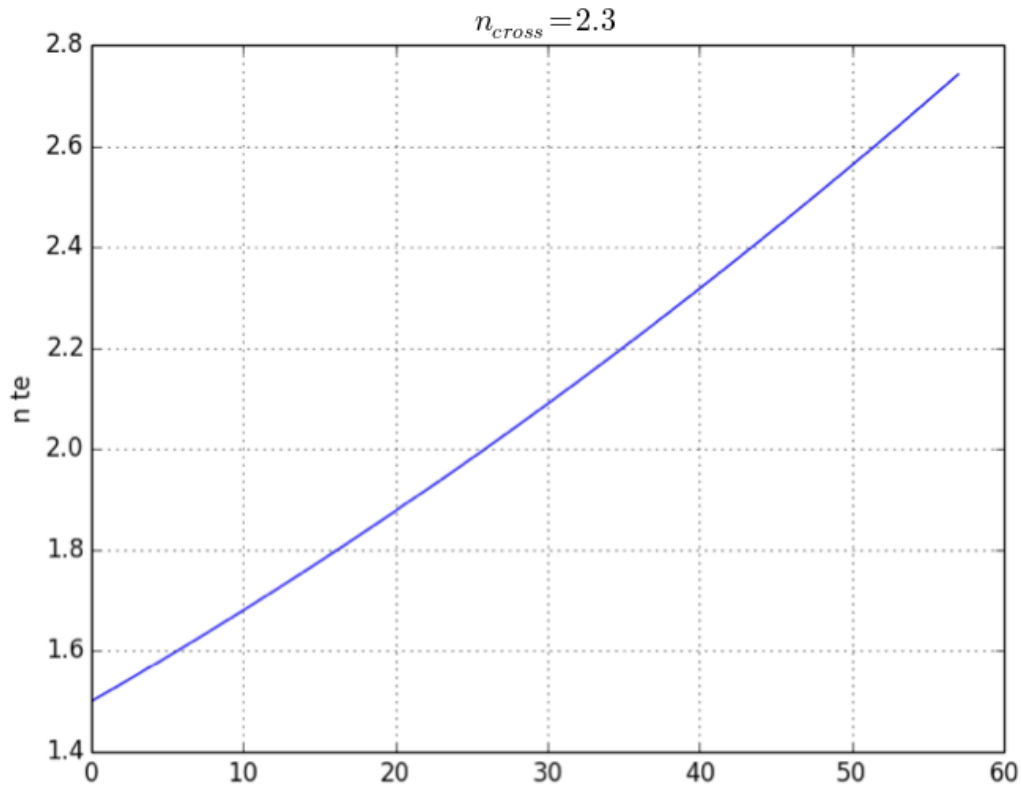

Figure 5.7: This shows the range of index values which can be obtained for one polarisation, while maintaing a constant refractive index for the other.

a single mask is required due to the fact that all the mesh layers are identical. The layers are then hot pressed together using polypropylene spacers.

Like the previous design, the lens has not been impedance matched to free space, meaning that there will be reflection losses. This could be addressed by using a ARC on the surface of the lens. By proceeding in a similar fashion as what was discussed in the previous chapter for the simple GRIN lens. However, since the purpose of this prototype is to test the basic principles, the ARC will only add unnecessary complexity to the design.

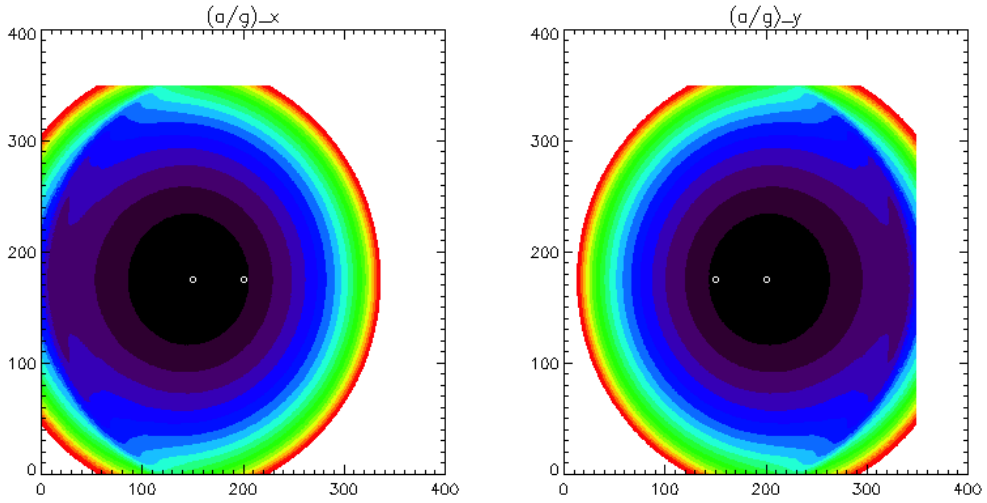

Figure 5.8: Contour plots showing the spatial variation in a/g for each axis.

5.2 Characterising the Lens

To successfully validate the design of this lens, there are a number of criteria that must be observed. The primary goal is to observe a shift in focus when changing between different linear polarisations. Also, the overall spectral properties of the lens should be measured to see how it compares against existing lenses functionality. Further testing will be required when the design of the lens splitter will be tuned for a particular application, in which case the knowledge of its detailed performance including second order aberrations will impact the performance of the instrument in question. Additional properties of the lens such as off-axis performance and characterisation of aberrations will also need to be studied. However, theses measurements are not required to validate the lens. A first set of tests was performed to check the spectral efficiency of the lens and due to the flexibility of the measurement setup, this was also setup with an additional translation stage allowing for

simultaneous scans of the detector system to check for the intended displacement of the focus.

5.2.1 Test setup

The experimental setup is based on refocusing the output of the FTS back down into the detector. This is achieved by using a two lens system, with the first lens expanding the FTS output into a parallel beam, then a secondary lens to focus the beam into the detector. Measurements will be taken of the standard two lens system and then the secondary lens can be swapped for the pol splitting lens, figure 5.9. A ratio of these results can be taken to test how the pol splitting lens performs. Two test configurations are outlined below, the first is to move the lens in front of the detector and the second is to scan the detector.

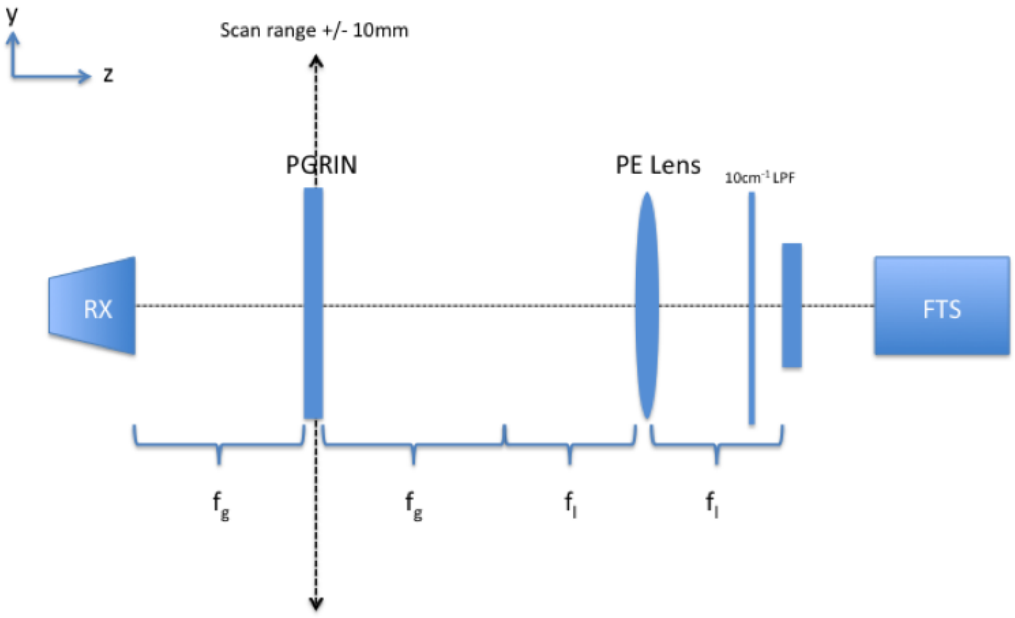

Figure 5.9: Optical configuration of the standard two lens FTS.

Lens scanning strategy

This test is setup such that the entire system is co-aligned with the lens translated perpendicularly across the beam. This exploits the fact that the optical axis for each polarisation is not in the physical centre of the lens, which is shown in Figure 5.11. This means that the lens will be in focus when the lens is offset so that a given optical axis is aligned with that of the detecting system, Figure 5.12. In this configuration the lens is under illuminated,

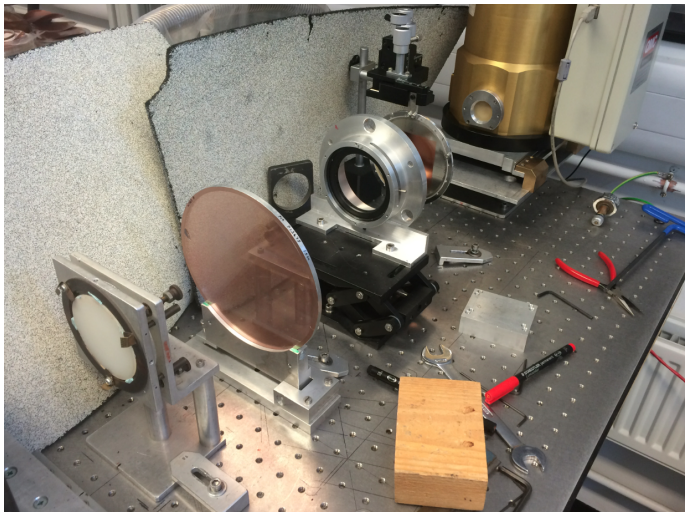

Figure 5.10: Actual FTS setup as illustrated in figure 5.9

which guarantees that when the lens is on axis, any detection will be due to the actual performance of the lens.

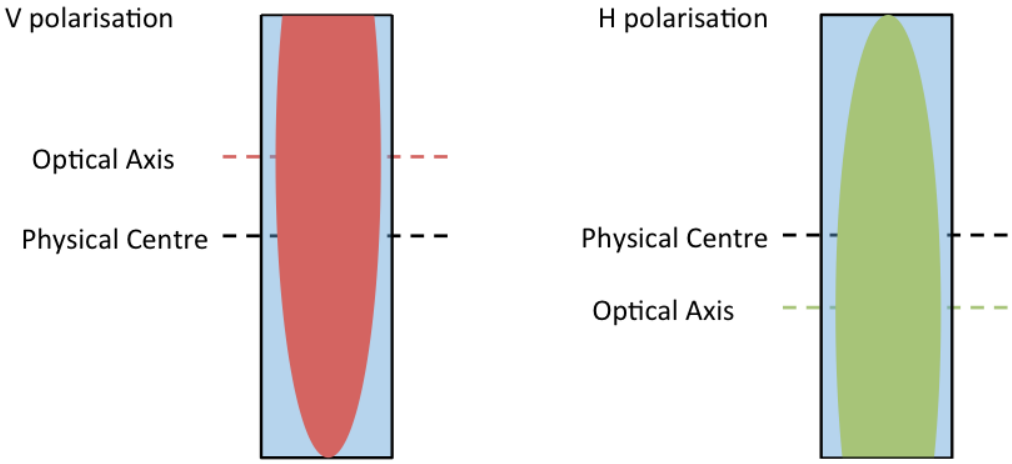

Figure 5.11: The two virtual lenses have different optical axis positioned in the lens.

In this setup the polarisation is set at the output of the FTS, with a 11cm^{-1} low pass filter included which limits the power to that of the frequencies of interest. A background reading is taken of the normal lens system. Once this is complete, the secondary lens can be replaced by the pol splitting lens. The positioning of the lens can then be adjusted to find the optimal focal length, height and minimise tilt. The expected focus for each polarisation is to be +/- 5mm at each side respectively from the physical centre of the lens. To cover this, scans were taken by moving the lens in 1mm steps +/- 10mm from its centre position. To allow for direct comparison, the second polarised state is measured

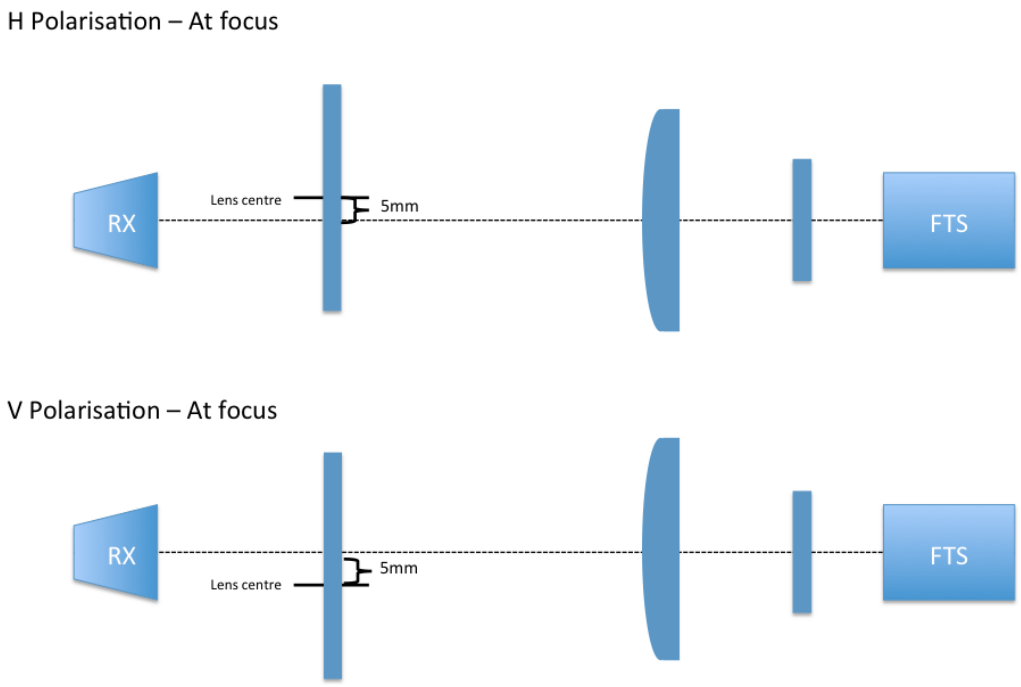

Figure 5.12: Position of the lens for each polarisation where the focus is expected to be.

without chaining anything else in the setup. Once this second set of data had been taken, the original lens is placed back and the background is retaken. This is required since the rotation of the polariser changes the output power of the FTS.

An additional test is performed on the lens by sending both polarisations simultaneously. This can be achieved by placing an additional polariser at 45 degrees in the optical path, Figure 5.13. Then the same procedure is repeated as before.

Detector scanning strategy

A different measurement approach is to keep the lens co-aligned with the FTS output while the detector is placed on a linear stage and scanned behind the lens. This has the advantage that the same amount of power is constantly incident on the lens, but involves mounting the cryostat containing the detector onto a linear state, which increases the complexity of the setup. The procedure for taking results is the same as the previous test. Another test that can be performed is to scan the standard polyethylene lens. This will allow for a comparison of the two different beam profiles.

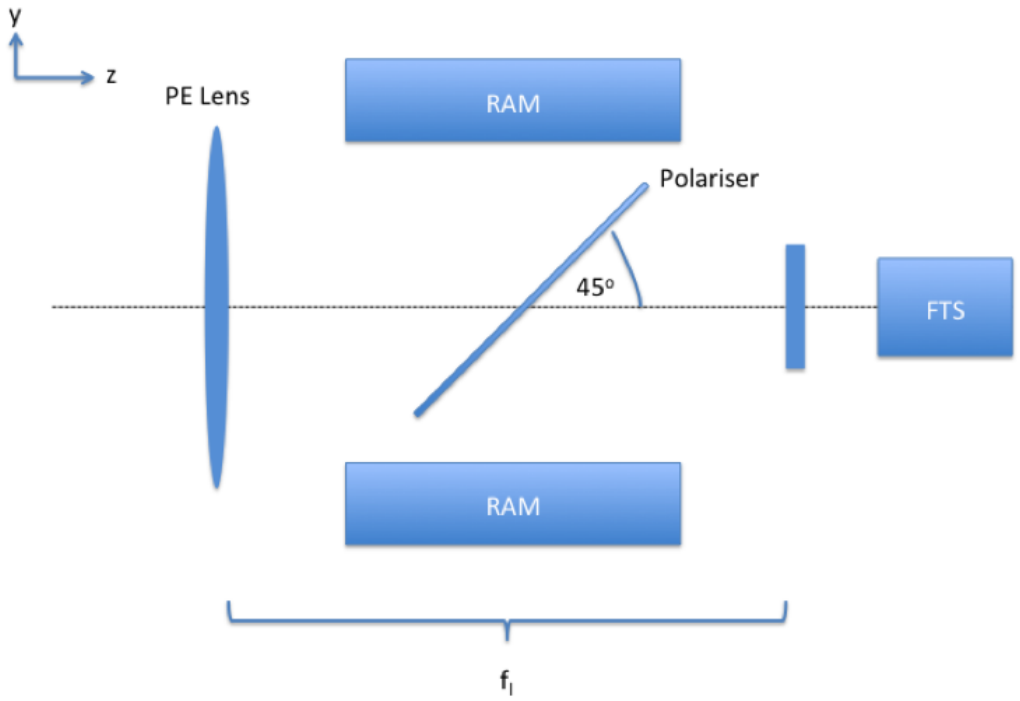

Figure 5.13: Polariser configuration for dual polarisation.

5.2.2 Results

The initial results from scanning the lens are shown in Figures 5.14, 5.15. These plots show the overall spectral performance of the lens as well as the focus position for each polarisation. The difference in powers between the two polarisations can be explained by looking at how the background measurements were taken. The data is normalised against the standard two lens system, so that the performance of the lens can be measured against the experimental setup. However, a problem arises in that it is assumed that the two lens setup is identical for each polarisation test. In practice swapping the lenses in and out means that there is some variation in the exact positing of the lens.This means that the alignment between the lenses is different for each background measurement, which causes a variation in the results between the two.

This can be corrected by looking at the original background plots and the ratio between them. Figure 5.16 shows that there is a slight difference between the two data sets, which is confirmed with the ratios given in Figure 5.17. The ratio at 5cm^{-}1 is taken to be 1.22, which can be used as a correction factor to give the adjusted beam profile in Figure 5.18.

The same correction can be applied to the spectral plot, Figure5.19 , which shows the same spectral performance for each polarisation.

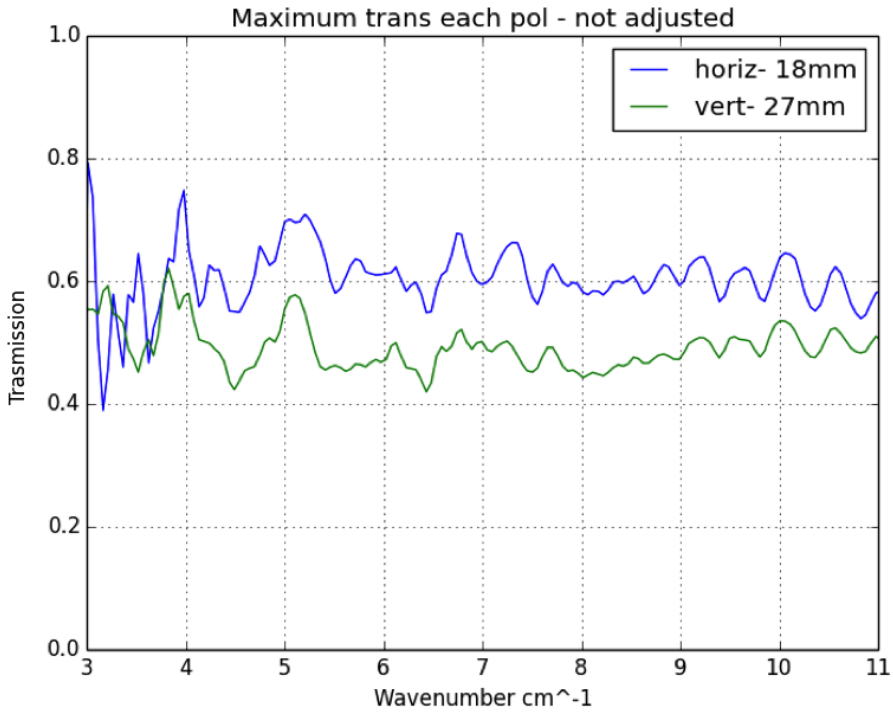

Figure 5.14: Spectral transmission of lens at each focus point

The additional features around the focus of the horizontal curve (15, 22mm) are due to the FTS rather then being a feature of the lens, since it was producing a lot of glitches at that time which produced some noisy interferograms.

The results from both polarisations are shown in Figure 5.20. Again, this raw result can be adjusted to compensate for the difference in backgrounds, which is shown in Figure 5.21.

Detector scanning results

From these initial results it was decided to rearrange the experimental setup, by placing the detector linear stage so it can scan perpendicular to the lens. This now allows for the physical centre of the lens to be aligned with the output of the FTS, which means that it will now be under constant uniform illumination. The procedure for these measurements were the same as before, except a beam profile of the standard lens was taken. The focal length of the lens was found to be 250mm, which matches the design. The beam profiles for each polarisation and the original lens at 150GHz is shown figure 5.22. The results were normalised to themselves so that the beam profiles can be compared. It can be seen

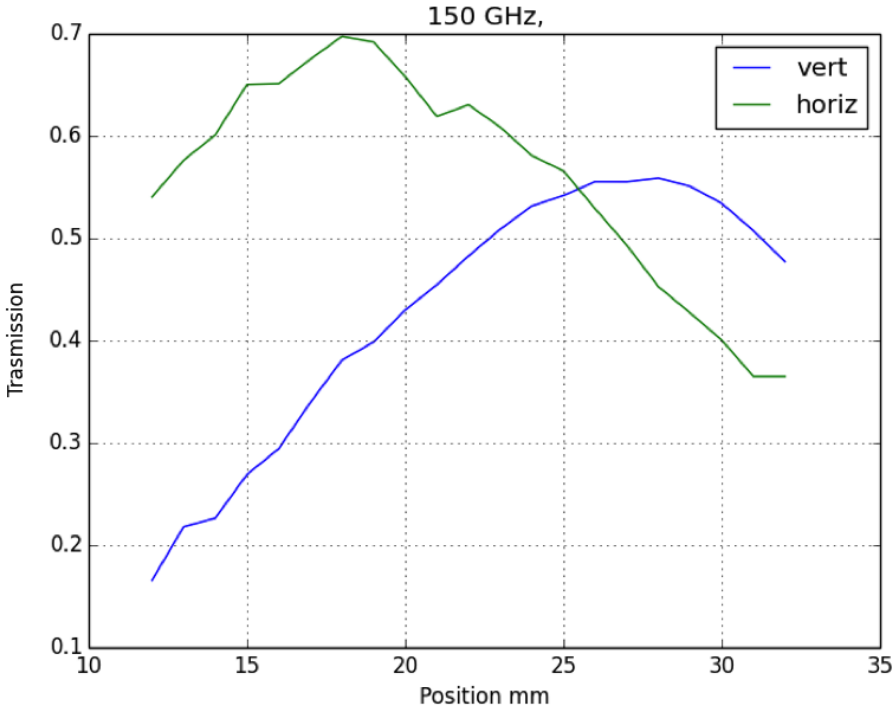

Figure 5.15: Beam profile of the lens for each polaisation.

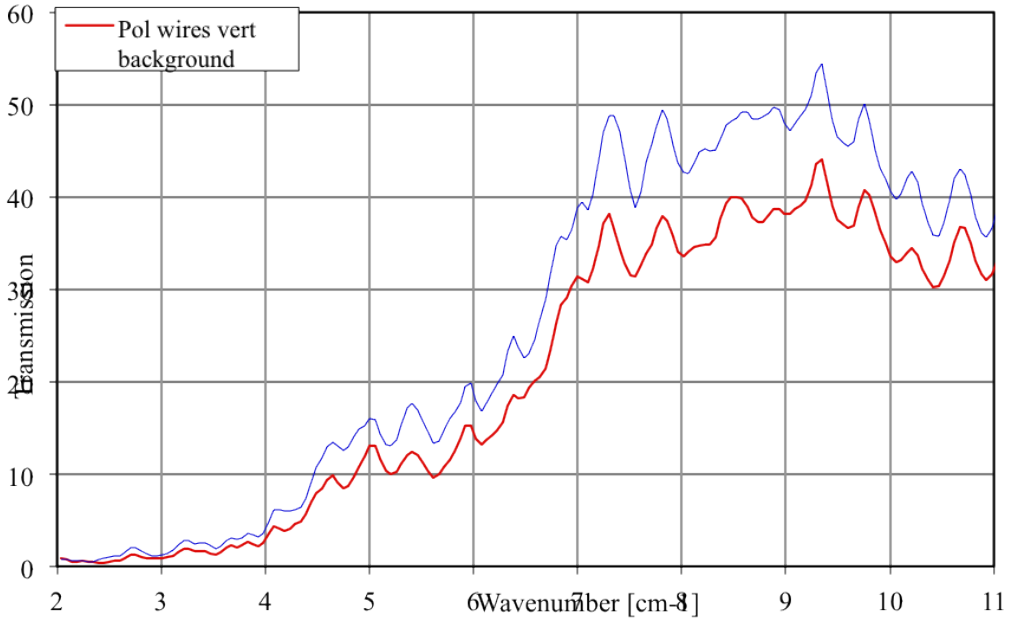

Figure 5.16: The two measured backgrounds. Shows the difference in coupled total power due to the alignment.

that the focus separation is 8.14 mm, slightly less then the original design. The full width half maximum (FWHM) of the polarised beams is slightly larger when compared to the

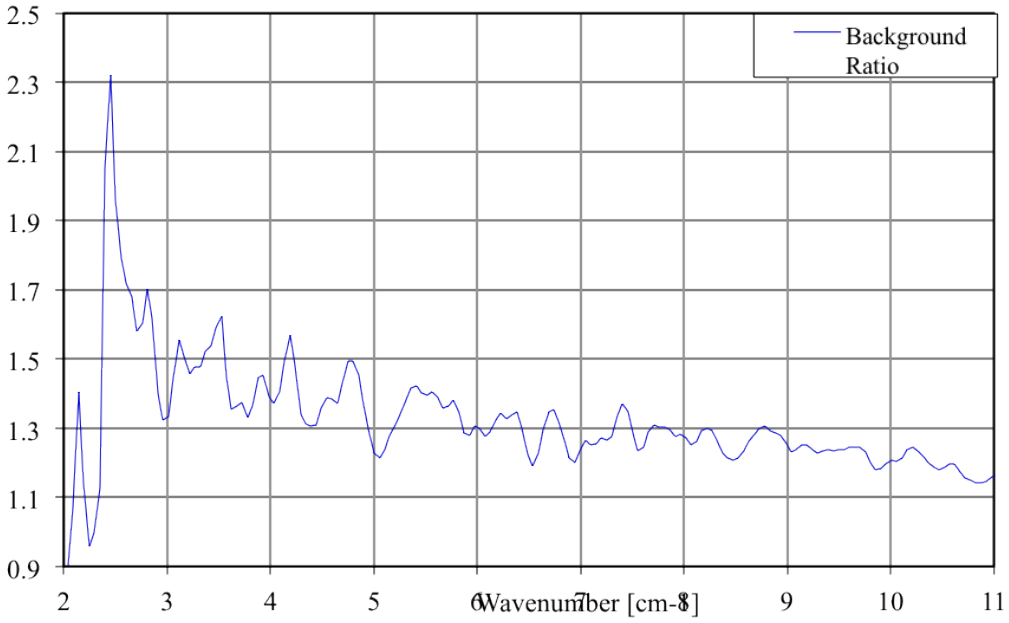

Figure 5.17: Ratio of the two different background measured. Ideal case should be 1 across all wave numbers.

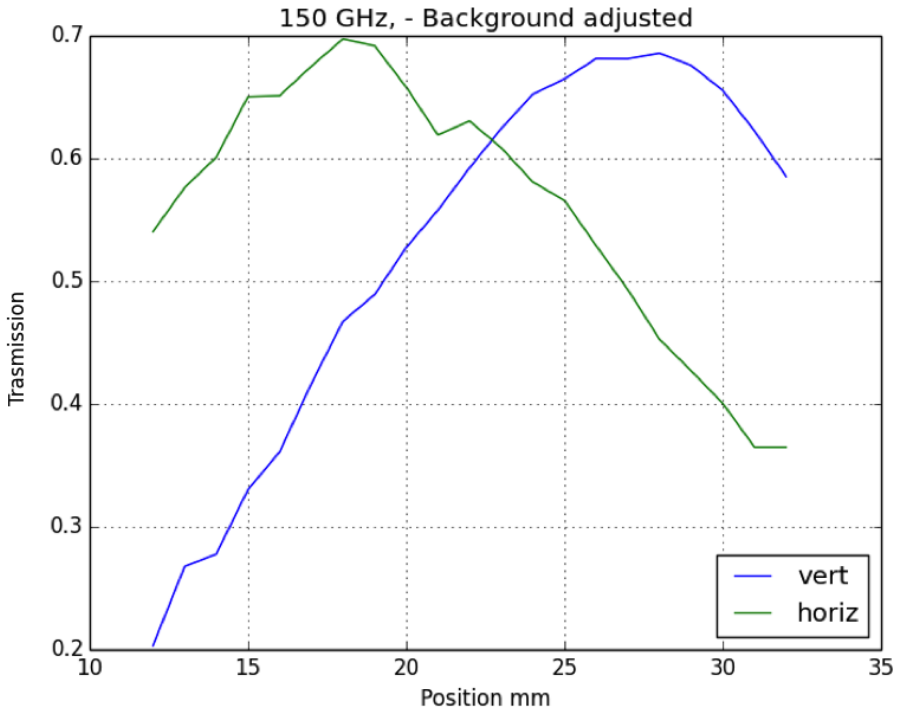

Figure 5.18: Adjusted lens profile. Both beam profiles are level once the background has been taken into account.

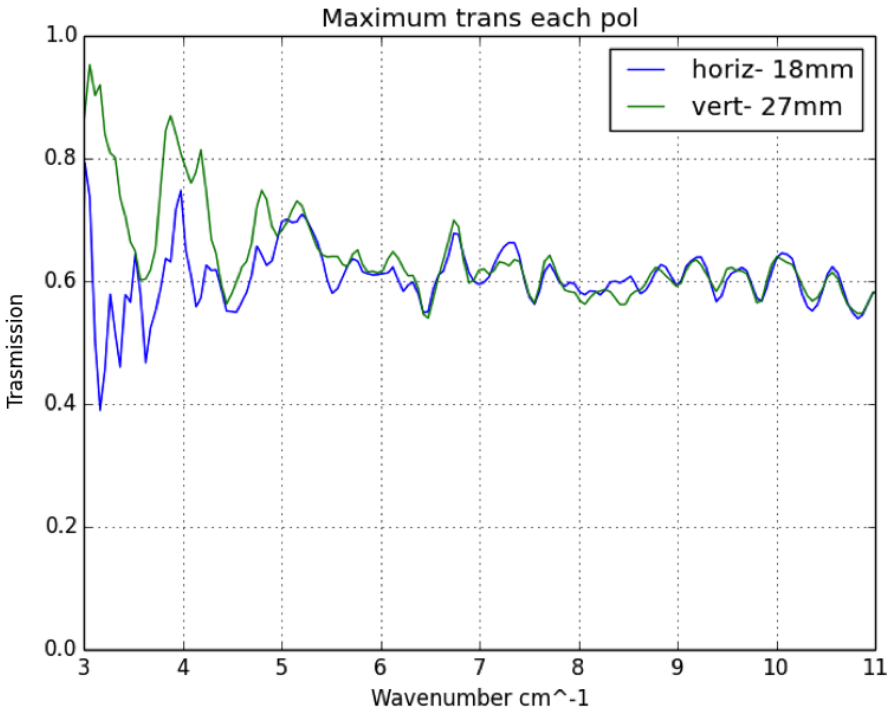

Figure 5.19: Spectral response is nearly identical now for both polarisations.

original lens. This also shows that the beam shape for each polarisation is similar which is shown in figure 5.23. This is important for the practical applications of the lens since any major differences between polarisations would introduce extra systematics into the results.

Another important property of the lens that must be taken into account is the chromatic nature of the lens. Figure 5.24 shows the same result at 320 GHz. This shows that the separation between polarisation has now increased to 11.15mm as well as the beam width becoming narrower. This could be due to the dispersion effects that are occurring due to the mesh girds. However, further results need to be taken, ideally with a network analyser, to fully understand the chromatic nature of the lens. However, this was not available at the time.

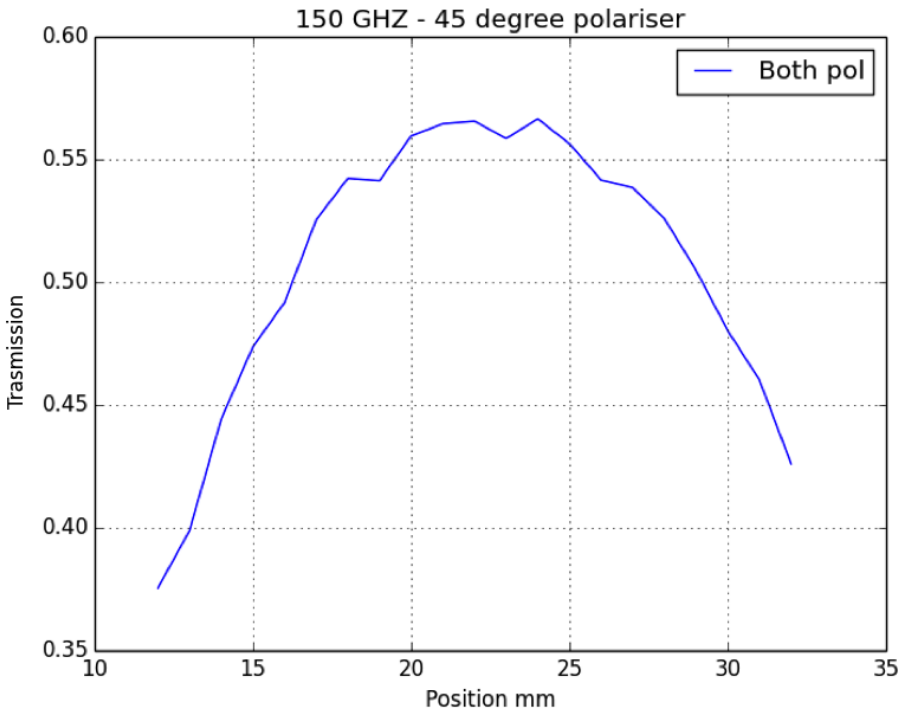

Figure 5.20: Spatial response is nearly identical now for both polarisations.

Figure 5.21: Spatial response is nearly identical now for both polarisations.

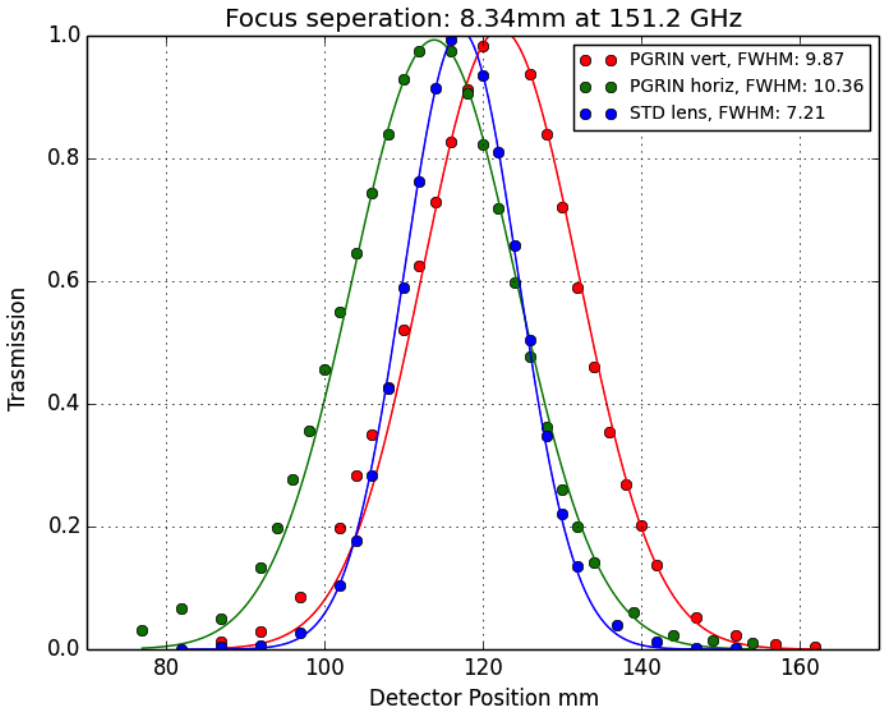

Figure 5.22: Beam profile comparisons between the GRIN lens and the original lens. The separation between polarisation was smaller then expected.

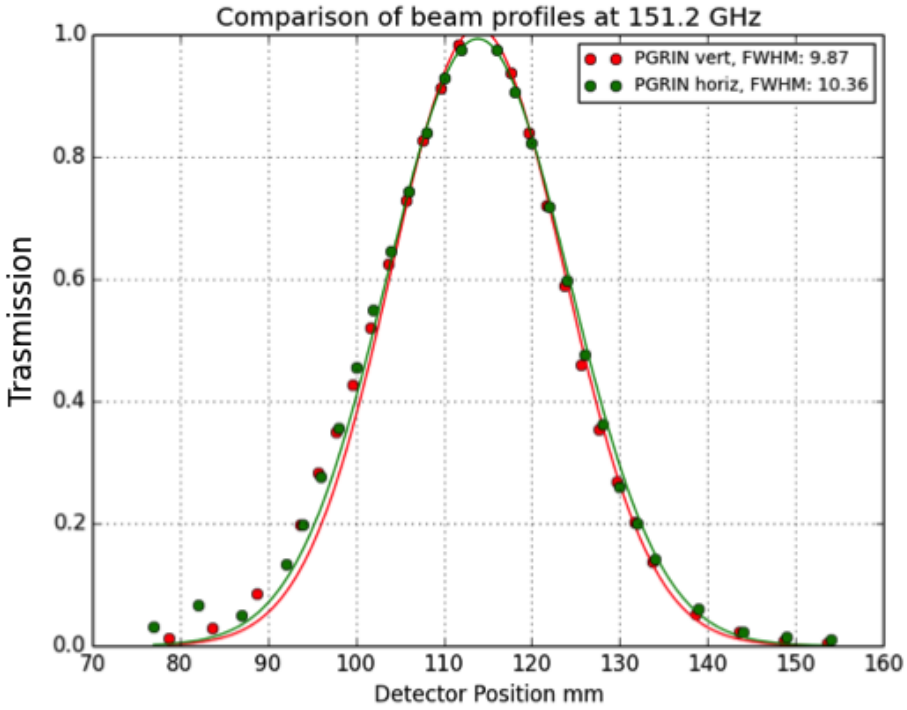

Figure 5.23: Direct comparison between beam profiles for each polarisation.

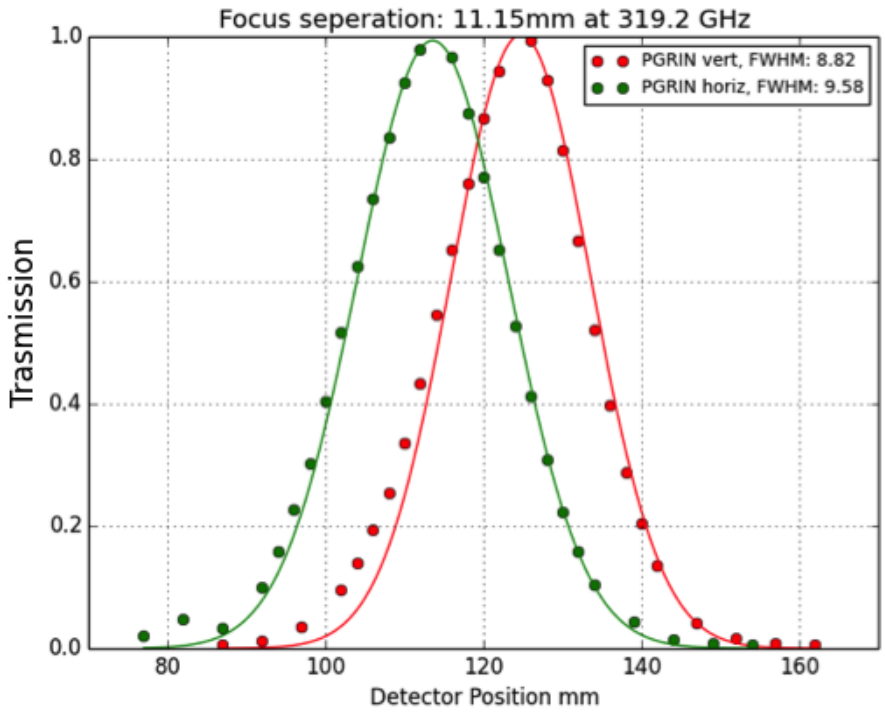

Figure 5.24: The beam comparison between polarisations at 320GHz. The separation between focus has now increased to 11.15mm.

5.3 Conclusion

It has been shown that a polarisation splitting lens using metal mesh technology is possible[47][48]. A clear focal separation was achieved, which matched up with predicted results. This also proves that it is possible to design a spatially varying anisotropic patch structure by modelling each element as a infinite periodic sheet. In the near future further characterisation of the lens will be required to determine its expected spectral performance as well as off-axis behaviour. This can be achieved by using a network analyser setup as detailed in Chapter 4.

Further improvements of the lens design can be made by maximising the transmission response of the lens by introducing an anti-reflection coating, which would also have to be polarisation dependent. Further work can be done exploring graded index designs which a differ from the Woods formalism, such as using a hyperbolic index profile or designs derived from transformation optics [49]. These designs would aim to maximise possible separation between focus, while retaining the same focusing performance.

This page was intentionally left blank

Chapter 6

Metamaterial Half Waveplates

6.1 Half Waveplate Applications

The control of refractive index subject to the direction of polarisation opens another field of specific devices in far-infrared instrumentation: polarisation modulation. A number of experiments in astronomy instrumentation are designed specifically with the objective to measure the polarisation fraction of the radiation being observed. These vary in specifics depending on whether they are designed to measure a small fraction (around 1 percent) of a bright signal, such as the sub-mm polarised emission in star forming regions to assess the role that magnetic fields have in the star formation process (Blast-pol, Rover, POL-2) [50] [51] [52]or if they are targeting an almost negligible fraction of a vastly extended emission such as the polarisation of the microwave background radiation (Spider, EBEx, Polarbear) [53] [54] [55].

Building a half waveplate (HWP) (which is the required modulating element as it leaves the unpolarised signal ideally untouched) can be achieved at these frequencies in a number of ways. Evolving from bi-refringent crystal [56] [57] builds to quasi-optical/waveguide modulation elements in the case of low frequency [58] to recently metal-mesh photo-lithographic waveplates which employ some similar techniques as those discussed. In this chapter we will focus in particular on one of these family of HWPs which are designed to observe the cosmic microwave background.

The cosmic microwave background has been of much scientific interest since its acci-

dental discovery in 1964. Since then, many experiments have progressively mapped its temperature fluctuations[59][60] in more and more detail.

In the last decade, theoretical predictions of the expected fractional polarisation of this signal have been verified with measurements first below 30GHz (DASI) [61] and then subsequent with full sky data below 90GHz (WMAP)[60] and in small patches of the sky with other ground-based or balloon experiments at higher frequencies where the degeneracy with the polarisation signal originating from the dust requires untangling.

The nature of the CMB polarisation can be broken down in E and B modes due to the analogy with the distribution of the vectors in the sky and the electro magnetic fields. The B modes have yet to be measured which would act as proof for gravitational waves. However, the expected B mode signal is expected to have a root mean squared (RMS) value of 100 nk and is about a factor of 100 smaller than the measured temperature anisotropy, this is illustrated in figure 6.1. It is a factor of 10^7 smaller then the temperature of the CMB. Since the signal is so much fainter, it shows that there must be good control on the exact noise of the system and any systematics to be able to detect it. Modulating the incident polarisation is a way to improve the overall sensitivity of the instrument as well as removing systematics. This is due to the fact that any additional effects the instrument after the HWP will appear across the whole modulated signal, so can be removed in post processing.

To prove these further theoretical predictions related to the mechanism of inflation, require future instruments to reach to a level of sensitivity and cleanliness which is two order of magnitude more precise than existing instruments.

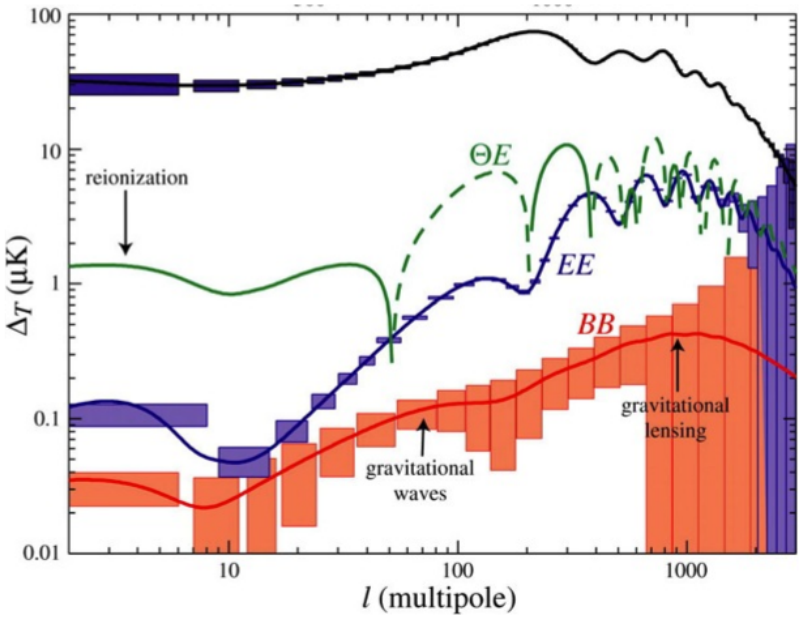

Figure 6.1: The temperature variations of different components of the cmb [62].

6.2 Ideal HWP

A wave plate is a device that is capable of manipulating the polarisation states of a wave by causing a phase delay to the TE or TM component of the wave. Traditionally, HWPs employed birefringent crystals which have optical axes, usually referred to as an ordinary and extraordinary axes, with each offering a different refractive index to the incoming radiation. The crystal is cut so that these two orthogonal axes are parallel to the surface of the wave plate. The speed of the wave traveling through the material depends on the refractive index, so when a plane wave is incident normal to the wave plate, the two linear components each travel along an axes at a different velocity, thus leading to a phase difference between the two when they leave the crystal. By controlling the birefringence of the material and the length of the wave plate, any desired phase change can be selected. This relation is given by equation 6.1, where Γ is the desired phase shift, l is the plate thickness and λ_0 is the target wavelength.

$$\Gamma = \frac{2\pi\Delta n l}{\lambda_0} \tag{6.1}$$

The two most commonly used wave plates are a quarter wave plate (QWP), $\Gamma = \pi/2$ and half waveplate (HWP), $\Gamma = \pi$. A quarter waveplate will convert linear to circular

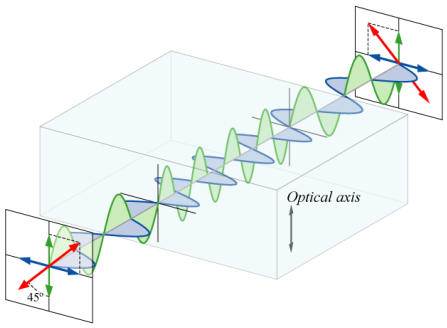

Figure 6.2: An illustration of a simple half waveplate. The incident polarised wave is aligned 45 degrees to the optical axes and then goes through a 90 degree rotation when it exits the crystal. (Figure from [63].)

polarisation. A half waveplate will rotate a linear polarised wave by the the angle 2θ, where θ is the angle between the incident polarised wave and one of the crystal axes in the wave plate. Figure 6.2 shows how a wave is rotated by 90 degrees when $\theta = 45$.

In order to operate with maximum efficiency, there are a number of performance criteria which a HWP design should aim to match. The first case is the minimising the insertion loss, or the loss in transmitted signal by the insertion of the optical element. This combines both the absorption due to the materials used and the reflection at the first surface due to the impedance mismatch from vacuum to the material of the HWP. The second requirement is that the phase difference between the two axes should be 180 degrees over the entire operational bandwidth.

When designing a HWP for use in the next generation CMB instruments there are some specific design details that should be followed and implemented. One major requirement is that it should be the first object in the optical path. This is so that no spurious polarisation generated by the instrument is modulated together with the signal from the sky. In most large focal plane instrument builds, this implies that the HWP now has to be much greater in size than previous wave plates, current designs require a waveplate of the order of 0.5 to 1m in diameter[64]. They also should be easy to be fabricated, easy to implement mechanically,light weight and cryogenically stable [65]. All of theses are made more complicated by the larger size that is required.

So far, most waveplate designs are created using sapphire, due to its low loss and limited dispersion. Since a single waveplate is inherently narrowband in operation, there has been much work into developing achromatic sapphire wave plates [56], these combine multiple waveplates rotated at different angles to each other, so that a series of partial phase shifts

occur to get the overall phase shift required, which is described by Pancharatnam [66].

While these achromatic waveplates have shown to operate very close to the ideal design, they are not capable of meeting the requirements for the future CMB missions. Therefore a new technology must be found that is capable of improving on the existing capabilities while taking into account the numerous added requirements on the size and thermal stability.

6.3 Metal Mesh HWP

6.3.1 Theory

A metal mesh HWP was first proposed by Pisano et.al. in 2008 [63]. There have been various iterations since the first prototype[67]. The basic design concept is to use a pair of quarter-wave plates (one capacitive and one inductive) with opposite compensating frequency dependance that cancel out in a given range to yield a achromatic half-wave plate in the region of interest.

The phase difference is achieved by modelling two different stacks of grids, which emulate the ordinary and extraordinary axes found in a crystal HWP. The challenge is creating two structures that has the desired transmission and phase result for one polarisation state but not the other. So that when combined, the total phase shift is obtained. It has been found that this can be achieved by using a stack of inductive strip gratings to represent one axes and a stack of capacitive grids to represent the other axes. This grid configuration is shown in figure 6.3. Each stack can be be independently modelled since the geometry of the inductive girds is such that when the incident wave is orthogonal to the girds, it is acting as a low pass filter with nearly 100 percent transmission. The same occurs for the capacitive girds which are made using rectangular dipoles, these present very little capacitance to the incoming polarisation when viewed orthogonally. From this approach it is possible to model such devices using the previous transmission line model. Figure 6.4 shows a simulation of one of the early Cardiff prototype grids[68]. It shows that the transmission along each axes is fairly well matched and the phase difference is around 180 degrees.

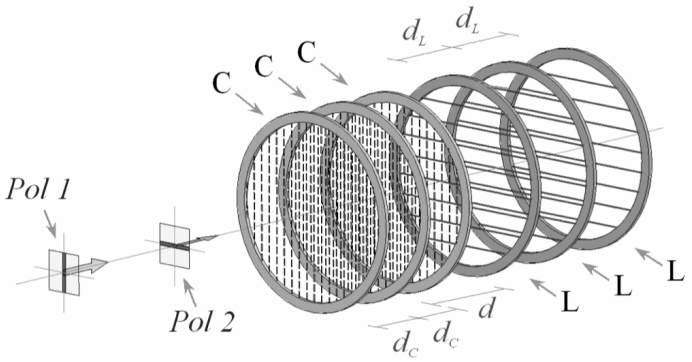

Figure 6.3: Mesh configuration for HWP. It consist of two different stack of metal mesh grids. (Figure taken from [69])

6.3.2 Measurements

Cardiff university have produced two prototype metal mesh wave plates, which were designed to operate around 94 GHz and 150-225 GHz, an example of such is shown in figure6.5, this device is a few mm thick and has a diameter of 80mm . Previous measurements of this HWP have been been made using an FTS [68]. By design, the FTS does not allow full recovery of the phase delay between two orthogonal polarisations. Instead it had to be recovered from the transmission data, which could be prone to other issues such as differential reflection which can then be mistaken for loss due to deviations from the 180 degree phase shift ahead of the second linear polariser. Using the facilities at ESTEC, direct measurements of the phase can be performed using a network analyser.

Quasi-optical bench

To measure the phase and transmission of the HWP, the quasi-optical bench was used in its standard configuration, as shown in Figure 6.6. There was no sample rotator, so the HWP had to be manually rotated. To characterise the HWP, the transmission and phase along each optical axes must be measured. The Tx and Rx antennas are configured to only accept linear polarisation in one orientation. To rotate the polarisation, the horn must be physically rotated. Figure 6.7 shows the various configurations that will be measured.

The co-pol setup has both antennas aligned to the same polarisation. When the HWP is aligned to its optical axes, represented as 0^o and 90^o, there should be maximum transmission in the desired bandwidth. The phase difference between the two axes should equal 180 degrees. When rotated at 45^o there should be no transmission, due to rotating

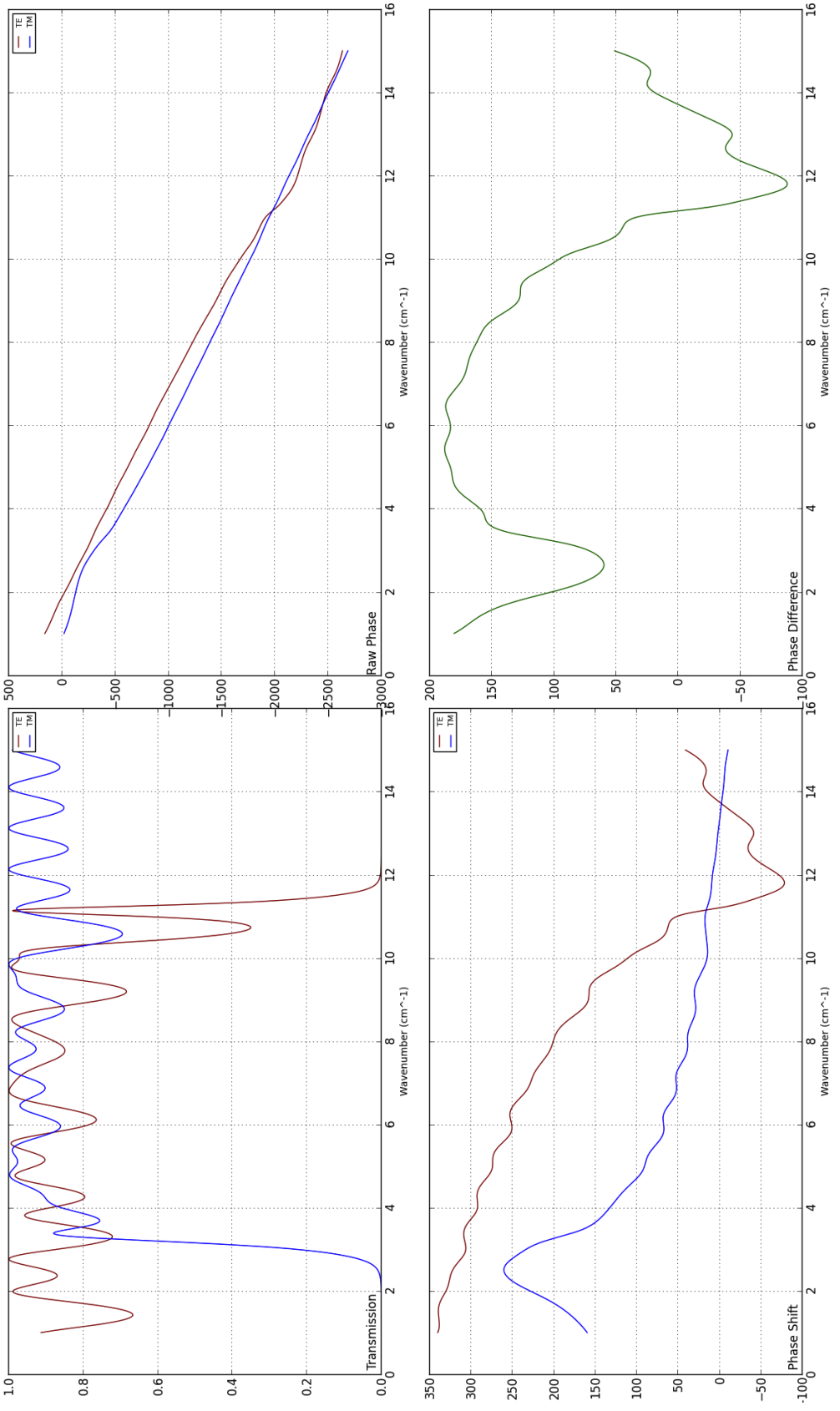

Figure 6.4: Transmission line model predicting the performance of a HWP. It shows that there is good transmission between 3-10 wave numbers, and a fairly flat phase between 4-8 wavenumbers.

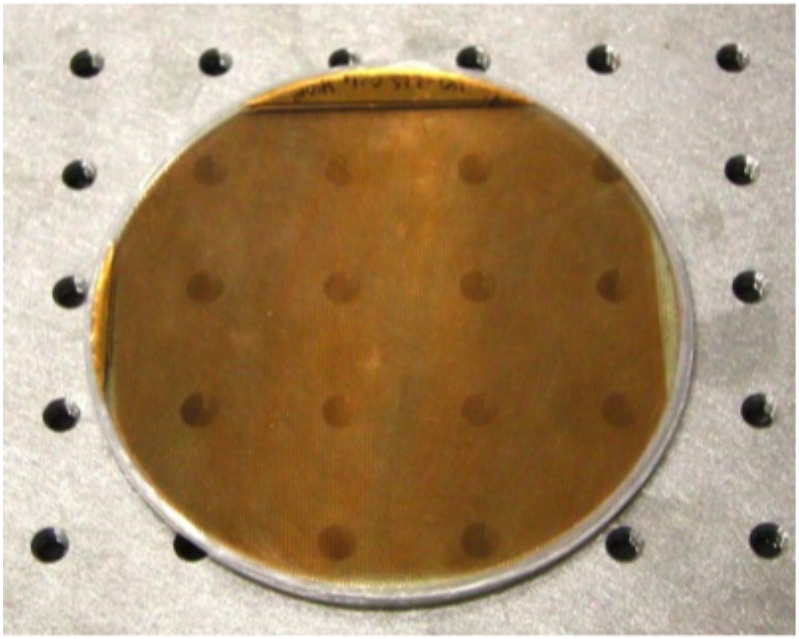

Figure 6.5: A metal mesh half wave plate.

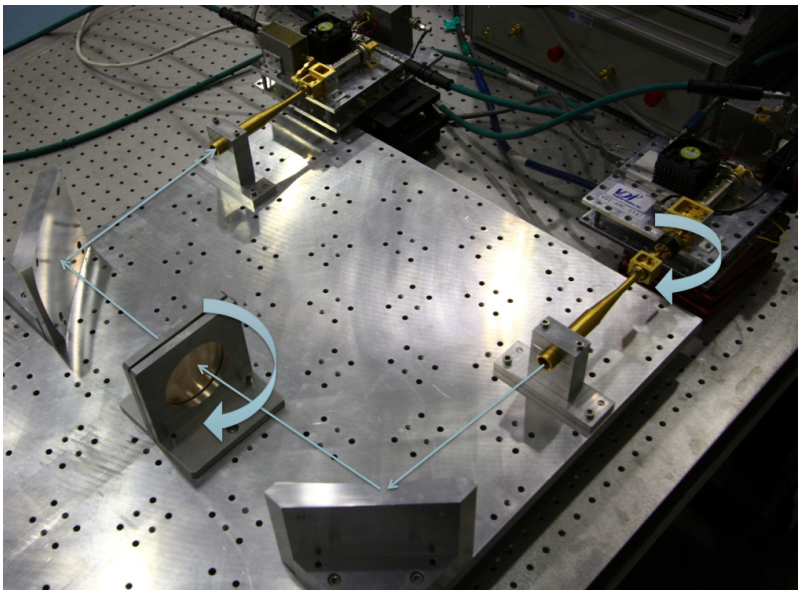

Figure 6.6: Quasi-optical bench to measure transmission and phase of HWP. Corrugated horns are used to launch an receive, while two off-axis parabolic mirrors are used to create a plane wave at the sample position.

the polarisation by 90^o. In the case of the cross-pol setup, where the antennas have different orientations, the results should be swapped.

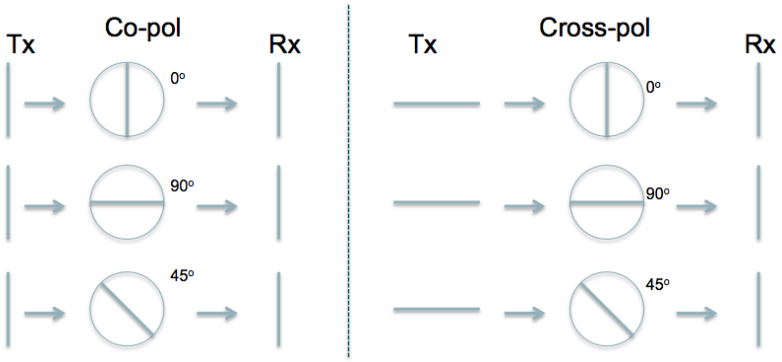

Figure 6.7: Different possible configurations of horns and HWP

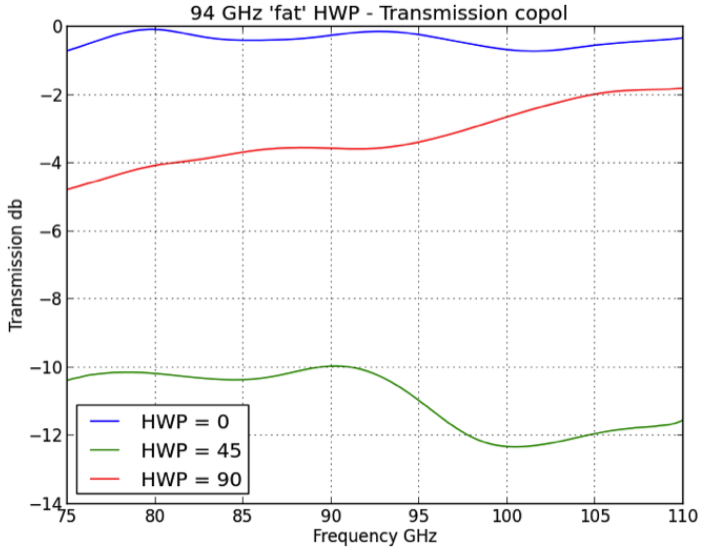

Figure 6.8: Transmission along each axes, in co pol. There is good transmisison along one axis, but not for the other.

Results

The results of the 94 GHz HWP are shown in Figures 6.8, 6.9, 6.10. From the transmission results it can be seen that there is a large discrepancy between transmission along each axes. However, the phase results show a fairly flat phase difference, but did not match 180 degrees as required. The reasons for this discrepancy is that there could have been an over etching of one of the girds in the manufacturing process. This would effect the transmission along one of the axis and thus change the overall phase difference. In future devices this can be varied by adjusting the model parameters to see if the measured data can fit the model.

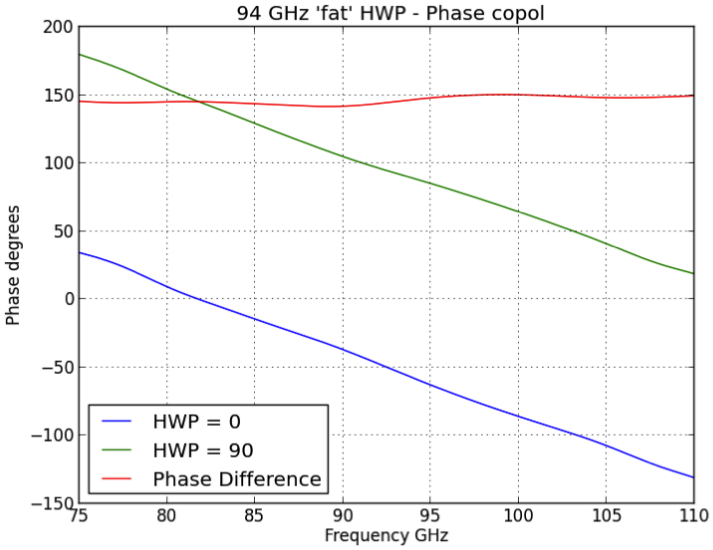

Figure 6.9: Phase difference of HWP. This shows a flat phase difference, but is does not meet the design requirements of 180 degrees.

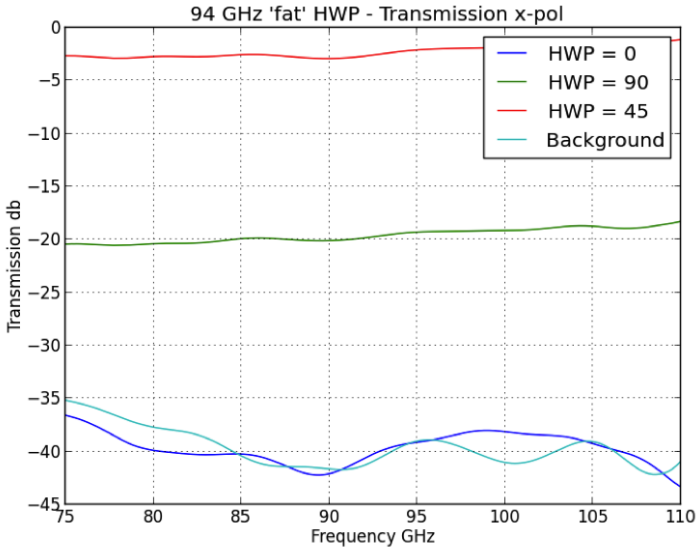

Figure 6.10: Transmission along each axes, in cross pol. Since the phase difference isnt 180 degrees, the rotated power at 45 degrees is much lower then expected.

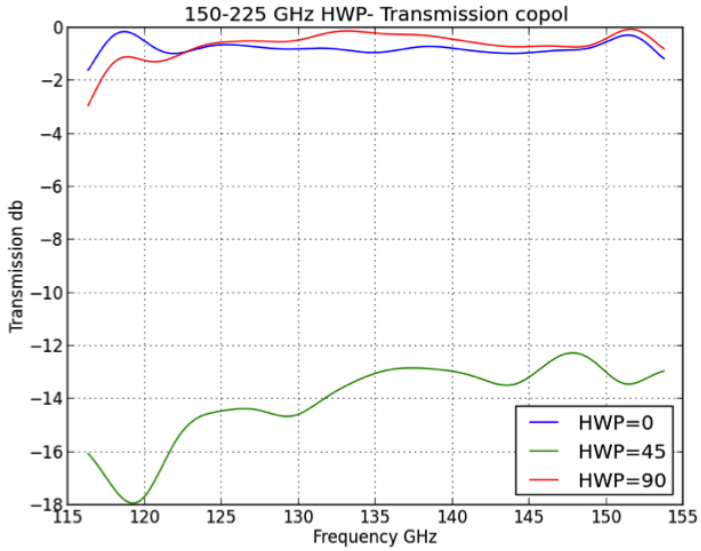

Figure 6.11: Transmission along each axes, in co pol.

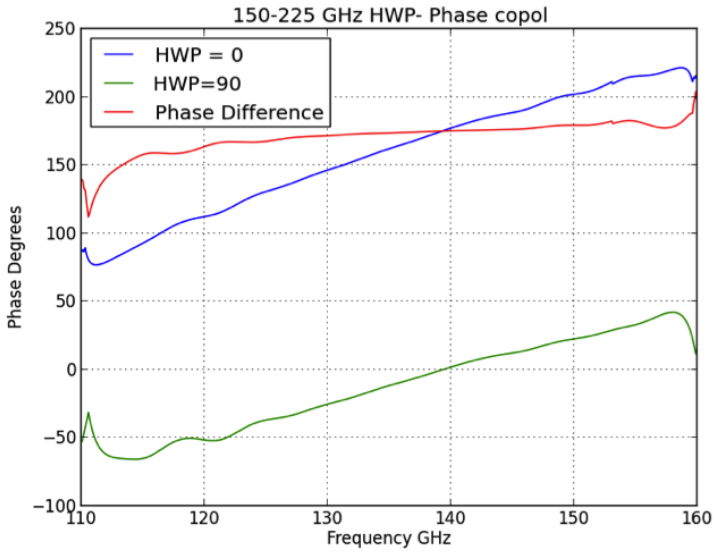

Figure 6.12: Phase difference of HWP.

The results at 150-225 GHz show an improvement, Figures 6.11, 6.12, 6.13. The transmission along each of the axes have a similar value as required to avoid inducing instrumental polarisation, there is minimal polarisation leakage between axes. The measured phase difference is closer to 180 degrees.

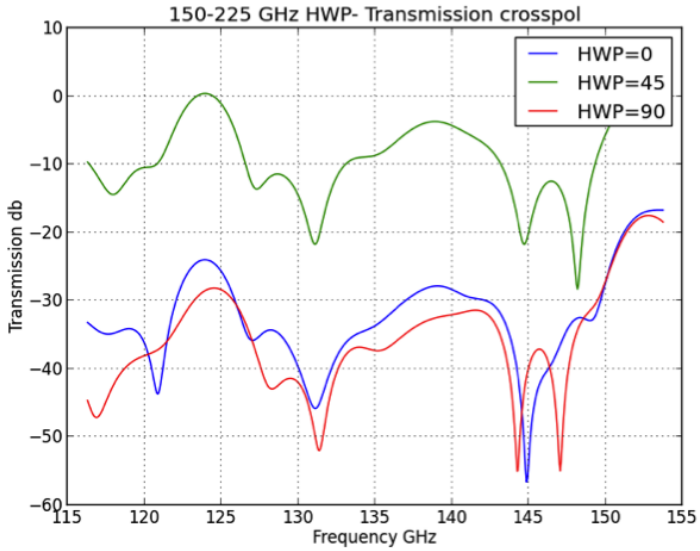

Figure 6.13: Transmission along each axes, in cross pol.

6.4 Future designs

All the previous metal mesh designs detailed use the same two types of grids, inductive strips and capacitive dipoles used in a simple configuration. Detailed below are some examples of using different types of geometry to create a half wave plate.

6.4.1 Artificial Crystal Waveplate

In chapter 3, it was shown that it was possible to create an artificial birefringent dielectric. This means that it is possible to use this to create a HWP in the same way as a crystal waveplate. As given by equation 6.1, there are two parameters that define the design of a HWP, the difference in refractive index between each axes, Δn, and the thickness of the slab. These two parameters are inversely proportional to each other, meaning the that greater the index difference the thinner the wave plate can be.

An advantage of using an artificial birefringent material, is that it is possible to have control over the birefringence. Sapphire has a birefringence limited to $\Delta n = 0.34$ at 150GHz, whereas using an artificial birefringence it is possible to achieve higher values. However, before attempting to obtain such values it is important to consider the frequency response of the grids, since higher refractive index can be achieved, the cut off frequency will be lower. It is important to note that in the case of a single plate design, the phase response is narrowband, the transmission axes are broad band, which allows for multiple

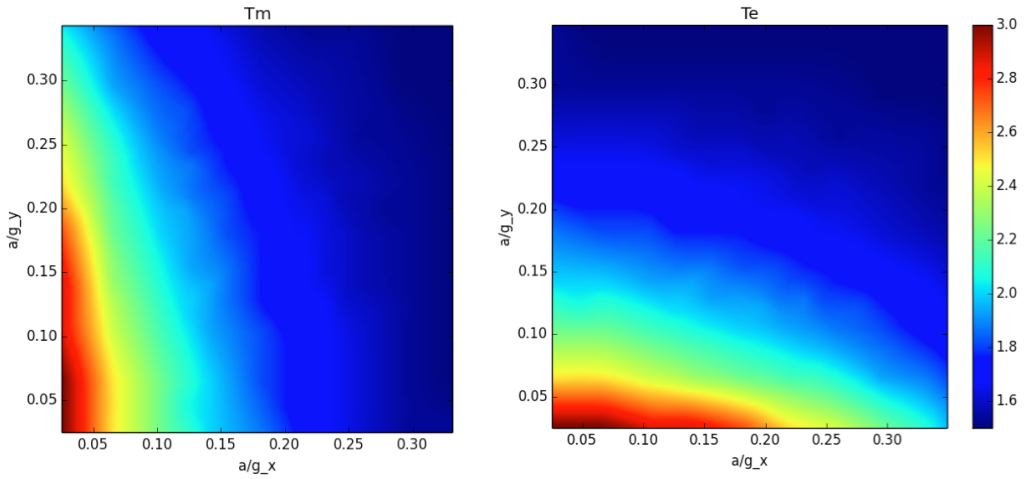

Figure 6.14: Parameter space of patch geometry to give an effective refractive index depending on polarisation.

plates to be combined to from an achromatic wave plate.

Given these criteria, the existing parameter space that was used in designing the polarisation splitting lens in chapter 5, can be used to design a single wave plate. Since it is already been shown that the structure is broadband over the required frequency bands. From figure 6.14 the values of $a/g_x = 0.05$ and $a/g_x = 0.15$, this gives the effective refractive index along each axes as $n_{ord} = 2.5$ and $n_{ex} = 1.9$ which gives $\Delta n = 0.6$. Substituting this into equation 6.1 and choosing a thickness of 1mm, gives a operating frequency of 250 GHz. This requires a stack of 10 grids with a spacing of 100um. This structure can be simulated using HFSS to produce the phase results shown in figure 6.15. The corresponding ideal phase response for an all dielectric wave plate was also plotted but it does not match the simulated phase. By decreasing the overall birefringence to $\Delta n = 0.59$ a better fit was found. The change in birefringence is due to the fact that the calculated refractive index for the grids did not account for dispersion effects, so at 250GHz the difference between values would be closer.

This result shows that an artificial waveplate could be designed, with better understanding of the exact dispersion of the structure. However, due to the number of layers that would be required to fabricate an entire achromatic HWP, it is not a practical solution. The number of layers that are required would be at least 50, given a 5 wave plate design. This is even harder to fabricate if it was to be scaled up to a meter in diameter. Even if a different parameter space was used to design the device, the result would still be the same. This is because, an increase in birefringence could be met by decreasing

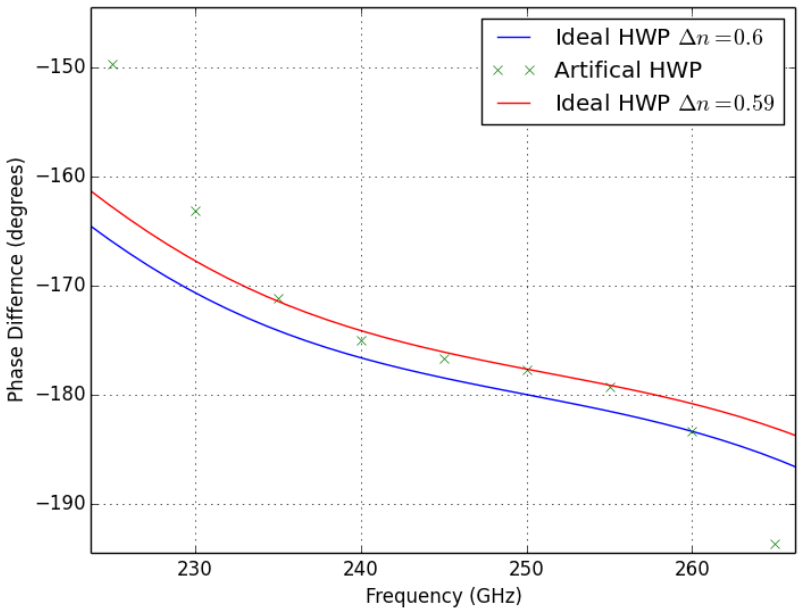

Figure 6.15: Comparison of an simulated performance of an artificial HWP compared to the idea case.

the layer separation, but then more layers would be required to make up the overall required thickness of the plate. Likewise, the distance between layers could be increased in attempt to minimise the number of layers. However, this will have the effect of lowering the birefringence, meaning the physical distance will have to be larger.

This shows that using the metal mesh grids as an artificial birefringent HWP is not practical as a direct replacement in sapphire waveplate design, given that the previous designs have shown promising results using fewer number of grids.

6.4.2 Linear Rotator

It has been recently shown by Grady et al. [70] that is possible to create a linear polarisation rotator using just 3 grids. This is a device which will rotate a linear polarised wave 90 degrees, in the same way that a HWP rotates a linear wave when it is aligned 45 degrees to the incident wave. However, unlike a HWP it can only rotate the polarisation component along one axes. The design that was demonstrated was built to operate at 1-2 THz using gold as the metallic layer and polyimide as the dielectric substrate.

Using the design given in the original paper, a test can be performed to see if it scales down to lower frequencies. The design of the device is given in figure 6.16. It consists of

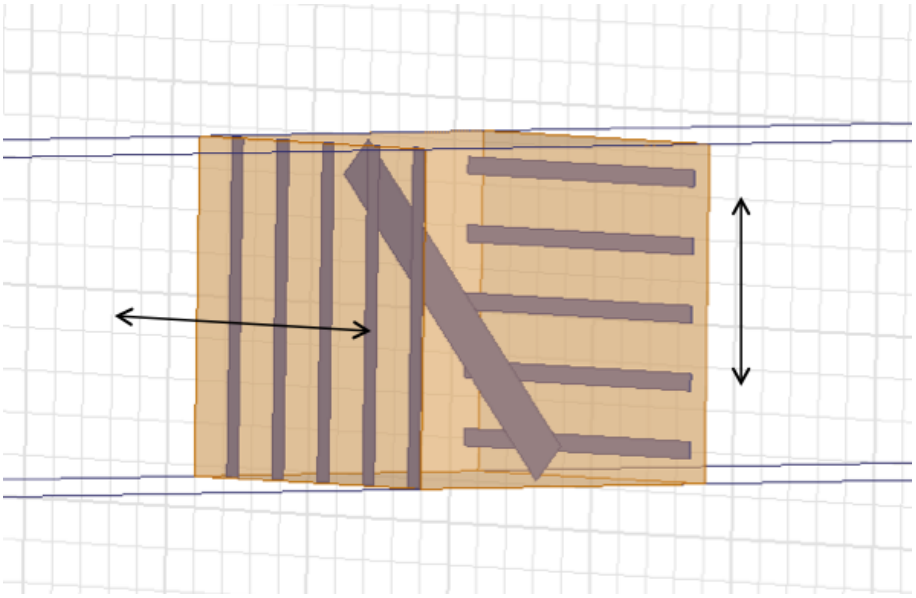

Figure 6.16: Geometry of the linear polarised rotator. An incident wave on the left is rotated by 90 degrees as it leaves on the right.

two, one dimensional gratings, which have a periodicity of 80um and width of 20um.

The geometry is such that when the incident polarisation is orthogonal to the grid, there is a full transmission between 100-370GHz. Then when it is parallel to the grid, it acts as as filter over the same transmission band. They are arranged so they are orthogonal to each other with a separation of 450um. This configuration forms a Fabry-Perot like cavity, such that a polarised wave orthogonal to the first grid is transmitted, but then reflected by the second grid. This means that the only way a wave can by transmitted through the structure is if it is rotated by 90 degrees in between the two grids. This is achieved by placing a rectangular dipole at 45 degrees to the grids, this means that when a linear polarised wave is incident on the dipole, it re-radiates in both polarisation. This is shown in figure 6.17, which is just the transmission through the dipole only. The blue curve shows the transmission of the original linear polarised wave, whereas the green curve shows the the orthogonal component which has been generated by the dipole.

By combing the grid cavity and the dipole a full rotator can be made. The results of this are shown in figure 6.18. This shows that over 94 percent of the incident polarised wave has been rotated by 90 degrees over the frequency range of 100 to 370 GHz. This result shows that some further refinement is needed in exploring the exact geometry required, but it shows that polarisation manipulation can be achieved with only three grids.

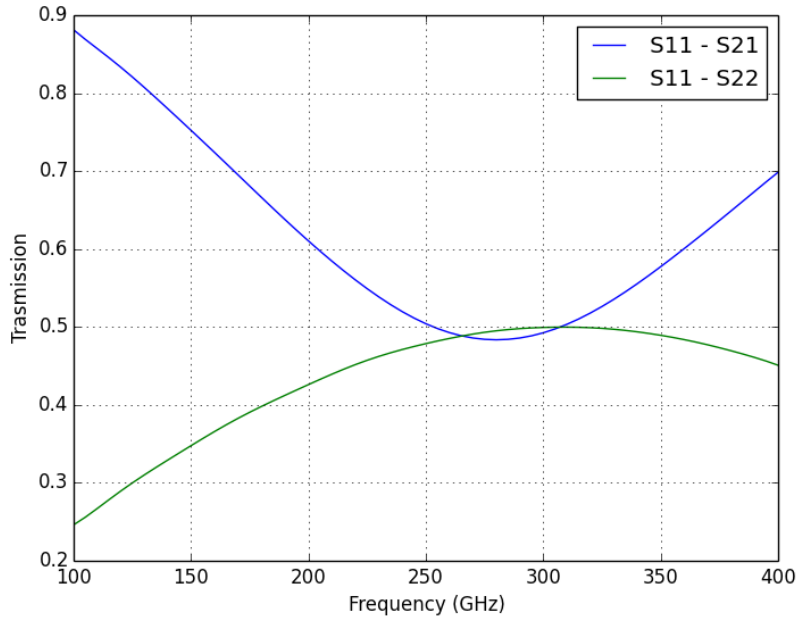

Figure 6.17: Transmission profile of a single dipole which is oriented at 45 degrees. The blue curve shows the original field, and the green shows the orthogonal field re-radiated by the dipole.

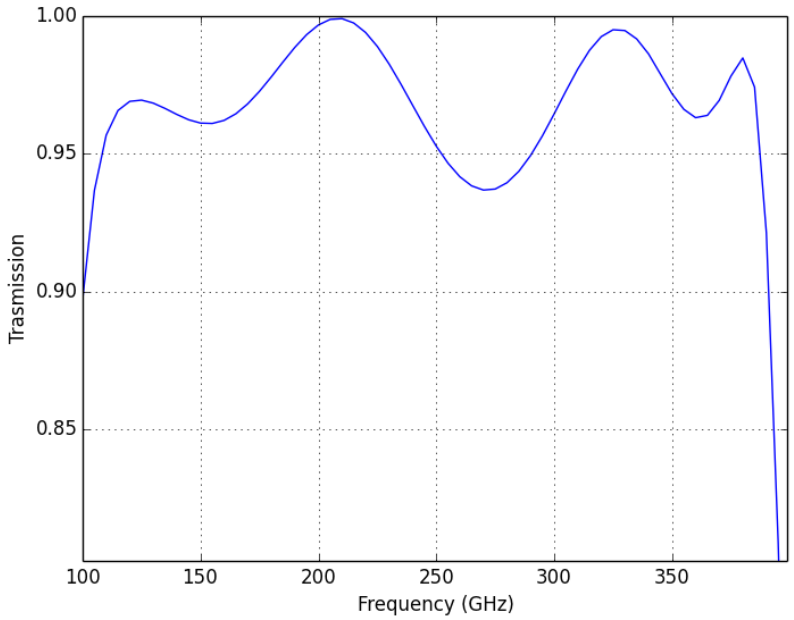

Figure 6.18: Overall transmission response which shows the percentage of the incident wave has been rotated by 90 degrees.

6.5 Conclusion

It has been shown that a metal mesh grid structure can be used to represent a traditional sapphire wave plate. There is still work to be done in finding an optimal design to be able to match the performance that is required, but the practical befits such as scaleability and thermal stability they bring, mean they are an ideal replacement for sapphire waveplates. It has also been shown that attempting to recreate an artificial sapphire waveplate requires too many grids which is not practical due to the cost and time to manufacturing such a device.

This page was intentionally left blank

Chapter 7

Conclusions and Future Work

In this thesis a series of novel quasi optical devices have been presented, as well as the theoretical work of the underlying metal-mesh technology that makes them possible.

It was first shown that a metal mesh grid or frequency selective surface is a type of planar metamaterial which has certain filtering properties based on the geometry of the structure. Because of this behaviour, they are commonly used as filters in THz telescopes. To model these structures, first a transmission line model was developed, which allowed simulating of the propagation of EM fields through various dielectric slabs and how these could be cascaded together. The addition of the metal mesh grids was introduced in to the model by using an equivalent circuit approach. A series of analytical models for capacitive and inductive grids was presented. The use of non-symmetric grids was also presented and which was shown to have different behaviours depending on the orientation of the incident polarised wave.

This sets the foundation for all the future work in this thesis, so was important to have a well behaved model. A lot of time was spent developing a computer code from the theory described. Time was taken to make sure that it was a modular code that could be scaled up depending on the problem that needs to be solved. Deciding on the correct equivalent circuit model to use is critical in a working model. It was found in most cases the Timusk offered the closest approximation. Additional time was taken to upgrade the code so that it can now handle two orthogonal polarisations. This was coupled with the analytical model for non symmetric girds. The results from this model, show that it is

not as accurate as the symmetrical girds, which is due to the increased complexity of the underlying physics occurring in the patch which the model tries to account for. However, it does still allow for an estimate to be made on the performance of the girds.

Chapter 3 demonstrated how it is possible to create an artificial dielectric based on a stack of capacitive metal mesh grids. From the transmission profile of the structure an effective refractive index could be found. By exploring the parameter space of these structures, it was possible to assess the range of effective index values that could be obtained. It was found that a range of effective refractive indexes could be found up to as high as 3.5. Higher values could be obtained by decreasing the spacing between layers. However, it was shown that the transmission line model does not accurately model this due higher order effects that occur. A secondary approach to modelling the grids was undertaken by looking at the band structure that occurs in an infinite stack of grids. The approach allowed for detailed study into the variation of the refractive index with frequency. A simple prism like device is outlined, which shows how it might be possible to exploit these properties of grids to steer light based on its frequency. It was also shown that combining a series of rectangular patches in the same way as the square grids created an artificial birefringent material. This is an important result as it now allows for even greater freedom when designing a device now that the birefringence can be artificially controlled.

These first two chapters described the building blocks which can be used to build a series of devices. The first device presented was a gradient index flat lens. It was designed using existing gradient index theory to mimic a normal polyethylene lens. The lens was further characterised using a quasi optical test bench at ESTEC-ESA. This allowed precise measurements of the lens to be performed both on and off axis. It was proven that it was possible to create a graded index material by slowly varying the size of mesh structure, while still being able to model each unit cell as an infinitely periodic structure. It was also shown that the off-axis behaviour of the lens matches that with an ideal grin lens meaning that the grids did not change the performance of the lens. This is important as it means that future devices can be designed with out having to consider the off-axis behaviour of the girds.

A second lens was also developed, which was an evolution of the first. It was designed to take a randomly polarised source and separate it out into two linearly orthogonal components and focus them separately on the same focal plane. This device could be realised

due to the development of the artificial birefringent material. The lens was fabricated and initial measurements performed using the FTS available at Cardiff University. Two different measurement setups were used to take the data, scanning the lens in front of the beam and scanning the detector. The latter was the preferred method, due to the fact that it could be guaranteed that the lens it uniformly illuminated. In both cases it was shown to perform as predicted, separating out the two polarisation components with a separation of the two foci to be 8mm. From this prototype future devices can now be designed for more specific applications.

Finally a review into the use of half wave plates in astronomy was presented. It was shown that there is a need to produce larger waveplates for future CMB missions and how a metal mesh HWP could be used as suitable replacement. An existing metal mesh HWP is characterised using the quasi optical bench at ESTEC-ESA, since it had not been previously possible to make direct phase measurements. The results showed that there such a device is possible, further work in refining the design is needed. An artificial birefringent waveplate was modelled, which aimed to use the difference in refractive index to cause a phase shift. However, while it was possible, it was shown to be impractical due to the large number of grids that it required. It was then shown how just three grids could be used to rotate the polarisation 90 degrees over a broad frequency range. However, this device was not a true HWP since it can only operate at one angle. However, such a device might use useful in other applications where such a rotation needs to be made in free-space and not in a mechanical waveguide.

7.1 Future Work

There are many ways to expand on the work that has been undertaken in this thesis. With the two lens designs proven there are many other devices which can be fabricated using the same metal mesh materials, such as artificial prisms and compact lens arrays. In the short-term further measurements need to be undertaken on the polarisation splitting lens, to truly understand the chromatic nature of the lens. It is also possible to produce an anti reflection coating for a standard GRIN lens to see if it matches the predicted performance. This would lead on to a verification of the possibility to create a graded index in the the Z direction. While this could never be as smoothly varied, a full three dimension control of the refractive index allows for some devices to be designed using transformation optics

[71]. Another step that needs to be taken is to investigate further the ability to control the individual frequencies, as was done with the polarisation.

There also needs to be further work into the investigation of the behaviour of different meta material structures. There might be other types of structure that can be used to obtain a larger range of effective refractive indexes. To test these new structures more advanced modelling tools will be required if a suitable equivalent circuit representation can not be found. The most suitable method for this would be to implement a full. method of moments solution, due to it increased accuracy, while still being much faster then HFSS. However, implementing such a method if non-trivial and will required a large amount of time dedicated to it.

Appendix A

Appendix A

A.1 Transmission line code

Below is the code that was created for the work in this thesis, to calculate any combination of grids and dielectrics. The code was designed to be modular, so all calculations are calculated in the file tlmm.py. The second file ADBATCHMULTI.py is an example how to use the main code module. The way the two codes interact is given by the basic flow diagram figure A.1. 'ADBATCHMULTI.py' was developed for performing a parameter space, to find the possible obtainable effective index values for a artificial dielectric.. Python was used to due to the familiarity with the language.

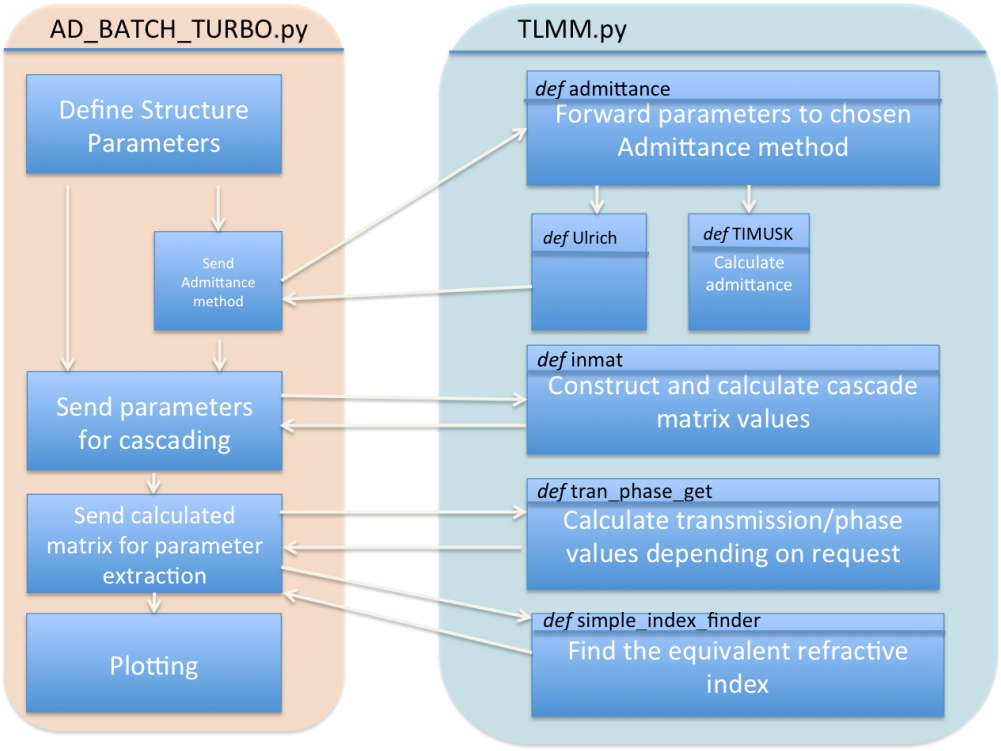

Figure A.1: Flow diagram of data and function calls between programs.

Is capable of dealing with symmetric and non-symmetric grids. The desired admittance method can be specified.

A.1.1 ADBATCHMULTI.py

```
import numpy as np
import scipy as sp
import scipy.ndimage.filters as filters
import scipy.ndimage.morphology as morphology
import matplotlib.pyplot as pl
import os, multiprocessing, datetime,sys
import csv
pl.ion()

#Package capable of calaculating the transmission of metal meshes.
# Either artifical dielectricor hwp.
#Use it making a batch run program or varification.
def loadtest():
        print "TLMM successfully loaded!"

def intmat(Y,grid,n,l,wave,rotation = 0,):
#Y=admitance,grid= grid type (0=nogrid, 1=cap, 2=ind), n = index,
# l=layerthickness , wave=wavelength,
```

```
nn = len(wave)
i = np.complex(0,1)
#!!!!!!!Temp rotation fix!!!!!!!!!
rotation = np.zeros(len(grid))
#!!!!!!!!!!!!!!!!!!!!!!!!!!!!!!!!

A_tot = np.zeros((nn,4,4), complex)
A_te = np.zeros((2,2), complex)
A_tm = np.zeros((2,2), complex)
A_zeros = np.zeros((2,2), complex)

A_add = np.zeros((nn,4,4), complex)
Ainter = np.zeros((nn,4,4), complex)
Alayer = np.zeros((4,4),complex)
A_rotation = np.zeros((4,4), complex)

for k2 in range(nn):

        for k1 in range(len(n)-1):
                A_te = 1./(2.*n[k1]) * np.array([ [-Y[0,k1,k2]+(n[k1]+n[k1+1]),
                        -Y[0,k1,k2]+(n[k1]-n[k1+1])], [Y[0,k1,k2]+(n[k1]-n[k1+1]),
                        Y[0,k1,k2]+(n[k1]+n[k1+1])] ])
                A_tm = 1./(2.*n[k1]) * np.array([ [-Y[1,k1,k2]+(n[k1]+n[k1+1]),
                        -Y[1,k1,k2]+(n[k1]-n[k1+1])], [Y[1,k1,k2]+(n[k1]-n[k1+1]),
                        Y[1,k1,k2]+(n[k1]+n[k1+1])] ])

                Ainter[k2, 0:2, 0:2] = A_te
                Ainter[k2, 0:2, 2:4] = A_zeros
                Ainter[k2, 2:4, 0:2] = A_zeros
                Ainter[k2, 2:4, 2:4] = A_tm

                if k1 < len(n)-2:
                        if grid[k1] == 2:
                                #Mesh is inductive so use inverted propagation matrix.
                                gamma = 2.*np.pi*n[k1+1]*l[k1]*wave[k2]
                                Alayersub = np.array([[np.exp(-i*gamma),0],
                                        [0,np.exp(i*gamma)]])
                                Alayer[0:2, 0:2] = Alayersub
                                Alayer[0:2, 2:4] = A_zeros
                                Alayer[2:4, 0:2] = A_zeros
                                Alayer[2:4, 2:4] = Alayersub
                        else:
                                gamma = 2.*np.pi*n[k1+1]*l[k1]*wave[k2]
                                Alayersub = np.array([[np.exp(-i*gamma),0],
                                        [0,np.exp(i*gamma)]])
                                Alayer[0:2, 0:2] = Alayersub
                                Alayer[0:2, 2:4] = A_zeros
                                Alayer[2:4, 0:2] = A_zeros
                                Alayer[2:4, 2:4] = Alayersub
```

```
                                A_rotationsub1 = np.array([[np.cos(rotation[k1]),0],
                                        [0,np.cos(rotation[k1])]])
                                A_rotationsub2 = np.array([[np.sin(rotation[k1]),0],
                                        [0,np.sin(rotation[k1])]])
                                A_rotation[0:2, 0:2] = A_rotationsub1
                                A_rotation[0:2, 2:4] = -A_rotationsub2
                                A_rotation[2:4, 0:2] = A_rotationsub2
                                A_rotation[2:4, 2:4] = A_rotationsub1


                                Ainter[k2] = A_rotation.dot(Ainter[k2].dot \
                                        (np.linalg.inv(A_rotation)))

                                A_add[k2] = Ainter[k2].dot(Alayer)


                                if k1 == 0:
                                        A_tot[k2] = A_add[k2]
                                else:
                                        A_tot[k2] = A_tot[k2].dot(A_add[k2])

                        else:
                                if k1 == 0:
                                        A_tot[k2] = Ainter[k2]
                                else:

                                        Ainter[k2] = A_rotation.dot(Ainter[k2].dot \
                                                (np.linalg.inv(A_rotation)))
                                        A_tot[k2] = A_tot[k2].dot(Ainter[k2])

        return A_tot

def admitance(params,method,grid,n,wave):
#Returns two values of admitance, one for 'fast' one for 'slow' axis
#       - the same if square
#Inputs: params = (a,g,0,0) x ngrids OR (a,b,c,d) x ngrids
#                method = see dict
#                grid = 0-nogird 1-capgrid  2-indgrid 3-1d capgrid 4-1d indgrid
#            n = index - len(grids)+1
#                !!!!Dimensions are in cm. so 100 microns is passed as 100E-4!!!
#If size of parmas is 2 then geometry is square or infinite wires.
#If 4 then recatangle or diople.
#Have to specify if 2d or wire by choice of method. - code cant tell.
#
#Outputs: Admitance(size: 2(fast/slow), nlayers, wave)

#!!!!!!!!!!!!!!!!!!!!!!!!!!!!!!!!!!!!!!!!!!!!!!!
#!!!! len grid = len params = len method!!!!!
#!!!!!!!!!!!!!!!!!!!!!!!!!!!!!!!!!!!!!!!!!!!!!!!
```

```
methods = {1:admitanceelena,2:admitancelzrect, 3:admitancetim,
 4:admitancetimmod,5:admitanceulrich, 6:admitancelz,
  7:whitborn, 8:moseley}

slow_params = np.zeros(params.shape)
fast_params = np.zeros(params.shape)

fast_params = params

for i in range(len(grid)):
        #Effectivly rotates the geometry 90 degrees.
        #print params[3][i]
        if params[3][i] == 0:
                slow_params[0][i] = (params[1][i]-2*params[0][i])/2.
                slow_params[1][i] = params[1][i]

        else:
                slow_params[1][i] = params[0][i]
                slow_params[0][i] = params[1][i]
                slow_params[3][i] = params[2][i]
                slow_params[2][i] = params[3][i]

y = np.zeros((2,len(grid),len(wave)),complex)

for i in range(len(grid)):

        #Casts admit into chosen method function.
        #Each method must have same imput params.
        #Does one grid at a time. So can use any compination of
        #methods when modeling a composite

        admit = methods.get(method[i])

        if grid[i] ==0:
                y[0,i] = 0
                y[1,i] = 0

        #test for 1-d grids. Eg cap grid rotated 90 deg becomes inductive
        #and vic-verca.
        elif grid[i] == 3:
                y[0,i] = admit(fast_params.T[i],n[i],n[i+1],wave,1)
                y[1,i] = admit(slow_params.T[i],n[i],n[i+1],wave,2)

        elif grid[i] == 4:
                y[0,i] = admit(fast_params.T[i],n[i],n[i+1],wave,2)
                y[1,i] = admit(slow_params.T[i],n[i],n[i+1],wave,1)

        else:
```

```
                        y[0,i] = admit(fast_params.T[i],n[i],n[i+1],wave,grid[i])
                        y[1,i] = admit(slow_params.T[i],n[i],n[i+1],wave,grid[i])

        return y

##########################################################################
#########################ADMITANCE METHODS################################
#Each method must have same inputs:
#admitanceNAME(params,n1,n2,wave,grid)
#Up to method to use required info
#Returns 1-d admitance values as a fucntion of wavenumber
#If new method added, add to dictonary method.
##########################################################################

def admitanceulrich(params,n1,n2,wave,grid):
#admitanceNAME(params,n1,n2,wave,grid)
        #Test 1) n is largest array, l = n - 2 , y = n -1, grid = y (comparing lengths)

        j = np.complex(0,1)
        y = np.zeros(len(wave),complex)
        R=0

        a = params[0]
        g = params[1]

        om=wave*2*np.pi

        #om_0 = (1-0.27*a/g)*2*np.pi/g
        om_0 = (1-0.27*a/g)
        bigOm = om/om_0 - om_0/om

        c = g - 2.*a

        if grid ==1:

                Y_0 = ((n1**2+n2**2)*np.log(1./np.sin(np.pi*a/g)))
                y = 1./(R+j*bigOm/Y_0)
        else:
                Y_0 = np.log(1./np.sin(np.pi*a/g))
                y = (R+j*bigOm/Y_0)

        return y

def admitancetim(params,n1,n2,wave,grid):


        a = params[0]
        g = params[1]

        j = np.complex(0,1)
```

```
        y = np.zeros(len(wave),complex)
        R=0

        om=wave*2*np.pi
        om_0 = 2*np.pi/g

        bigOm = om/om_0 - om_0/om
        R=0

        if grid ==1:

                Y_0 = 2*((n1**2+n2**2))*np.log(1./np.sin(np.pi*a/g))
                y = 1./(R+j*bigOm/Y_0)



        else:

                Y_0 = np.log(1./np.sin(np.pi*a/g))
                y = (R+j*bigOm/Y_0)


        return y

def admitancetimmod(params,n1,n2,wave,grid):
        #admitanceNAME(params,n1,n2,wave,grid)
#        Modified method based on compton
grid = y (comparing lengths)

        a = params[0]
        g = params[1]

        j = np.complex(0,1)
        y = np.zeros(len(wave),complex)
        R=0


        om=wave*2.*np.pi
        om_0 = (2.*np.pi*wave*2.*np.pi)/g
        bigOm = (om/om_0) - (om_0/om)


        if grid ==1:

                Y_0 = 4*np.pi*wave*(n1**2+n2**2)*np.log(1./np.sin(np.pi*a/(g)))
                y = 1./(R+j*bigOm/Y_0)



        else:
```

```
                om=wave*2*np.pi
                om_0 = 2*np.pi/g
                bigOm = om/om_0 - om_0/om

                Y_0 = np.log(1./np.sin(np.pi*a/g))
                y = (R+j*bigOm/Y_0)

        return y

def         whitborn(params,n1,n2,wave,grid):

        a = params[0]
        g = params[1]

        j = np.complex(0,1)
        y = np.zeros(len(wave),complex)
        R=0
        om = g*wave
        #om_0 = 0.906
        om_0 = 1.
        om_0prime = om_0 *np.sqrt(2./(n1**2+n2**2))
        bigOm = om/om_0 - om_0/om
        xcap = ((2./(n1**2+n2**2))*bigOm)/(4*om_0prime*
                np.log(1./np.sin(np.pi*a/(g))))

        return j/xcap



def admitancelz(params,n1,n2,wave,grid):
#admitanceNAME(params,n1,n2,wave,grid)
        a = params[0]
        g = params[1]


        j = np.complex(0,1)
        y = np.zeros(len(wave),complex)
        R=0
        om=wave*2*np.pi

        om_0 = (1-0.41*a/g)*2*np.pi/g
        bigOm = om/om_0 - om_0/om

        c = g - 2.*a


        if grid ==1:
                Y_0 = (((n1**2+n2**2)/2.)*np.log(1./np.sin(np.pi*a/g)))/((g/c)
```

```
                        + 0.5*(g*wave)**2)
                y = 1./(R+j*bigOm/Y_0)
        else:
                Y_0 = (((n1**2+n2**2)/1.75)*np.log(1./np.sin(np.pi*a/g)))/((g/c)
                        + 0.5*(g*wave)**2)
                y = (R+j*bigOm/Y_0)

        return y


def admitancelzrect(params,n1,n2,wave,grid):
        #admitanceNAME(params,n1,n2,wave,grid)
        j = np.complex(0,1)

        nn=len(wave)

        # wlim =np.array([0.3,14.])  #cm^-1
        # wave=np.linspace(wlim[0],wlim[1],nn)

        freq = 3E10*wave


        lamb = (3e8/ freq)/(np.sqrt((n1**2+n2**2)/2.))


        a = np.complex(params[0]*0.01,0)
        b = np.complex(params[1]*0.01,0)
        c = np.complex(params[2]*0.01,0)
        d = np.complex(params[3]*0.01,0)

        y_ind_p1 = np.sqrt((lamb/a)**2 -1)
        y_ind_p2 = ((np.cos(np.pi*c/a))/(1-(2*c/a)**2))**2
        y_ind_p3 = (1/np.sqrt((lamb/b)**2 - 1))
        y_ind_p4 = ((np.sin(np.pi*d/b))/(np.pi*d/b))**2
        y_ind_p5 =  2*(b/(a+b))#factor 2?
        y_ind_p6 = np.sqrt(((a**2 + b**2)/(a**2*b**2))*lamb**2 - 1)
        y_ind_p7 = (1/y_ind_p6)*(a/b)


        Y1_ind_tot = -j*2*(y_ind_p1*y_ind_p2 - y_ind_p3*y_ind_p4 +\
         y_ind_p5*(y_ind_p6- y_ind_p7)* y_ind_p4*y_ind_p2)

        return 1/Y1_ind_tot


##########################################################################
##########################################################################

def tran_phase_get (A,pol="te",result="b"):
#Takes 4x4 transfer matrix A and can return TE or TM modes and phase
```

```
#transmision or both.
        nn =len(A)
        rhote = np.zeros(nn,complex)
        taute = np.zeros(nn,complex)
        rhotm = np.zeros(nn,complex)
        tautm = np.zeros(nn,complex)


        for k in range(nn):

                rhote[k] = A[k,0,1]/A[k,1,1]
                taute[k] = 1/A[k,1,1]
                rhotm[k] = A[k,2,3]/A[k,3,3]
                tautm[k] = 1/A[k,3,3]

        if pol == "te":

                R1 = abs(rhote)**2
                #T1 = abs(taute)**2
                phase1 = np.rad2deg(np.unwrap(np.arctan2(-taute.imag,taute.real)))
                if result == "b":
                        return 1-R1, phase1
                elif result == 'p':
                        return phase1
                elif result == "t":
                        return 1-R1

        elif pol == "tm":
                R2 = abs(rhotm)**2
                #T2 = abs(tautm)**2
                phase2 = np.rad2deg(np.unwrap(np.arctan2(-tautm.imag,tautm.real)))

                if result == "b":
                        return 1-R2, phase2
                elif result == 'p':
                        return phase2
                elif result == "t":
                        return 1-R2

        elif pol == "b":
                R1 = abs(rhote)**2
                #T1 = abs(taute)**2
                phase1 = np.rad2deg(np.unwrap(np.arctan2(-taute.imag,taute.real)))
                R2 = abs(rhotm)**2
                #T2 = abs(tautm)**2
                phase2 = np.rad2deg(np.unwrap(np.arctan2(-tautm.imag,tautm.real)))

                if result == "b":
                        return 1-R1,1-R2, phase1,phase2
                elif result == 'p':
```

```
                    return phase1,phase2
                elif result == "t":
                    return 1-R1,1-R2

def simple_index_finder(T):
        #based on using the first minimum. - Not ideal at all, But a test for rest of code.
        #want n as a funciton of lambda also cutoff

        mins = detect_local_minima(T)
        mins = mins[0]
        first_min_pos = mins[1]
        first_min = T[first_min_pos]

        n = np.sqrt((2-first_min+ 2*np.sqrt(1-first_min))/first_min)

        return n,first_min_pos

def detect_local_minima(arr):
    # http://stackoverflow.com/questions/3684484/peak-detection-in-a-2d-array/3689710#3689710
    """
    Takes an array and detects the troughs using the local maximum filter.
    Returns a boolean mask of the troughs (i.e. 1 when
    the pixel's value is the neighborhood maximum, 0 otherwise)
    """
    # define an connected neighborhood
    # http://www.scipy.org/doc/api_docs/SciPy.ndimage.morphology.html#generate_binary_structure
    neighborhood = morphology.generate_binary_structure(len(arr.shape),2)
    # apply the local minimum filter; all locations of minimum value
    # in their neighborhood are set to 1
    # http://www.scipy.org/doc/api_docs/SciPy.ndimage.filters.html#minimum_filter
    local_min = (filters.minimum_filter(arr, footprint=neighborhood)==arr)
    # local_min is a mask that contains the peaks we are
    # looking for, but also the background.
    # In order to isolate the peaks we must remove the background from the mask.
    #
    # we create the mask of the background
    background = (arr==0)
    #
    # a little technicality: we must erode the background in order to
    # successfully subtract it from local_min, otherwise a line will
    # appear along the background border (artifact of the local minimum filter)
    # http://www.scipy.org/doc/api_docs/SciPy.ndimage.morphology.html#binary_erosion
    eroded_background = morphology.binary_erosion(
        background, structure=neighborhood, border_value=1)
    #
    # we obtain the final mask, containing only peaks,
    # by removing the background from the local_min mask
    detected_minima = local_min - eroded_background
    return np.where(detected_minima)
```

```
def fp_fit(n,wave,l):
        # r = (1+n)/(1-n)
        # R = r**2
        # l = np.sum(l)
        # #why factor of 3 needed?
        # beta = 2*np.pi*wave*n*l*r/3.
        # fp = 1/(1+(4*R/(1-R)**2)*np.sin(beta)**2)
        # #Add cutoff? Fermi driac bandgap?

        R = (1-n)**2/(1+n)**2

        l = np.sum(l)
        #why factor of 3 needed?
        beta = 2*np.pi*wave*l*n
        fp = 1/(1+4*R*np.sin(beta)**2/(1-R)**2)
        #Add cutoff? Fermi driac bandgap?

        return fp



def index_finder(A,wave,l):
#Effective permitivity recovered, acording to Smith.
        d = np.sum(l)
        n = np.zeros(len(wave))
        j = np.complex(0,1)

        for i in range(len(n)):

                #test = (1/(2*A[i,1,0]))*(1 - A[i,0,0]**2 + A[i,1,0]**2)
                #print test

                k = 2*np.pi*wave[i]

                s11 = A[i,0,1]/A[i,1,1]
                s21 = 1/A[i,1,1]

                n[i] = (1. / (k*d))* np.arccos((1/(2*s21))*(1 - s11**2 + s21**2))

        return np.real(n)

def robust_index_finder(T,wave,l):
        d = np.sum(l)
        n = np.zeros(len(wave))
        j = np.complex(0,1)
        R = 1.-T
        k0 = 2.*np.pi*wave

        s21 = T*np.exp(j*k0*d)
        s11 = R*np.exp(j*k0*d)
```

```
        z = np.sqrt(((1+s11)**2 - s21**2)/((1-s11)**2 -s21**2))
        expval = s21/(1.-s11*((z-1)/(z+1)))

        # X = (1/(2*s21*(1-s11**2+s21**2)))
        # expval = X+j*np.sqrt(1-X**2)
        n=(1/(k0*d))*((np.imag(np.log(expval))+2*0*np.pi)-j*np.real(np.log(expval)))
        #(1/(k0*d))*
        return np.real(n)#,s21

def cutoff_finder(T,wave):
        tlog= np.log(T)
        cutfreq = 0

        for i in range (len(wave)):
                if (tlog[i] < -10):
                        cutfreq = wave[i]
                        break
        return cutfreq

def kk_index_finder(T,phase,wave,l):
        #based on Szabo paper

        s11_abs = 1-T
        s11_phase = 2*np.pi - phase
        s21_abs = T
        s21_phase = phase

        nn=len(wave)
        j= np.complex(0,1)

        d_eff= np.sum(l)
        R = 1.-T


        k = 2.*np.pi*wave
        om= k*3e6



        s11 = s11_abs*(np.cos(s11_phase*np.pi/180.) -
                np.sqrt(-1+0j)*np.sin(s11_phase*np.pi/180.))
        s21 = s21_abs*(np.cos(s21_phase*np.pi/180.) -
                np.sqrt(-1+0j)*np.sin(s21_phase*np.pi/180.))



        z_eff = np.sqrt(((1+s11)**2-s21**2)/((1-s11**2)-s21**2))
        exp_ink0d = s21/(1-s11*((z_eff-1.)/(z_eff+1.)))
```

```
for i in range(len(wave)):
        re_z_eff = z_eff[i].real
        if (abs(re_z_eff) >1e-2):

                if(re_z_eff<0):

                        z_eff[i] = -z_eff[i]
                        exp_ink0d[i] = s21[i]/(1-s11[i]*((z_eff[i]-1.)/
                                (z_eff[i]+1.)))
        else:

                if(abs(exp_ink0d[i])>1.):

                        z_eff[i] = -z_eff[i]
                        exp_ink0d[i] = s21[i]/(1-s11[i]*((z_eff[i]-1.)/
                                (z_eff[i]+1.)))

logexp_ink0d = np.log(exp_ink0d)
neff = (logexp_ink0d.imag - np.sqrt(-1+0j)*logexp_ink0d.real)/
                        (k*d_eff)

imag_n = neff.imag

n_re_kk = np.zeros(len(wave))

delta_om = om[1] - om[0]

term_a = imag_n[1]*om[1]/(om[1]**2 - om[0]**2)

for i in range(1,nn-1):

        term_b = imag_n[i+1]*om[i+1]/(om[i+1]**2 - om[0]**2)
        n_re_kk[0] = n_re_kk[0] + term_a +term_b
        term_a = term_b

n_re_kk[0] = 1.+delta_om/np.pi*n_re_kk[0]

term_a = imag_n[0]*om[0]/(om[0]**2 - om[nn-1]**2)

for i in range(0,nn-3):

        term_b = imag_n[i+1]*om[i+1]/(om[i+1]**2 - om[nn-1]**2)
        n_re_kk[nn-1] = n_re_kk[nn-1] + term_a +term_b
        term_a = term_b

n_re_kk[nn-1] = 1.+delta_om/np.pi*n_re_kk[nn-1]

for i in range(1,nn-2):
        n_re_kk[i] = 0
        term_a = imag_n[0]*om[0]/(om[0]**2 - om[i]**2)
```

```
                for j in range(0,i-2):
                        term_b = imag_n[j+1]*om[j+1]/(om[j+1]**2 - om[i]**2)
                        n_re_kk[i] = n_re_kk[i] + term_a +term_b
                        term_a = term_b

                term_a = imag_n[i+1]*om[i+1]/(om[i+1]**2 - om[i]**2)

                for j in range(i+2,nn-2):
                        term_b = imag_n[j+1]*om[j+1]/(om[j+1]**2 - om[i]**2)
                        n_re_kk[i] = n_re_kk[i] + term_a +term_b
                        term_a = term_b

                n_re_kk[i] = 1.+delta_om/np.pi*n_re_kk[i]

        m_branch = np.round((n_re_kk-neff.real)*k*d_eff/(2*np.pi))

        #neff = neff +2*np.pi*m_branch/(k*d_eff)

        pl.figure()
        pl.plot(wave,neff.real)

        return neff



#=============================================
#Useful stuff
#=============================================



def struct_varification(params, method,grid,n,l,wave,log = 0):
#This function will test to makesure that sizes of all the paramters make sense.

        flag = 0
        error1 = ""
        error2 = ""
        error3 = ""

        if (len(grid)!= len(l)+1) or (len(grid)+1!=len(n)) or (len(n)!= len(l)+2):
                flag =1
                error1 = "Length of arrays do not match"

        else:

                if len(method) != len(params[0]):
                        flag = 1
                        error2 = "Grid Method does not match prameters "

                else:
```

```
                        temp = 0
                        for i in grid:
                                if i != 0:
                                        temp +=1

                        if len(method)!= temp:
                                flag = 1
                                error3 = "Have not correctly defined an Interface."


        errormessage = error1 # + error2.. etc

        if flag != 0:
                print error1, error2, error3
        #if log =1, save arrays to file. - Or another routine?
        #Call by saying if error = struct_Varification
        #                if error != "0", print error, halt/redo
        return errormessage
        #Finish off

def read_hfss_data(filename, headsize = 10):

        freq, trans =np.loadtxt(filename, unpack=True,skiprows = headsize)
        wavenum = freq*0.01*1E9/3E8
        # print "Min wavenumer is :", wavenum[0]
        # print "Max wavenumer is :", wavenum[-1]

        return wavenum, trans

def read_csv_data(filename, headsize = 10):

        filedat = csv.reader(open(filename, "rb"))

        wavenum = np.array(())
        trans = np.array(())

        for i in range(headsize):
                filedat.next()

        for row in filedat:
                wavenum = np.append(wavenum,row[0])
                trans = np.append(trans,row[1])

        print "Min wavenumer is :", wavenum[0]
        print "Max wavenumer is :", wavenum[-1]

        return wavenum, trans
```

A.1.2 tlmm.py

```
from __future__ import division
from multiprocessing import Pool
from matplotlib.patches import Patch
import numpy as np
import scipy as sp
import matplotlib.pyplot as pl
import os, multiprocessing, datetime, sys
#Path to tlmm file.
sys.path.append( "/Users/paulmoseley/Documents/Python/tlmm/" )
import tlmm
import cPickle as pickle
pl.ion()
reload(tlmm)
##############################################################################
#Program to find differnt effective refractive index over large parameter space

#Fixed parms: Number of layers, Uniform Spacing, Uniform dielectric.
#Variable range: a/g and g - Based on ulrich geometry
#Plugin function for finding n.
#Output Pickable file that contains A for all runs.
#Run details are saved in folder names.
#Implement a config file of list of params, method used etc. Time and date stamped.
#This allows to re analise the index when better method is done.

#To do: Program to readback in A. Function to convert from .pickle to .csv
##############################################################################

##############################################################################
###################################Input params###############################

def mainfunc(args):
        params = args[0]
        method = args [1]
        grid = args[2]
        n = args[3]
        l = args[4]
        wave = args[5]

        Y = tlmm.admitance(params,method,grid,n,wave)
        A = tlmm.intmat(Y,grid,n,l,wave)
        T = tlmm.tran_phase_get(A,pol="te",result="t")


        temp_name = open( "%s_%s.p" %(g_range[j]/1e-4,ag_range[i]/1e-4), "wb" )
        pickle.dump((wave,T), temp_name)
        temp_name.close()

        #Select method for extracting n
```

```
        effective_n,pos = tlmm.simple_index_finder(T)
        #effective_n = tlmm.index_finder(A,wave,l)

        #P = tlmm.tran_phase_get(A,pol="te",result="p")
        return effective_n, T.tolist()

#freq resolution
nn=400

#Min and max wave number
wlim =np.array([0.1,20.])  #cm^-1
wave=np.linspace(wlim[0],wlim[1],nn)

#Parameter Resolution - Square grid only.
gridres = 5

#a/g min/max - must be < 1
ag_min = 0.05
ag_max = 0.2

#g min/max
g_min = 50E-4
g_max =500E-4

ngrids = 12

layer_index = 1.49
spacing = 200E-4

#Chosen method for finding Y. See tlmm for list of methods.
cap_method = 4

###############################################################################
###############################################################################

ag_range = np.linspace(ag_min,ag_max,gridres)
g_range = np.linspace(g_min,g_max,gridres)

n = np.ones(ngrids+1)*layer_index
n = np.append(n,1)
n = np.insert(n,0,1)

l = np.ones(ngrids-1)*spacing
l = np.append(l,spacing/2.)
l = np.insert(l,0,spacing/2.)

print "Thickness:" ,np.sum(l)

#strucutre assumes air-dielectric/grid/dielectric - air
grid = np.ones(ngrids)
```

```
grid = np.append(grid,0)
grid = np.insert(grid,0,0)

method = np.ones(len(grid))*cap_method

#folder name = sapceing_nlayers_minmaxag_minmaxg
olddir = os.getcwd()
try:
        os.mkdir("%s_%s_%s-%s_%s-%s"%(spacing/1e-4,ngrids,ag_min,ag_max,g_min/1e-4,g_max/1e-4))
        os.chdir("%s_%s_%s-%s_%s-%s"%(spacing/1e-4,ngrids,ag_min,ag_max,g_min/1e-4,g_max/1e-4))
except:
        print "File exists"
        selection = raw_input("Remove exising data? y/n")
        if selection == 'y':
                pass
                #need to fix
                #os.chdir("%s_%s_%s-%s_%s-%s"%(spacing,ngrids,ag_min,ag_max,g_min,g_max))
                #os.remove("??")

total_no_values = len(ag_range)*len(g_range)
args = []

#Can add extra loops to get extra param dimensions
for i in range (len(ag_range)):
        for j in range(len(g_range)):

                params = np.zeros((4,len(grid)))

                #Extra loop added to test axial graded materials
                for k in range(len(grid)):
                        params[1][k] = g_range[j]
                        params[0][k] = g_range[j]*(ag_range[i])
                args.append((params,method,grid,n,l,wave))


pool = Pool()
results = pool.map(mainfunc, args)
print "done"

effective_n = np.array(results,object).reshape((len(g_range),len(ag_range),2))
###############################################################################
#Plotting
##########

os.chdir(olddir)
print"Finish"
```

A.1.3 Band Theory

Below is an example code on how the artificial dielectric can be modelled using Bloch waves.

```
from __future__ import division
from matplotlib.patches import Patch
import numpy as np
import scipy as sp
import matplotlib.pyplot as pl
import os, multiprocessing, datetime, sys
#Path to tlmm file.
sys.path.append( "/Users/paulmoseley/Documents/Python/tlmm/" )
import tlmm
import cPickle as pickle
pl.ion()
reload(tlmm)

#Program to predict cutoff frequency for artifical dielectric
#Define struture

g = 200e-4
a_g= 0.15
a = (2*a_g*g)
print a
l_spacing = 100e-4
n_mat = 1.49
e_mat = n_mat**2
n0=376.73
c=3e8

theta = 0
theta = np.deg2rad(theta)

nn=1000

wlim =np.array([0.3,55.])  #cm^-1
wave=np.linspace(wlim[0],wlim[1],nn)

k = 2*np.pi*wave

beta = k*np.sqrt(e_mat - np.sin(theta)**2)

thi = beta*l_spacing

om = k*3e6

Y_0 = (2*g*e_mat/(np.pi*3e6*n0))*np.log(1./np.sin(np.pi*a/(2.*g)))
Y_d = e_mat/(np.sqrt(e_mat-np.sin(theta)**2)*n0)
```

```
b = (om*Y_0)/Y_d

kbh = (np.cos(thi)-(b/2.)*np.sin(thi))

for i in range(len(kbh)):
        if (kbh[i]> 1.):
                kbh[i] = 1
        elif (kbh[i]<-1):
                kbh[i] = -1

kbh_ful = np.arccos(kbh)

ktest = kbh_ful/l_spacing

neff = np.zeros(len(ktest))

for i in range(len(ktest)):
        if (kbh_ful[i] == np.pi):
                neff[i] = 0.
        else:
                neff[i] = ktest[i]/(2*np.pi*wave[i])

kbh_ful = np.rad2deg(kbh_ful)
pl.figure()
pl.plot(kbh_ful,wave)
pl.xlim(0,180)
pl.xlabel('$k_Brh$ (Degrees)')
pl.ylabel("Wavnumber (cm$^{-1}$)")
pl.grid()

pl.figure()
pl.plot(wave,neff)
```

This page was intentionally left blank

Appendix B

Appendix B

B.1 Definition of a lossless transmission line

The basic principle of a transmission line is to carry signal and thus power from a generator to a load. In the case when the length of wire is much smaller then the wavelength of the signal, the voltage and current are the same for each location on the wire. For high frequencies, the signal propagates as a wave of voltage and current along the line. This means that the impedance properties of the wire must be accounted for.

To account for this, a transmission line can be represented as a cascade of identical cells with infinitesimal length. Each cell can be represented as a circuit. In the case of a loss less transmission line, this can be represented as an L C circuit. Which is shown in figureB.1. The series inductance determines the variation of the voltages from the input to output of the cell. While the current flowing through the shunt capacitance determines the current variation through the cell. These two quantities can be used to define the characteristic impedance $Z_0 = \sqrt{L/C}$. The characteristic impedance is the ratio of the amplitudes of the voltage and current of a wave propagating along a line. It does not depend on the length of the line, only the configuration of the wire. For example the type of dielectric material used.

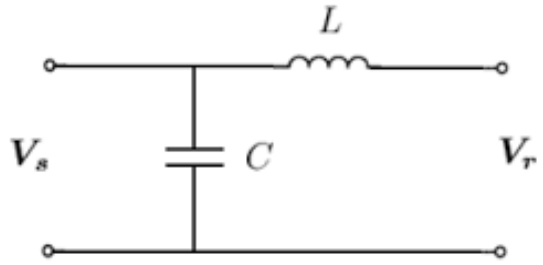

Figure B.1: The circuit representation of an LC transmission line.

For a given load impedance Z_R, a usefull quantity to know is the amount of reflected power, Γ_R. This is given by the characteristic impedance of the line Z_0 and is given by equation B.1

$$\Gamma_R = \frac{Z_R - Z_0}{Z_R + Z_0} \tag{B.1}$$

A final useful quantity when defining a transmission line is to able to calculate the input impedance for a given impedance length Z_L. This is given by equation B.2. Where l is the length of the transmission line and $\beta = \omega\sqrt{LC}$

$$Z_{in} = Z_0 \frac{Z_L + jZ_0 tan(\beta l)}{Z_0 + jZ_R tan(\beta d)} \tag{B.2}$$

Appendix C

Appendix C

C.1 List of Acronyms

Below is a list of acronyms used throughout this thesis.

AGN Active Galactic Nuclei

ARC Anti-Refection Coating

ALMA Atacama Large Millimetre Array

CMB Cosmic Microwave Background

ESA European Space Agency

FP Fabry-Perot

FTS Fourier Transform Spectrometer

FSS Frequency Selective Surface

Ghz Gigahertz

GRIN Graded Index

HWP Half Waveplate

IF Intermediate Frequency

LO Local oscillator

MoM Method of Moments

SHM Sub-Harmonic Mixer

THz Terahertz

VNA Vector Network Analyser

Bibliography

[1] H. Dole, G. Lagache, J.-L. Puget, K. I. Caputi, N. Fernndez-Conde, E. Le Floc'h, C. Papovich, P. G. Prez-Gonzlez, G. H. Rieke, and M. Blaylock, "The cosmic infrared background resolved by spitzer," *A&A*, vol. 451, no. 2, pp. 417–429, 2006. [Online]. Available: http://dx.doi.org/10.1051/0004-6361:20054446

[2] M. J. Barlow, B. M. Swinyard, P. J. Owen, J. Cernicharo, H. L. Gomez, R. J. Ivison, O. Krause, T. L. Lim, M. Matsuura, S. Miller, G. Olofsson, and E. T. Polehampton, "Detection of a noble gas molecular ion, 36arh+, in the crab nebula," *Science*, vol. 342, no. 6164, pp. 1343–1345, 2013. [Online]. Available: http://www.sciencemag.org/content/342/6164/1343.abstract

[3] A. Lazarian, "Tracing magnetic fields with aligned grains," *Journal of Quantitative Spectroscopy and Radiative Transfer*, vol. 106, no. 1, pp. 225–256, 2007.

[4] P. Ade, R. Aikin, D. Barkats, S. Benton, C. Bischoff, J. Bock, J. Brevik, I. Buder, E. Bullock, C. Dowell *et al.*, "Bicep2 i: Detection of b-mode polarization at degree angular scales," *arXiv preprint arXiv:1403.3985*, 2014.

[5] C. Yu, S. Fan, Y. Sun, and E. Pickwell-MacPherson, "The potential of terahertz imaging for cancer diagnosis: A review of investigations to date," *Quantitative Imaging in Medicine and Surgery*, vol. 2, no. 1, pp. 33–45, 03 2012. [Online]. Available: http://www.ncbi.nlm.nih.gov/pmc/articles/PMC3496499/

[6] P. A. R. Ade, G. Pisano, C. Tucker, and S. Weaver, "A review of metal mesh filters," in *Society of Photo-Optical Instrumentation Engineers (SPIE) Conference Series*, ser. Society of Photo-Optical Instrumentation Engineers (SPIE) Conference Series, vol. 6275, Jul. 2006.

[7] H. O. Moser, J. A. Kong, L. K. Jian, H. S. Chen, G. Liu, M. Bahou, S. M. P.

Kalaiselvi, S. M. Maniam, X. X. Cheng, B. I. Wu, P. D. Gu, A. Chen, S. P. Heussler, S. bin Mahmood, and L. Wen, "Free-standing thz electromagneticmetamaterials," *Opt. Express*, vol. 16, no. 18, pp. 13 773–13 780, Sep 2008. [Online]. Available: http://www.opticsexpress.org/abstract.cfm?URI=oe-16-18-13773

[8] S. Mener, R. Gillard, R. Sauleau, C. Cheymol, and P. Potier, "Design and characterization of a cpss-based unit-cell for circularly polarized reflectarray applications," *Antennas and Propagation, IEEE Transactions on*, vol. 61, no. 4, pp. 2313–2318, April 2013.

[9] A. V. Kildishev, A. Boltasseva, and V. M. Shalaev, "Planar photonics with metasurfaces," *Science*, vol. 339, no. 6125, 2013. [Online]. Available: http://www.sciencemag.org/content/339/6125/1232009.abstract

[10] J. B. Pendry, "Negative refraction makes a perfect lens," *Phys. Rev. Lett.*, vol. 85, pp. 3966–3969, Oct 2000. [Online]. Available: http://link.aps.org/doi/10.1103/PhysRevLett.85.3966

[11] R. A. Shelby, D. R. Smith, and S. Schultz, "Experimental verification of a negative index of refraction," *Science*, vol. 292, no. 5514, pp. 77–79, 2001. [Online]. Available: http://www.sciencemag.org/content/292/5514/77.abstract

[12] T. J. Yen, W. J. Padilla, N. Fang, D. C. Vier, D. R. Smith, J. B. Pendry, D. N. Basov, and X. Zhang, "Terahertz magnetic response from artificial materials," *Science*, vol. 303, no. 5663, pp. 1494–1496, 2004. [Online]. Available: http://www.sciencemag.org/content/303/5663/1494.abstract

[13] *Ansoft HFSS*. [Online]. Available: http://www.ansoft.com/hfss/

[14] "Arc figure," http://hyperphysics.phy-astr.gsu.edu/hbase/phyopt/antiref.html.

[15] R. C. Compton, L. B. Whitbourn, and R. C. McPhedran, "Strip gratings at a dielectric interface and application of babinet's principle," *Appl. Opt.*, vol. 23, no. 18, pp. 3236–3242, Sep 1984.

[16] S. Tretyakov, *Analytical Modeling in Applied Electromagnetics*, ser. Artech House electromagnetic analysis series. Artech House, 2003. [Online]. Available: http://books.google.co.uk/books?id=MZ3tpGtadhcC

[17] N. Marcuvitz and I. of Electrical Engineers, *Waveguide Handbook*, ser. Iee Electromagnetic Waves Series. McGraw-Hill, 1951. [Online]. Available: http://books.google.co.uk/books?id=Ao34iFuNZgIC

[18] R. Ulrich, "Far-infrared properties of metallic mesh and its complementary structure," *Infrared Physics*, vol. 7, no. 1, pp. 37 – 55, 1967.

[19] T. Timusk and P. L. Richards, "Near millimeter wave bandpass filters," *Appl. Opt.*, vol. 20, no. 8, pp. 1355–1360, Apr 1981. [Online]. Available: http://ao.osa.org/abstract.cfm?URI=ao-20-8-1355

[20] S.-W. Lee, G. Zarrillo, and C.-L. Law, "Simple formulas for transmission through periodic metal grids or plates," *Antennas and Propagation, IEEE Transactions on*, vol. 30, no. 5, pp. 904 – 909, sep 1982.

[21] L. B. Whitbourn and R. C. Compton, "Equivalent-circuit formulas for metal grid reflectors at a dielectric boundary," *Appl. Opt.*, vol. 24, no. 2, pp. 217–220, Jan 1985.

[22] D. W. BERREMAN, "Optics in stratified and anisotropic media: 4 × 4-matrix formulation," *J. Opt. Soc. Am.*, vol. 62, no. 4, pp. 502–510, Apr 1972. [Online]. Available: http://www.opticsinfobase.org/abstract.cfm?URI=josa-62-4-502

[23] G. Zarrillo and K. Aguiar, "Closed-form low frequency solutions for electromagnetic waves through a frequency selective surface," *Antennas and Propagation, IEEE Transactions on*, vol. 35, no. 12, pp. 1406 – 1417, dec 1987.

[24] P. Ikonen, E. Saenz, R. Gonzalo, and S. Tretyakov, "Modeling and analysis of composite antenna superstrates consisting on grids of loaded wires," *Antennas and Propagation, IEEE Transactions on*, vol. 55, no. 10, pp. 2692 –2700, oct. 2007.

[25] P. Belov, S. Tretyakov, and A. Viitanen, "Dispersion and reflection properties of artificial media formed by regular lattices of ideally conducting wires," *Journal of Electromagnetic Waves and Applications*, vol. 16, no. 8, pp. 1153–1170, 2002. [Online]. Available: http://www.ingentaconnect.com/content/vsp/jew/2002/00000016/00000008/art00011

[26] R. Mittra, C. Chan, and T. Cwik, "Techniques for analyzing frequency selective surfaces-a review," *Proceedings of the IEEE*, vol. 76, no. 12, pp. 1593 –1615, dec 1988.

[27] J. Zhang, P. A. R. Ade, P. Mauskopf, L. Moncelsi, G. Savini, and N. Whitehouse, "New artificial dielectric metamaterial and its application as a terahertz antireflection coating," *Appl. Opt.*, vol. 48, no. 35, pp. 6635–6642, Dec 2009.

[28] D. R. Smith, S. Schultz, P. Markoš, and C. M. Soukoulis, "Determination of effective permittivity and permeability of metamaterials from reflection and transmission coefficients," *Phys. Rev. B*, vol. 65, p. 195104, Apr 2002. [Online]. Available: http://link.aps.org/doi/10.1103/PhysRevB.65.195104

[29] Z. Szabo, G.-H. Park, R. Hedge, and E.-P. Li, "A unique extraction of metamaterial parameters based on kramers #x2013;kronig relationship," *Microwave Theory and Techniques, IEEE Transactions on*, vol. 58, no. 10, pp. 2646–2653, Oct 2010.

[30] S. Monni, G. Gerini, A. Neto, and A. Tijhuis, "Multimode equivalent networks for the design and analysis of frequency selective surfaces," *Antennas and Propagation, IEEE Transactions on*, vol. 55, no. 10, pp. 2824–2835, Oct 2007.

[31] C. S. R. Kaipa, A. B. Yakovlev, F. Medina, and F. Mesa, "Transmission through stacked 2d periodic distributions of square conducting patches," *Journal of Applied Physics*, vol. 112, no. 3, 2012. [Online]. Available: http://scitation.aip.org/content/aip/journal/jap/112/3/10.1063/1.4740054

[32] H. F. Ma, G. Z. Wang, W. X. Jiang, and T. J. Cui, "Independent control of differently-polarized waves using anisotropic gradient-index metamaterials," *Sci. Rep.*, vol. 4, 09 2014. [Online]. Available: http://dx.doi.org/10.1038/srep06337

[33] G. Savini, P. A. Ade, and J. Zhang, "A new artificial material approach for flat thz frequency lenses," *Opt. Express*, vol. 20, no. 23, pp. 25 766–25 773, Nov 2012.

[34] R. W. Wood, *Physical Optics*, no. 71, 1905.

[35] B. Fong, J. Colburn, J. Ottusch, J. Visher, and D. Sievenpiper, "Scalar and tensor holographic artificial impedance surfaces," *Antennas and Propagation, IEEE Transactions on*, vol. 58, no. 10, pp. 3212–3221, Oct 2010.

[36] G. Minatti, F. Caminita, M. Casaletti, and S. Maci, "Spiral leaky-wave antennas based on modulated surface impedance," *Antennas and Propagation, IEEE Transactions on*, vol. 59, no. 12, pp. 4436–4444, Dec 2011.

[37] D. K. M. Paquay, J. Hesler, "Improvements on high performance solid state frequency extension units for full-band frequency coverage at mm-wave frequencies," *Antenna Measurement Techniques Association Symposium (AMTA), 4-9 November 2007,.*

[38] J. B. Caldwell, "Optical design with wood lenses 1: infinite conjugate systems," *Appl. Opt.*, vol. 31, no. 13, pp. 2317–2325, May 1992. [Online]. Available: http://ao.osa.org/abstract.cfm?URI=ao-31-13-2317

[39] G. Pisano, P. A. Ade, and S. Weaver, "Polarisation effects investigations in quasi-optical metal grid filters," *Infrared Physics Technology*, vol. 48, no. 2, pp. 89 – 100, 2006. [Online]. Available: http://www.sciencedirect.com/science/article/pii/S1350449505000526

[40] C. Gomez-Reino, V. Perez, and C. Bao, *Gradient-Index Optics: Fundamentals and Applications.* Springer Berlin Heidelberg, 2010. [Online]. Available: http://books.google.co.uk/books?id=9gqCcgAACAAJ

[41] P. Ade *et al.*, "A Measurement of the Cosmic Microwave Background B-Mode Polarization Power Spectrum at Sub-Degree Scales with POLARBEAR," *Astrophys.J.*, vol. 794, no. 2, p. 171, 2014.

[42] D. F. Filipovic, S. S. Gearhart, and G. M. Rebeiz, "Double-slot antennas on extended hemispherical and elliptical silicon dielectric lenses," *Microwave Theory and Techniques, IEEE Transactions on*, vol. 41, no. 10, pp. 1738–1749, 1993.

[43] P. Moseley, G. Savini, E. Saenz, J. Zhang, and P. Ade, "Lenster - a mm-wave flat lens: Further analysis," in *Antennas and Propagation Society International Symposium (APSURSI), 2013 IEEE*, July 2013, pp. 1184–1185.

[44] G. Savini, P. Ade, P. Moseley, J. Zhang, and E. Saenz, "Broadband thin flat lens at sub-thz frequencies," in *Millimeter Waves and THz Technology Workshop (UCMMT), 2013 6th UK, Europe, China*, Sept 2013, pp. 1–2.

[45] P. Moseley, S. Savini, E. Saenz, J. Zhang, and P. Ade, "Lensters #x2014; the evolution from filter to lens and beyond," in *Advanced Electromagnetic Materials in Microwaves and Optics (METAMATERIALS), 2013 7th International Congress on*, Sept 2013, pp. 40–42.

[46] P. Moseley, G. Savini, P. Ade, J. Zhang, and E. Saenz, "#x201c; lensters #x201d; at mm-wave frequencies," in *Antennas and Propagation (EuCAP), 2013 7th European Conference on*, April 2013, pp. 1631–1635.

[47] P. Moseley, G. Savini, E. Saenz, P. Ade, and J. Zhang, "A focusing metamaterial based wollaston prism," in *Infrared, Millimeter, and Terahertz waves (IRMMW-THz), 2014 39th International Conference on*, Sept 2014, pp. 1–2.

[48] P. M. et al., "Design and characterization of a dual polarised lens."

[49] R. Yang, W. Tang, and Y. Hao, "A broadband zone plate lens from transformation optics," *Optics express*, vol. 19, no. 13, pp. 12 348–12 355, 2011.

[50] G. Marsden, P. Ade, S. Benton, J. Bock, E. Chapin, J. Chung, M. Devlin, S. Dicker, L. Fissel, M. Griffin *et al.*, "The balloon-borne large-aperture submillimeter telescope for polarization: Blast-pol," in *SPIE Astronomical Telescopes+ Instrumentation*. International Society for Optics and Photonics, 2008, pp. 702 002–702 002.

[51] B. C. Matthews, "Polarimetry and star formation in the submillimeter," in *Astronomical Polarimetry: Current Status and Future Directions*, vol. 343, 2005, p. 99.

[52] P. Bastien, E. Bissonnette, P. Ade, G. Pisano, G. Savini, T. Jenness, D. Johnstone, and B. Matthews, "Pol-2: a polarimeter for scuba-2," *Journal of the Royal Astronomical Society of Canada*, vol. 99, p. 133, 2005.

[53] B. Crill, P. Ade, E. Battistelli, S. Benton, R. Bihary, J. Bock, J. Bond, J. Brevik, S. Bryan, C. Contaldi *et al.*, "Spider: a balloon-borne large-scale cmb polarimeter," in *SPIE Astronomical Telescopes+ Instrumentation*. International Society for Optics and Photonics, 2008, pp. 70 102P–70 102P.

[54] B. Reichborn-Kjennerud, A. M. Aboobaker, P. Ade, F. Aubin, C. Baccigalupi, C. Bao, J. Borrill, C. Cantalupo, D. Chapman, J. Didier *et al.*, "Ebex: a balloon-borne cmb polarization experiment," in *SPIE Astronomical Telescopes+ Instrumentation*. International Society for Optics and Photonics, 2010, pp. 77 411C–77 411C.

[55] K. Arnold, P. Ade, A. Anthony, F. Aubin, D. Boettger, J. Borrill, C. Cantalupo, M. Dobbs, J. Errard, D. Flanigan *et al.*, "The polarbear cmb polarization experiment," in *SPIE Astronomical Telescopes+ Instrumentation*. International Society for Optics and Photonics, 2010, pp. 77 411E–77 411E.

[56] G. Savini, G. Pisano, and P. A. R. Ade, "Achromatic half-wave plate for submillimeter instruments in cosmic microwave background astronomy: modeling and simulation," *Appl. Opt.*, vol. 45, no. 35, pp. 8907–8915, Dec 2006.

[57] G. Pisano, G. Savini, P. A. Ade, V. Haynes, and W. K. Gear, "Achromatic half-wave plate for submillimeter instruments in cosmic microwave background astronomy: experimental characterization," *Applied optics*, vol. 45, no. 27, pp. 6982–6989, 2006.

[58] M. Bersanelli, N. Mandolesi, R. C. Butler, A. Mennella, F. Villa, B. Aja, E. Artal, E. Artina, C. Baccigalupi, M. Balasini *et al.*, "Planck pre-launch status: Design and description of the low frequency instrument," *arXiv preprint arXiv:1001.3321*, 2010.

[59] P. De Bernardis, P. Ade, R. Artusa, J. Bock, A. Boscaleri, B. Crill, G. De Troia, P. Farese, M. Giacometti, V. Hristov *et al.*, "Mapping the cmb sky: the boomerang experiment," *New Astronomy Reviews*, vol. 43, no. 2, pp. 289–296, 1999.

[60] M. Tegmark, A. de Oliveira-Costa, and A. J. Hamilton, "High resolution foreground cleaned cmb map from wmap," *Physical Review D*, vol. 68, no. 12, p. 123523, 2003.

[61] S. Church, P. Ade, J. Bock, M. Bowden, J. Carlstrom, K. Ganga, W. Gear, J. Hinderks, W. Hu, B. Keating *et al.*, "Quest on dasi: a south pole cmb polarization experiment," *New Astronomy Reviews*, vol. 47, no. 11, pp. 1083–1089, 2003.

[62] [Online]. Available: http://background.uchicago.edu/~whu/araa/node4.html#pla:cltt

[63] G. Pisano, G. Savini, P. A. R. Ade, and V. Haynes, "Metal-mesh achromatic half-wave plate for use at submillimeter wavelengths," *Appl. Opt.*, vol. 47, no. 33, pp. 6251–6256, Nov 2008. [Online]. Available: http://ao.osa.org/abstract.cfm?URI=ao-47-33-6251

[64] P. Andre, C. Baccigalupi, D. Barbosa, J. Bartlett, N. Bartolo, E. Battistelli, R. Battye, G. Bendo, J.-P. Bernard, M. Bersanelli *et al.*, "Prism (polarized radiation imaging and spectroscopy mission): A white paper on the ultimate polarimetric spectro-imaging of the microwave and far-infrared sky," *arXiv preprint arXiv:1306.2259*, 2013.

[65] P. Ade, D. Chuss, S. Hanany, V. Haynes, B. Keating, A. Kogut, J. Ruhl, G. Pisano, G. Savini, and E. Wollack, "Polarization modulators for cmbpol," in *Journal of Physics: Conference Series*, vol. 155, no. 1. IOP Publishing, 2009, p. 012006.

[66] S. Pancharatnam, "Generalized theory of interference, and its applications. part i. coherent pencils," in *Proceedings of the Indian Academy of Sciences, Section A*, vol. 44, no. 5. Indian Academy of Sciences, 1956, pp. 247–262.

[67] G. Pisano, M. W. Ng, V. Haynes, and B. Maffei, "A broadband metal-mesh half-wave plate for millimetre wave linear polarisation rotation," *Progress In Electromagnetics Research M*, vol. 25, pp. 101–114, 2012.

[68] J. Zhang, P. A. R. Ade, P. Mauskopf, G. Savini, L. Moncelsi, and N. Whitehouse, "Polypropylene embedded metal mesh broadband achromatic half-wave plate for millimeter wavelengths," *Appl. Opt.*, vol. 50, no. 21, pp. 3750–3757, Jul 2011.

[69] W. Commons. (2007) Half waveplate. [Online]. Available: http://upload.wikimedia.org/wikipedia/commons/6/68/Waveplate.png

[70] N. K. Grady, J. E. Heyes, D. R. Chowdhury, Y. Zeng, M. T. Reiten, A. K. Azad, A. J. Taylor, D. A. Dalvit, and H.-T. Chen, "Terahertz metamaterials for linear polarization conversion and anomalous refraction," *Science*, vol. 340, no. 6138, pp. 1304–1307, 2013.

[71] J. B. Pendry, D. Schurig, and D. R. Smith, "Controlling electromagnetic fields," *Science*, vol. 312, no. 5781, pp. 1780–1782, 2006. [Online]. Available: http://www.sciencemag.org/content/312/5781/1780.abstract

"The major difference between a thing that might go wrong and a thing that cannot possibly go wrong is that when a thing that cannot possibly go wrong goes wrong it usually turns out to be impossible to get at and repair."

Douglas Adams